

PIET REUTER

# Probing Inside a Scanning Electron Microscope

## DOCTORAL THESIS

For obtaining the academic degree of

Doktor der Naturwissenschaften

Doctoral Programme of Natural Sciences  
Technical Physics



Supervisor:

Univ.-Prof. Ph.D. Peter Hadley

Institute of Solid State Physics

Graz, November 2010



Deutsche Fassung:  
Beschluss der Curricula-Kommission für Bachelor-, Master- und Diplomstudien vom 10.11.2008  
Genehmigung des Senates am 1.12.2008

## EIDESSTÄTLICHE ERKLÄRUNG

Ich erkläre an Eides statt, dass ich die vorliegende Arbeit selbstständig verfasst, andere als die angegebenen Quellen/Hilfsmittel nicht benutzt, und die den benutzten Quellen wörtlich und inhaltlich entnommene Stellen als solche kenntlich gemacht habe.

Graz, am .....

.....  
(Unterschrift)

Englische Fassung:

## STATUTORY DECLARATION

I declare that I have authored this thesis independently, that I have not used other than the declared sources / resources, and that I have explicitly marked all material which has been quoted either literally or by content from the used sources.

.....  
date

.....  
(signature)



*All science is either physics or stamp collecting.*  
(Lord Kelvin)



---

Abstract of the  
Ph.D. Thesis

## **Probing Inside a Scanning Electron Microscope**

Piet Reuter

*Institute of Solid State Physics, Graz University of Technology  
8010 Graz, Austria*

Today's electronic devices tend to have sizes between a few nanometers and a few microns. For a full understanding of these devices it is often necessary to measure the current distribution and the electrostatic potential on a scale smaller than the device itself. For this purpose, a scanning electron microscope (SEM) probe station was assembled. It consists of six micromanipulators, which can be positioned with sub-nanometer precision inside a SEM. The micromanipulators hold sharp metal tips, which are used for manipulation of small objects and electrical probing tasks. The flexibility of the SEM probe station was utilized to investigate a broad range of samples with diverse measurement techniques. The probe station was used to contact small samples or devices and characterize them electrically. Scanning probe measurements were performed for producing 2D maps of the electrostatic potential of conducting surfaces or measuring the potential drop along a single-walled carbon nanotube (SWCNT). The attractive van der Waals forces between tip and sample were used on different types of samples for mechanical manipulation, like pushing, lifting and separating small objects. Electrical cutting and structuring of metal surfaces was employed through contact-breaking microspark erosion (CBME) and electrical fusing experiments. Probing inside a SEM provides extra possibilities of investigation, especially on semiconducting devices. Voltage contrast imaging was used to observe p-n junctions in the secondary electron image or enhancing the visibility of SWCNTs. Charge carrier diffusion lengths in silicon could be determined by measuring the electron beam induced current (EBIC). In solution processed organic (P3HT:PCBM) and inorganic (CdS/CZTS) solar cells, the generated EBIC signal was used to determine the spatially resolved homogeneity in these devices.



---

Kurzfassung der  
Doktorarbeit

**Aufbau und Anwendungen eines Spitzenmessplatzes  
im Rasterelektronenmikroskop**

Piet Reuter

*Institut für Festkörperphysik, Technische Universität Graz  
8010 Graz, Österreich*

Elektronische Bauteile haben heutzutage in der Regel Ausmaße von wenigen Nanometern bis zu einigen Mikrometern. Für ein volles Verständnis dieser Geräte ist es oft notwendig, Messungen der Stromverteilung oder des elektrostatischen Potentials auf einer Skala durchzuführen, die kleiner als das Bauteil ist. Für diesen Zweck wurde ein Rasterelektronenmikroskop (REM)-Spitzenmessplatz aufgebaut. Dieser besteht aus sechs Mikromanipulatoren, welche mit Sub-Nanometer-Genauigkeit positioniert werden können. Die Mikromanipulatoren halten feine metallische Spitzen, die zur Manipulation von kleinen Objekten oder zur elektrischen Kontaktierung verwendet werden können. Die Flexibilität eines REM-Spitzenmessplatzes wurde genutzt, um eine breitgefächerte Auswahl an Proben mittels diverser Messmethoden zu untersuchen. Der Spitzenmessplatz wurde benutzt, um kleine Proben oder Bauteile zu kontaktieren und elektrisch zu charakterisieren. Rastersondenmessungen wurden durchgeführt, um 2D-Abbildungen des elektrostatischen Potentials von leitenden Oberflächen zu erstellen oder Messungen des Spannungsabfalls entlang einer einwandigen Kohlenstoffnanoröhre (SWCNT) durchzuführen. Die anziehenden Van-der-Waals-Kräfte zwischen Spitze und Probe wurden an unterschiedlichen Arten von Proben für mechanische Manipulationen genutzt, wie zum Beispiel zum Schieben, Heben und Trennen von kleinen Objekten. Elektrisches Schneiden und Strukturieren von metallischen Oberflächen wurde durch Kontakttrennungs-Funkenerodieren oder mittels Durchbrennen bei hohen Stromdichten erprobt. Das Sondieren in einem REM bietet zusätzliche Untersuchungsmöglichkeiten, speziell bei Halbleiterbauteilen. Das Potentialkontrast-Abbildungsverfahren wurde verwendet, um p-n-Übergänge im Sekundärelektronenbild sichtbar zu machen oder die Sichtbarkeit von SWCNTs zu verbessern. Die Diffusionslängen der Ladungsträger in Silizium konnten durch Messungen des Elektronenstrahl-induzierten Stroms (EBIC) bestimmt werden. In aus Lösung prozessierten organischen (P3HT:PCBM) und inorganischen (CdS/CZTS) Solarzellen wurde das generierte EBIC-Signal dazu benutzt, die räumlich aufgelöste Homogenität in diesen Bauteilen zu ermitteln.



# Contents

<b>1. Introduction</b>	<b>1</b>
1.1. Probing on a Small Scale . . . . .	1
1.2. Building of a SEM Probe Station . . . . .	2
1.3. Outline of this Thesis . . . . .	3
<b>2. Basic Fundamentals of Scanning Electron Microscopy</b>	<b>5</b>
2.1. Electron Beam Generation and Electron Optics . . . . .	5
2.2. Electron Beam-Specimen Interactions and Signal Detection . . . . .	6
<b>3. Experimental Setup</b>	<b>9</b>
3.1. Micromanipulators and X-Y Substage . . . . .	9
3.2. Light Microscope Probe Station . . . . .	10
3.3. SEM Probe Station . . . . .	11
3.4. Measurement Instruments . . . . .	13
3.5. Program Codes . . . . .	15
<b>4. Mechanical Manipulations of Micro- and Nanostructures</b>	<b>17</b>
4.1. Manipulation of Colloidal Gold Particles . . . . .	18
4.2. Manipulation and Attachment of CNTs to Tungsten Probe Tips . . . . .	20
4.3. Two-terminal Measurements on Tungsten Nanowires . . . . .	21
<b>5. Making Small Contacts</b>	<b>23</b>
5.1. Theoretical Basics of Electrical Contacts . . . . .	23
5.1.1. Field Emission . . . . .	23
5.1.2. Tunnel Contacts . . . . .	23
5.1.3. Quantum Point Contacts . . . . .	24
5.1.4. Sharvin Point Contacts . . . . .	25
5.1.5. The Classical Holm Resistance . . . . .	25
5.1.6. Temperature Dependence of Contacts . . . . .	26
5.1.7. Summary of the Contact Resistance Regimes . . . . .	27
5.2. Electrical Probing of Micro- and Nanostructures . . . . .	27
5.2.1. Examples of Unstable Contacts . . . . .	28
5.2.2. Electrical Forming . . . . .	29
5.2.3. Tip Cleaning by Direct Current Heating . . . . .	29
5.2.4. Sharpening and Cleaning of Tips Inside the FIB . . . . .	30
5.2.5. Mechanical Scratching . . . . .	30
5.3. Conclusion . . . . .	31

---

<b>6. Multi-Probe Measurements</b>	<b>33</b>
6.1. Scanning Five-Point Electrical Measurements . . . . .	33
6.2. Scanning Three-Point Electrical Measurements . . . . .	35
6.2.1. Resistance Determination Method . . . . .	35
6.2.2. Current Ratio Method . . . . .	38
6.3. Three-Point Measurement of the Potential Drop Along a SWCNT . . . . .	40
<b>7. Structuring and Modification of Metal Lines and Thin Films</b>	<b>43</b>
7.1. Contact-Breaking Microspark Erosion . . . . .	43
7.1.1. Basics on Spark Generation upon Opening Electric Contacts . . . . .	43
7.1.2. Experimental Results . . . . .	45
7.2. Electrical Fusing of Metal Wires and Thin Films . . . . .	47
7.2.1. Electrical Fusing of a Photolithography Mask . . . . .	47
7.2.2. Electrical Fusing of a Metal Wire . . . . .	48
7.3. Conclusion . . . . .	49
<b>8. Voltage Contrast Imaging and Electron Beam-Induced Current</b>	<b>51</b>
8.1. Voltage Contrast Imaging . . . . .	51
8.1.1. Voltage Contrast Imaging of P-N Junctions . . . . .	52
8.1.2. Voltage Contrast Imaging of Single-Walled Carbon Nanotubes . . . . .	52
8.2. Electron Beam-Induced Current . . . . .	53
8.2.1. EBIC Measurements on P-N Junctions . . . . .	53
8.2.2. EBIC Measurements on Schottky Contacts . . . . .	54
8.2.3. EBIC Measurements on Silicon Solar Cells . . . . .	55
8.3. Conclusion . . . . .	56
<b>9. EBIC Mapping in Solution Processed Solar Cells</b>	<b>59</b>
9.1. Working Principle of Solar Cells . . . . .	59
9.2. Fabrication . . . . .	62
9.2.1. P3HT:PCBM Solar Cells . . . . .	62
9.2.2. CdS/CZTS Solar Cells . . . . .	63
9.3. The EBIC Measurement Technique . . . . .	64
9.4. EBIC Measurements on P3HT:PCBM Solar Cells . . . . .	65
9.4.1. Beam Damage in P3HT:PCBM Solar Cells . . . . .	65
9.4.2. 2D Mapping of Organic Solar Cells Using EBIC . . . . .	69
9.4.3. 2D Maps of EBIC at Different Beam Energies . . . . .	69
9.4.4. Analysis of Different Annealing Temperatures . . . . .	73
9.4.5. Solar Cells Fabricated by Squeegee-Coating Processing . . . . .	75
9.5. EBIC in CdS/CZTS Solar Cells . . . . .	77
9.6. Conclusion . . . . .	80
<b>10. Summary</b>	<b>81</b>
<b>Bibliography</b>	<b>83</b>

<b>Acknowledgments</b>	<b>87</b>
<b>Appendix</b>	<b>89</b>
<b>A. Selected Program Codes</b>	<b>91</b>
A.1. Basic ADC Program . . . . .	91
A.2. Averaging ADC Measurement . . . . .	93
A.3. Basic DAC Program . . . . .	97
A.4. Basic Motion Generator for Nanocontroller and LT6820 . . . . .	98
A.5. Communication with Nanocontroller and LT6820 via RS232 . . . . .	100
A.6. Communication with Current Preamplifier SR570 . . . . .	103
<b>B. Source and Specifications of the Used Materials for Fabricating Solution     Processed Solar Cells</b>	<b>105</b>
B.1. Indium Tin Oxide (ITO) . . . . .	105
B.2. PEDOT:PSS . . . . .	105
B.3. P3HT . . . . .	106
B.4. PCBM . . . . .	106
B.5. Chloroform . . . . .	106



# 1. Introduction

Electronic devices tend to have sizes between a few nanometers and a few microns. To fully understand the operation of these devices it is often necessary to measure the current distribution and the electrostatic potential on a scale smaller than the device itself. This makes it necessary to operate the devices inside some kind of microscope that can resolve these small length scales. A SEM typically has a resolution of about 10 nm and makes images fairly quickly. To make electrical measurements, Kleindiek micromanipulators have been installed inside a JEOL SEM (*JSM-6490LV*). These micromanipulators are small robotic arms that can be controlled with a precision of a few tens of nanometers. The micromanipulators hold sharp metal tips like those used in a scanning tunneling microscope to make contact to the devices. This thesis describes the build-up of a SEM probe station, its various applications, its advantages compared to competing techniques, and its limitations.

## 1.1. Probing on a Small Scale

To perform electrical measurements on small objects or devices one has to establish an electric contact between a microscopic device and the macroscopic measurement instrument. This is usually a nontrivial task and requires a substantial effort.

One way to make contact to a nanostructure like a carbon nanotube (CNT) is to use electron beam lithography [38]. First, atomic force microscopy (AFM) is used to find the position of a CNT relative to some predefined markers. After that, resist has to be spun on the substrate and an electron beam transfers a pattern for the metalization into the polymer layer. After the development of the resist, the metal layer is evaporated and the following lift-off process completes the fabrication process of contact pads on the sample, which are then contacted by macroscopic probe tips or wire bonding. This approach works well, but is time consuming and expensive.

For situations like this, it is very beneficial to be able to contact the object of interest directly with probe tips while observing your actions with an appropriate microscope. This can be achieved by using a micromanipulator probe station. This approach has several advantages: It needs less expensive equipment (no cleanroom facilities, no vacuum deposition chamber), it is much quicker and much more flexible, because you can change the position of the contacts and measure at many points to map the potential. The downside is that making reliable contacts is not easy.

Recent developments in micromanipulators make it possible to make spatially resolved electrical measurements with a resolution of a few nanometers either under an optical microscope or in a SEM [9]. Sharp needles, similar to scanning tunneling microscope tips, are used to make electrical contact to the sample. This makes it possible to contact very

small conductors like a metal trace in an integrated circuit [29] or a carbon nanotube [6]. Measurements range from simple two-terminal over multi-terminal current-voltage characteristic measurements to scanning electrostatic potential measurements on a sub-micron scale.

The capability of contacting micro- or nanometer sized areas though comes at a price. There are various difficulties that are encountered when sharp metal needles are used to measure the electrical characteristics of small devices. Insulating barriers on the tip or the sample can inhibit the desired low ohmic contact although the tip is already in physical contact. Contact regimes, which implicate certain resistance values, range from tunnel contacts, quantum point contacts, Sharvin contacts and Holm contacts (ordered from high resistance to low resistance). The diffusion of atoms in and out of small contact areas lead to a fluctuation of contact resistances. The occurrence of high current densities at the small contact areas can lead to direct current heating, which can change or break the contact due to thermal expansion or alter the contact through electrical forming. Corrosion or electrochemical processes at the contacts can also lead to unreliable contacts. Tips can scratch thin films or damage small structures like CNTs. Furthermore, electric potential differences between tip and sample can lead to electric discharges, which can also cause severe damage. If this characterization takes place in a SEM, the electron beam can charge ungrounded conductors. If a needle is brought into the proximity of a charged metal region, a spark can ablate metal away from the film. This process is difficult to control and is best avoided by grounding all surfaces. Similar sparks are observed when mechanical vibrations cause an electrical probe needle to pull away from a conducting surface while a current of a few milliamps is flowing. Mechanical vibrations can also lead to damage of a thin conducting film through scratching and a loss of an electrical connection.

## 1.2. Building of a SEM Probe Station

I started my work under supervision of Prof. Peter Hadley in the *Molecular Electronics and Devices* group at TU Delft in January 2006. During my six month stay in the Netherlands, a Zyvex micromanipulator system was installed inside a SEM of Cees Dekker's *Molecular Biophysics* group. Together with Peter and Jae-Ryoung Kim, I could collect the first experiences with a micromanipulator probe station. Some of the results on manipulation of small objects (chapter 4) were already gathered in Delft. Starting in September 2006, Peter gave me the opportunity to continue our teamwork at the *Institute of Solid State Physics* in Graz, where he got the position of the director of the institute and started a new group.

One main part of my work in Graz was the build-up of a probe station with the ability of manipulation and characterization of micro- and nanostructures. Two kinds of probe stations were set up: One probe station is equipped with a light microscope inside a vacuum chamber and can be used for macroscopic samples [28] and testing purposes. This probe station served mainly as a test environment, which was used quite intensely. Before the completion of the SEM probe station, we had the opportunity to set up our

equipment from time to time in an environmental scanning electron microscope (*FELI Quanta 200*) at the FELMI institute (TU Graz).

The second probe station is situated inside a SEM and capable of high resolution imaging and e-beam assisted measurements. Because of the delayed availability of the necessary money to purchase the SEM, it was completed not until the end of the third year of my thesis.

During the build-up of the probe stations, several fine mechanical mountings, fittings and flanges had to be designed and integrated into the systems, as well as other components like a patch box for connecting different kinds of plugs and cables. Several of these parts were produced in the institute's workshop. Besides the hardware, various measurement instruments had to be implemented in the setup.

For the automation of the experiments, most of the measurement instruments and the micromanipulator controller can be connected to a PC. In most cases, the experiments were controlled by *LabVIEW* routines, which communicated with the peripheral devices, controlled the application flow and processed and stored the accumulating data. For the diverse experimental tasks and the different communication environments of the instruments, many programs were developed during this work.

## 1.3. Outline of this Thesis

In this work a scanning electron microscope is not only used as the essential imaging tool, but it plays also an active role in several measurement applications. Therefore, it is useful to understand the working principles of scanning electron microscopy, which are given in chapter 2 and cover electron beam generation, electron optics, beam-specimen interactions and signal detection.

Chapter 3 describes the experimental setup, which was assembled from scratch during this work. It consists of six Kleindiek micromanipulators and an x-y substage, a light microscope probe station setup, a SEM probe station setup and several additional measurement instruments for electrical characterization. Several control and data acquisition programs were written to automate and link the various machines for complex measurement routines, which will be discussed briefly.

Pushing, bending, lifting and moving of objects is a straightforward application of micromanipulators. However, the manipulation of very small objects can be very different from our macroscopic experiences. Because of large surfaces and low weights, the van der Waals force will play a dominant role in the microscopic world, leading to the "sticky fingers" problem [37]. Examples of mechanical manipulation of small gold balls, carbon nanotubes and tungsten nanowires are presented in chapter 4.

A prerequisite for performing electrical measurements is establishing an electrical contact. Chapter 5 focusses on the properties of small electrical contacts from a theoretical and an experimental point of view.

Electrical measurements were performed to determine current distributions and electrostatic potential distributions on a range of different samples by multi-probe measurements (chapter 6).

Micromanipulators that are put into a SEM to perform electrical measurements can also be used to selectively remove metal films from integrated circuits and photolithography masks by CBME. This can be useful in failure analysis or mask repair and is much cheaper than the conventional method of using a focused ion beam (FIB) system. Electrical fusing of a metal wire by putting a high current through it can also be used for interrupting a conducting path. These methods for structuring and modification of metal lines and surfaces are presented in chapter 7.

The ability to perform electrical measurements inside the SEM provides the means for specialized measurements. Applications for the methods of voltage contrast imaging and measuring the EBIC are presented in chapter 8. Voltage contrast imaging is used for directly observing a p-n junction as well as enhancing dramatically the visibility of otherwise non-resolvable SWCNTs in the secondary electron image. Measuring the spatially resolved EBIC is used to obtain charge carrier diffusion lengths in silicon and to map the short-circuit current in a silicon solar cell.

The intriguing results of mapping the EBIC signal of a silicon solar cell were the starting point for extensive studies on organic (P3HT:PCBM) [23] and inorganic (CdS/CZTS) [24] solution-processed solar cells, which are discussed in chapter 9. By illuminating the active region of the devices with an electron beam that penetrates through the metal back contact, 2D EBIC maps were obtained. Useful information about the homogeneity of the solar cells can be obtained on scales ranging from microns to millimeters and the form of the defects can be obtained from the measurements.

Chapter 10 summarizes this work.

Appendix A presents exemplary *ADbasic* program codes, which were written and developed during this work. The selected codes are elementary for standard measurement and communication tasks. The source and specifications of the used materials for fabricating the solution processed solar cells can be found in appendix B.

## 2. Basic Fundamentals of Scanning Electron Microscopy

Being not only an observational tool but playing also an important role in the measurements itself (see chapters 8 and 9) the fundamental basics of a scanning electron microscope (SEM), which are of importance here, are given in this chapter (after [19], for further reading: [4, 11, 33]).

The SEM images a sample surface by scanning it with a high-energy beam of electrons. The beam diameter of only a few nanometers allows a high spatial resolution. The narrow electron beam leads also to a large depth of field. The electrons interact with the sample producing a multitude of signals that contain information about the sample's surface topography, composition and other properties such as electrical conductivity. The produced signals (see Figure 2.1) include secondary electrons (SEs), back-scattered electrons (BSEs), characteristic and bremsstrahlung X-rays, Auger electrons, light (cathodoluminescence), specimen current, electron beam induced current (EBIC) (in semiconductors) and transmitted electrons (thin samples).

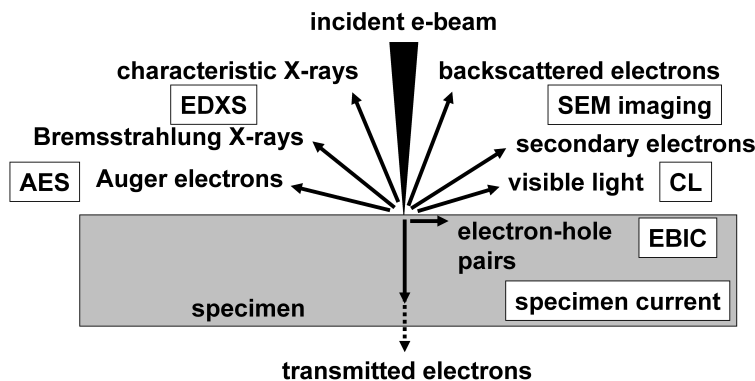


Figure 2.1.: Schematic diagram of the imaging and analytical modes of a SEM (adapted from [19]).

### 2.1. Electron Beam Generation and Electron Optics

Figure 2.2 shows a schematic diagram of the electron gun and the lens system of a SEM (adapted from [19]). Electrons from a thermionic cathode (tungsten hairpin cathode or LaB<sub>6</sub> cathode) or a field-emission cathode (cold-cathode type: tungsten single crystal

emitters; thermally-assisted Schottky type: tungsten tip covered with  $ZrO_2$ ) are accelerated by a voltage of 1–50 kV between cathode and anode. The beam cross-section with a diameter of 10–50  $\mu\text{m}$  for thermionic and 10–100 nm for field-emission guns is then demagnified by a two- or three-stage electron lens system so that an electron probe of about 1–10 nm carrying an electron probe current between 1–100 pA is formed at the specimen surface. A deflection coil system in front of the last lens scans the electron beam in a raster fashion.

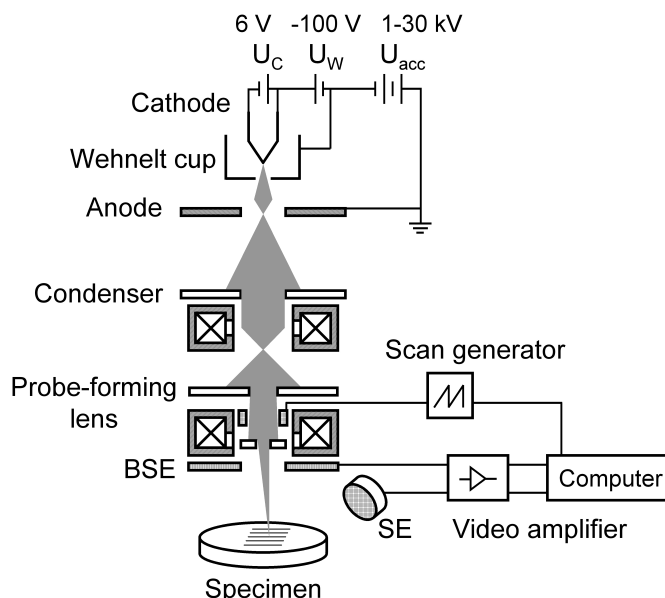


Figure 2.2.: Schematic diagram of the electron gun column of a SEM.

## 2.2. Electron Beam-Specimen Interactions and Signal Detection

The elementary interactions between the primary electrons and the sample atoms are elastic and inelastic scattering processes. The primary electrons lose energy by repeated inelastic scattering and absorption within a teardrop-shaped volume of the specimen known as the interaction volume. It extends from less than 100 nm to around 5  $\mu\text{m}$  into the surface. The size of the interaction volume depends on the acceleration voltage, the atomic number of the specimen and the specimen's density.

The Bethe stopping power relation [4, chap. 6] approximates the mean primary energy loss per unit trajectory length  $dE/dx$  for a mean ionization potential  $I$  in the limit of non-relativistic energies  $E_0 \ll m_0c^2$ :

$$\frac{dE}{dx} = \frac{Ne^4Z}{8\pi\epsilon_0E} \ln \frac{E_0}{I}. \quad (2.1)$$

$N$  is the number of atoms with atomic number  $Z$  per unit volume,  $I$  is the mean ionization potential for the specimen material,  $e$  is the electron charge,  $\epsilon_0$  is the dielectric constant for vacuum and  $m_0c^2$  is the electrons rest energy.

Secondary electrons are generated by inelastic excitation to such high energy levels that they become ionized. Their most probable energy is between 2–5 eV. Because of their low kinetic energies, they can leave the specimen only from a very thin surface layer of a few nanometers. The SE mode is therefore used to image the surface topography. They are standardly collected by the Everhart-Thornley detector [14]. A positive biased grid (100–200 V) draws the SEs towards the detector. The SEs that pass the grid are accelerated towards the scintillator with a bias of 10 kV. A light guide and a photomultiplier complete the detector. Typically one to ten photoelectrons will be created per incident SE. This detector stands out because of its low noise and wide bandwidth capability.

By convention, the discrimination between BSEs and SEs is drawn at the energy of 50 eV. A broad spectrum of BSEs between 50 eV and the primary electron energy is caused by the deceleration of electrons due to multiple energy losses and multiple scattering through large angles. The backscatter coefficient  $\eta_{BSE}$  is defined as the number of BSEs normalized to the total number of primary electrons. It increases with increasing atomic number of the specimen. Therefore a good material contrast can be achieved. The maximum information depth of the BSE signal is of the order of half the electron range, which limits the resolution of this imaging mode. Due to the straight trajectories of BSEs, detectors have to be mounted with a large solid angle of collection. Annular p-n junctions or scintillators without additional acceleration are used as detectors.

BSEs also excite SEs (SE<sub>2</sub>) on their path through the surface layer. These SE<sub>2</sub> decrease the high resolution capability of the SE mode, but also add a material contrast component to the signal.

If high energy electrons ionize inner shell electrons, the vacancy can be filled by an outer shell electron and the energy difference between the two states will be converted into a characteristic X-ray photon or transferred to another atomic electron (Auger electron). Characteristic X-ray spectroscopy is widely used for elemental analysis in SEMs. Auger electrons have characteristic kinetic energies and can leave the specimen only from a very thin surface layer. They can be used for surface sensitive elemental analysis.

The specimen current can also be used for imaging. Because of the small occurring currents (probe current minus emitted electrons) large probe currents or long recording times are required. If a sample is irradiated and at the same time an electrical measurement is carried out (like in the chapters 8 and 9), the specimen current adds to the measured current, but is often negligible compared to the other involved currents, for example EBIC.

In semiconductors, one primary electron generates numerous electron-hole pairs via ionization processes. In the presence of an internal electric field, such as a p-n junction or a Schottky barrier, or an externally applied electric field the charge carriers are separated and the resulting current can be measured. This technique provides the

means to quantitatively determine physical properties like the diffusion length, the recombination time, the width of a junction or its depth below the surface [33, chap. 4.7]. In such a way optoelectronic devices like solar cells can be analyzed by excitation via the electron beam instead of a light source.

Changes of the electric potential of a sample or a smaller part of it influences the potential distribution between the object and the collector of the SE detector and therefore the trajectories of the SEs. Applying a positive voltage to a region leads to less emitted SEs. Reversing the bias will increase the emitted electrons and lead to a brighter image. Thus a change of potential is reflected directly in the SE signal. Regions of the same potential (conducting objects, i.e. wires) will have no potential contrast, whereas potential drops or regions of different potential can be visualized. This can be used for inspection purposes in integrated circuits. Broken wires and p-n junctions can be directly seen in the SE image.

## 3. Experimental Setup

During this work two probe stations were assembled. Up to six micromanipulators can be mounted either under a light microscope or a scanning electron microscope (SEM) for manipulation and electrical measurements. For these measurements instruments like two current preamplifiers (*SR570*), a sourcemeter (*Keithley 2636A*) and two *ADwin-Pro II* systems were available. Several control and data acquisition programs were written to automate and link the diverse machines for complex measurement routines.

### 3.1. Micromanipulators and X-Y Substage

For the manipulation and positioning of sharp, chemically etched metallic tips (usually tungsten), six *MM3A-EM* micromanipulators from the company Kleindiek were obtained. Two rotational (A+B) and one linear (C) axis move the manipulator arm in all directions. The nominal (if driven by the associated *Nanocontroller*) smallest step size of the fine movement is 0.25 nm for axis C (A+B: 5 nm) and the range is 1  $\mu\text{m}$  (20  $\mu\text{m}$ ).<sup>1</sup> Stick-slip motion enables the manipulator to overcome the fine range limitation. Using coarse steps, a range of 12 mm (C) and 240° (A+B) can be achieved. The *Nanocontroller* can be operated by rotary knobs, a joypad or via PC by a RS232 port. Additionally a voltage can be directly applied to an analog input of the *Nanocontroller* with the range of  $\pm 10$  V which adds to the normal output voltage of the *Nanocontroller*, adjusted by the other channels. It is amplified internally by a factor of 8.5. Care has to be taken, that the sum of the two voltages do not exceed the limit for protection of the piezo crystal and the electronics. *LabVIEW* and *ADBasic* (programming language for *ADwin-Pro II*) programs were developed to move the manipulators via RS232 commands and analog voltages.

Although the manipulators allow step sizes in the nanometer range, a precise positioning is due to the stick-slip motion at larger distances and the curvature of the path of the rotational axis not possible. For two-dimensional scans an x-y substage (*LT6820* from Kleindiek) with encoders was installed. The control of the table is similar to the manipulators. Additionally, the substage can travel to given coordinates with a precision of 100 nm. The maximum range of the linear table is 20 mm and the fine step size is nominally 0.5 nm.

---

<sup>1</sup>Using the *ADwin-Pro II* analog output (16 Bit resolution) a sixteen times higher resolution can be achieved than with the *Nanocontroller* (12 Bit resolution).

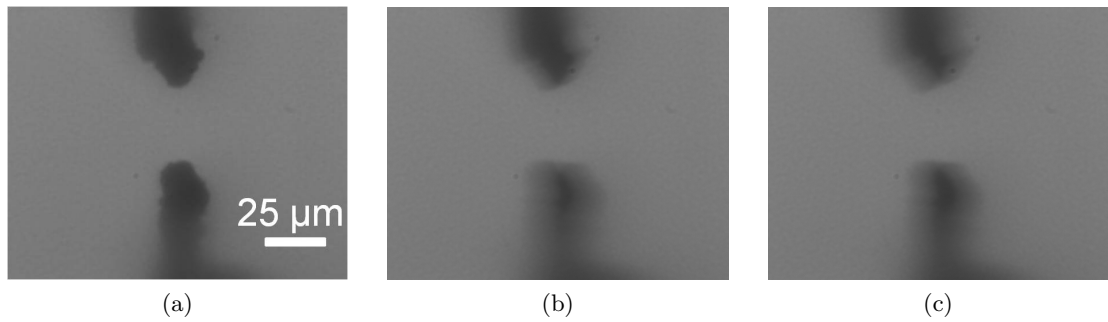


Figure 3.1.: Microscope images of two wires attached to manipulators inside the vacuum chamber. Without vibration damping the operation of the turbomolecular pump will induce strong vibrations in the manipulators. During acceleration of the rotation speed images were taken at different speeds: (a) the pump is not in operation, (b) the rotation speed is  $390 \text{ s}^{-1}$  and (c)  $410 \text{ s}^{-1}$ .

### 3.2. Light Microscope Probe Station

For purposes, where the optical resolution of a light microscope is sufficient for the probing measurements and for a testing environment, a vacuum chamber was designed and built in the institute's workshop. A glass window in the center of the lid allows for observation by a light microscope. For excess to the chamber, the lid can be lifted. Six flanges (DN 50 ISO-KF) are available for mounting the vacuum pump, electric feedthroughs and other user requests.

The vacuum system consists of a turbomolecular pump (Pfeiffer: *TMH 071 P*), a rotary vane pump (Pfeiffer: *DUO 5 M*) as backing pump and a combined Pirani and cold cathode system gauge (Pfeiffer: *PKR 251*; pressure range:  $5 \times 10^{-9} - 10^3 \text{ mbar}$ ). With this setup pressures down to  $10^{-6} \text{ mbar}$  could be achieved in the vacuum chamber.

Vibration damping is for our applications very important. Vibrations coupled in the vacuum chamber via the floor of the building (low frequencies) and the pumps (rotation speed of the turbopump is  $1500 \text{ s}^{-1}$ ) can induce damage through failing electrical contacts or scratching as well as a blurry microscope image. A series of microscope images of two wires attached to manipulators inside the vacuum chamber at different rotation speeds of the turbopump are shown in Figure 3.1. The manipulators showed strong resonances between  $350 \text{ s}^{-1}$  and  $450 \text{ s}^{-1}$ .

To reduce vibrations inside the chamber several damping mechanisms were employed. To prevent vibration coupling via the hose between the two pumps, the hose is fixed to a heavy concrete weight. A vibration compensator is connected between the high vacuum side of the turbopump and the vacuum chamber. To reduce building vibrations coupled in through the floor a small rigid and heavy table was custom made by the workshop. An active vibration damping table (Halcyonics: *Micro 40*) was bought to further decrease the mechanical noise. The active bandwidth of the damping system

ranges from 0.6–200 Hz and the isolation performance above 10 Hz is 40 dB.<sup>2</sup>

For observation a light microscope is used. The image is recorded by a CCD camera and transferred to a PC via an USB cable. A microobjective (20x/0.35, working distance: 20 mm) and a long-distance objective (3.1x, working distance: 77 mm). An additional zoom with a magnification ranging from 0.75x–5x is installed. The microscope is mounted on a custom made stand. A micrometer spindle moves the microscope vertically for focussing. For the lateral positioning two x-y tables are installed. A photograph of the assembled light microscope probe station is shown in Figure 3.2.



Figure 3.2.: Photograph of the assembled light microscope station.

### 3.3. SEM Probe Station

The main goal of this work in the sense of installation was the assembly of a SEM probe station for high resolution probing. Multiple individual instruments were combined in one setup and several parts were designed and custom made for the special purpose.

The main frame of this setup is the JEOL *JSM-6490 LV* SEM. Two vacuum modes are available. The high vacuum mode has an ultimate pressure in the gun chamber of the order of  $10^{-6}$  mbar. In this mode the secondary electron (SE) detector (Everhardt-Thornley detector) as well as the back-scattered electron (BSE) detector (semiconductor p-n junction detector) can be used for imaging. In the low vacuum mode the pressure can be adjusted in the range of 0.1–2.7 mbar, but only the BSE detector is available. Two oil rotary pumps and one oil diffusion pump are installed for establishing the desired pressure conditions. The electron gun of the SEM is a thermionic tungsten hairpin filament type. The acceleration voltage can be set from 0.3–30 kV.

---

<sup>2</sup>Values are taken from operating manual.

Up to six manipulators can be installed inside the SEM, which are mounted either on the stage or overhead on an adapter plate, which is fixed to the chamber wall. Manipulators, which are mounted on the stage, will travel together with the stage and the sample, whereas the top mounted manipulators stay in place and are fixed relative to the chamber and the electron beam. If mounted both ways at the same time, one has to be careful not to crash the manipulators into each other, especially tilting the sample should be off-limits.<sup>3</sup> The *LT6820* substage is placed between the stage and the manipulator fixture. The sample as well as the stage mounted manipulators will travel uniformly with the piezo-driven substage. The substage is electrically isolated from the SEM stage (connected by plastic washers and screws) for cases, when we want to measure the specimen current with our probes. Additionally, the safety “collision detection” is circumvented, which was triggered through the grounded cable shield of the substage and the manipulators leading to a blockage of the stage movement. A simplified sketch of the setup is shown in Figure 3.3.

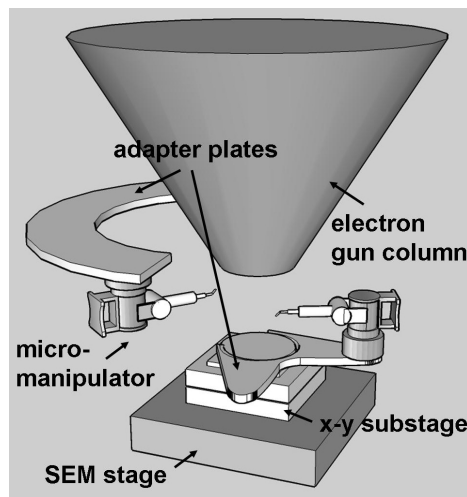


Figure 3.3.: A simplified sketch of the SEM probe station. Shown are two manipulators, one in top and one in bottom mounting configuration. The upper adapter plate is fixed to the chamber and can be adjusted in height. The bottom mounted manipulator travels with the piezo-driven substage and the SEM stage. The sample holder is mounted in the center of the bottom adapter plate.

Standardly, the electric signal from the manipulator tip is wired to the *Nanocontroller* together with the piezo supply voltages. An air splitter can bundle the signals of up to four *Nanocontrollers* to a 30 wire cable. This is connected to a vacuum feedthrough. Inside the vacuum chamber (e.g. a SEM) the vacuum splitter separates the signals again and a metallic shielded cable connects to each manipulator. Using the standard

<sup>3</sup>For the current installation a value of 65 mm “sample height” in the SEM main menu prevents the top and bottom mounted manipulator bodies from collision during stage drive.

tip wiring, the maximum probing voltage is 100 V and 100 mA for the current. For being able to use higher voltages and currents in the SEM probe station as well as reducing electromagnetic pickup from neighboring wires, isolated tip holders were developed which connect the probe tips to separate BNC feedthroughs.

## 3.4. Measurement Instruments

In this section the main instruments used for electrical measurements and automatic control of the manipulators are presented.

**ADwin-Pro II-light** The *ADwin-Pro II-light* (*ADwin*) system consists of analog and digital outputs, which are connected to a dedicated real-time processor with a clock rate of 300 MHz. Via an Ethernet communication link to the PC, user-defined measurement and control tasks are passed to the *ADwin* system and executed autonomously. Two identical “light” systems were obtained, which have half the width of the standard 19 inch version. One *ADwin* system has an analog input module (Pro II-AIn-F-8/18 Rev. E) with eight Fast-AD channels (18 Bit resolution), which are galvanic separated. Because of the rather low input resistance of only 330 k $\Omega$ , correct high resistance measurements are not possible. In these cases the high impedance source has to be transformed with a voltage buffer (see Fig. 3.5b). For applying voltages an analog output module (Pro II-AOut-8/16 Rev. E) with eight channels (16 Bit resolution) is integrated. Both modules have a voltage range of  $\pm 10$  V. Additionally, a system has four RS-232 interfaces to communicate with peripheral instruments (*Nanocontroller*, *LT6820* and *SR570*). For programming the *ADwin* systems the program language *ADbasic* is available. There are also several interfaces to other languages and platforms, i.e. *LabVIEW*.

**Current preamplifier SR570** For the measurement of small currents, for example in the EBIC measurements (see chapter 9), two *SR570* current preamplifiers (Stanford Research) were obtained. The sensitivity ranges from 1 pA/V to 1 mA/V and the maximum input current is  $\pm 5$  mA. A low noise mode allows for good noise performance on the expense of bandwidth, which was normally chosen. The high bandwidth mode produced too much noise especially at high sensitivity settings. Figure 3.4 shows the response of the *SR570* to a sine wave at different frequencies in both modes. A Lock-In amplifier (*SR830*) provided a sine wave with an amplitude of 1 V. This signal was connected to the current preamplifier input with a resistance of 1 G $\Omega$  in series. The sensitivity setting was set to 1 nA/V. The low noise mode shows inferior performance at higher frequencies. Above 10 kHz the dynamic response is decreasing, at 200 kHz the amplitude is already damped to 1/10. If the low noise mode is crucial for a sensible signal to noise ratio, good results are only obtained for frequencies up to 10 kHz.

**SourceMeter 2636A** The versatile *SourceMeter 2636A* (Keithley) allows for sourcing and measuring currents and voltages in a broad range (1 fA–1.5 A, 1  $\mu$ V–200 V). The

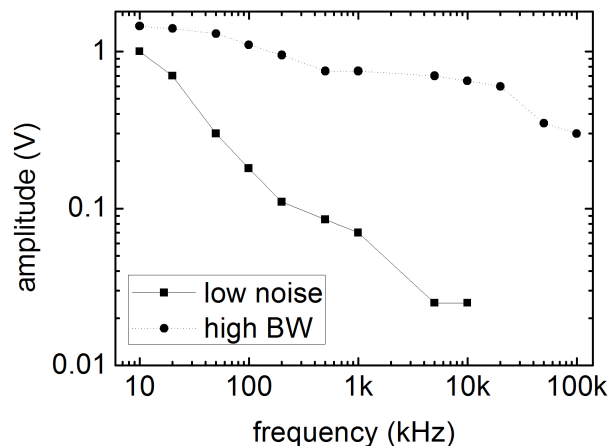


Figure 3.4.: Bandwidth measurement of the *SR570*. A Lock-In amplifier generated a sine wave of 1 V amplitude and a  $1\text{ G}\Omega$  resistor was placed in series. The current was measured with the current preamplifier at the sensitivity of  $1\text{ nA/V}$  in the low noise mode (squares) and in high bandwidth mode (circles). The low noise mode shows inferior performance at higher frequencies.

*2636A* has two independent source measurement units (SMUs). For low impedance circuits ( $<1\text{ k}\Omega$ ) 4-wire remote sense connections are available.

**Manufacture of printed circuit board electronics** When measuring small signals, a long distance between the amplifier stage and the device under test (DUT) should be avoided. To reduce electromagnetic pickup, that is amplified together with the signal coming from the DUT, the preamplifier stage can be placed close to the tips inside the vacuum chamber. For the integration of small, lightweight preamplifiers and voltage followers close to the tips, electric circuits were built on printed circuit boards.

For the microspark erosion measurements (see chapter 7) a dedicated circuit was developed (see Figure 3.5a). A standard current-voltage converter circuit was modified with an inductor ( $L = 1\text{ mH}$ ) placed between the tip and the inverting input for controlling the energy released upon breaking contact.

In order to measure a high impedance source with a measurement instrument with low input impedance, a voltage follower is used (see Figure 3.5b). A pull-down resistor ( $R_{PD} = 10\text{ M}\Omega$ ) brings the output to zero voltage if the tip is in air ( $R_{DUT} = \infty$ ). For an electrical approach detection, a Lock-In amplifier can be used. An AC voltage modulates the connection to ground. The resistors  $R_{PD}$  and  $R_{DUT}$  act as a voltage divider. If  $R_{PD} \ll R_{DUT}$  the Lock-In amplifier measures the modulation in the output voltage. The measured amplitude of the AC signal decreases for decreasing  $R_{DUT}$ .

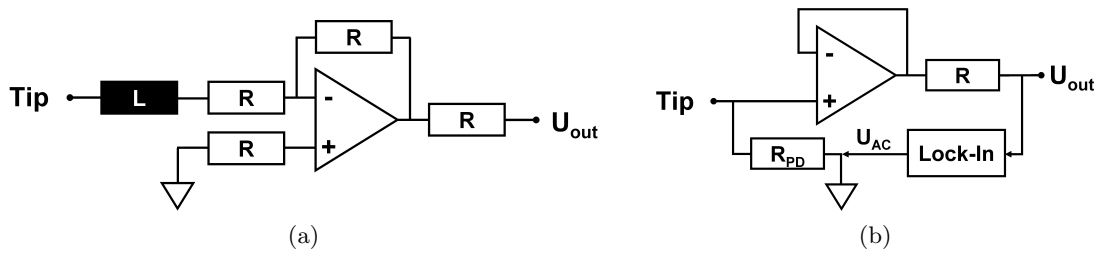


Figure 3.5.: Electronic circuit diagram designs. (a) A standard current-voltage converter circuit was modified with an inductor placed between the tip and the inverting input for controlling the energy released upon breaking contact (see chapter 7). The resistance of  $R$  was chosen to  $1\text{ k}\Omega$ . (b) In order to measure a high impedance source with a measurement instrument with low input impedance, a voltage follower is used. A pull-down resistor ( $R_{PD} = 10\text{ M}\Omega$ ) brings the output to zero voltage if the tip is in air ( $R_{DUT} = \infty$ ). For an electrical approach detection, a Lock-In amplifier can be used. An AC voltage  $U_{AC}$  modulates the connection to ground. The resistors  $R_{PD}$  and  $R_{DUT}$  act as a voltage divider. If  $R_{PD} \ll R_{DUT}$  the Lock-In amplifier measures the modulation in the output voltage. The measured amplitude of the AC signal decreases for decreasing  $R_{DUT}$ .

### 3.5. Program Codes

For various measurement and controlling tasks programs in *ADbasic* and *LabVIEW* were written for synchronous interplay. Basic programs measure the voltages on the eight *ADwin* inputs and apply voltages on the outputs. More complex codes allow for time series measurements with power spectrum analysis, two-dimensional scanning routines for micromanipulators and x-y substage, automatic approach, a waveform generator and current-voltage sweep measurements. For complex tasks *LabVIEW* combines several subroutines and controls their execution, collects and displays data and acts as the user interface. In Appendix A the source code of selected elementary *ADbasic* programs is presented for measuring and applying voltages, motion control for the manipulators and the x-y substage as well as basic code for communication via RS232 between the *ADwin* system and a *Nanocontroller*, the *LT6820* substage or the *SR570* current preamplifier.



## 4. Mechanical Manipulations of Micro- and Nanostructures

Ever since Richard P. Feynman's stimulating talk, "There's Plenty of Room at the Bottom", where he challenged scientists to consider "manipulating and controlling things on a small scale", tremendous progress has been made in the field of nanotechnology.<sup>1</sup> Feynman suggested that tiny machining tools such as drills and lathes should be made to make tiny parts and that these could be used to make even smaller machine tools. He thought we needed to develop "tiny hands" that would hold and manipulate the nanocomponents that we produce.

What Feynman did not foresee is that miniaturization would mostly advance by photolithography. In photolithography we don't need tiny tools or tiny hands to manipulate the small components we make. All of the components are held by a substrate during processing. Photolithography has been spectacularly successful and is now routinely used to make devices only a few nanometers in size. The length in a modern transistor is 20 nm long and the gate oxide is only 1 nm thick. One hundred billion transistors like this are fabricated simultaneously on a single wafer. This makes the price per transistor very low.

Even though photolithography has been so successful, many speculate that by using chemical synthesis, devices like transistors and light emitting diodes could be made more cheaply. The transistors that are made now have the size of macromolecules. Chemical synthesis can be used to produce macromolecules in quantities of  $10^{25}$  per batch. If transistors could be made by this route, they would be much cheaper than those produced by photolithography.

Chemically synthesized electronic components would have to be assembled into circuits, presumably by self-assembly. This will likely limit such circuits to architectures where the components are arranged in periodic patterns.

In order to test prototypes of chemically synthesized devices it is important to be able to contact them electrically. Either the devices have to be placed on electrical contacts or the electrical contacts have to be placed on the devices. This is once again the "tiny hands" problem described by Feynman. Under some circumstances it is possible to manipulate atoms and molecules with a scanning tunneling microscopy (STM). However, Richard Smalley has argued that it is not possible to make tiny hands that can pick up molecules and place them where they should go. The problem is that the molecules tend to stick to the hands due to van der Waals forces [37]. This is known as the "sticky" fingers problem.

---

<sup>1</sup>Feynman, Richard. (1959) *There's Plenty of Room at the Bottom*. Available at <http://feynman.caltech.edu/plenty.html> (June 24, 2010).

This chapter describes some experiments where chemically synthesized nanostructures such as carbon nanotubes or gold nanospheres are moved around with micromanipulators in a scanning electron microscope (SEM). Our intuition based on observations of macro objects is not always a good guide to how small objects behave as you try to push them around. We certainly observe the sticky fingers problem of Smalley. It is difficult to controllably move anything a small distance. Typically once enough force is applied to move an object at all, it jumps to a new position.

#### 4.1. Manipulation of Colloidal Gold Particles

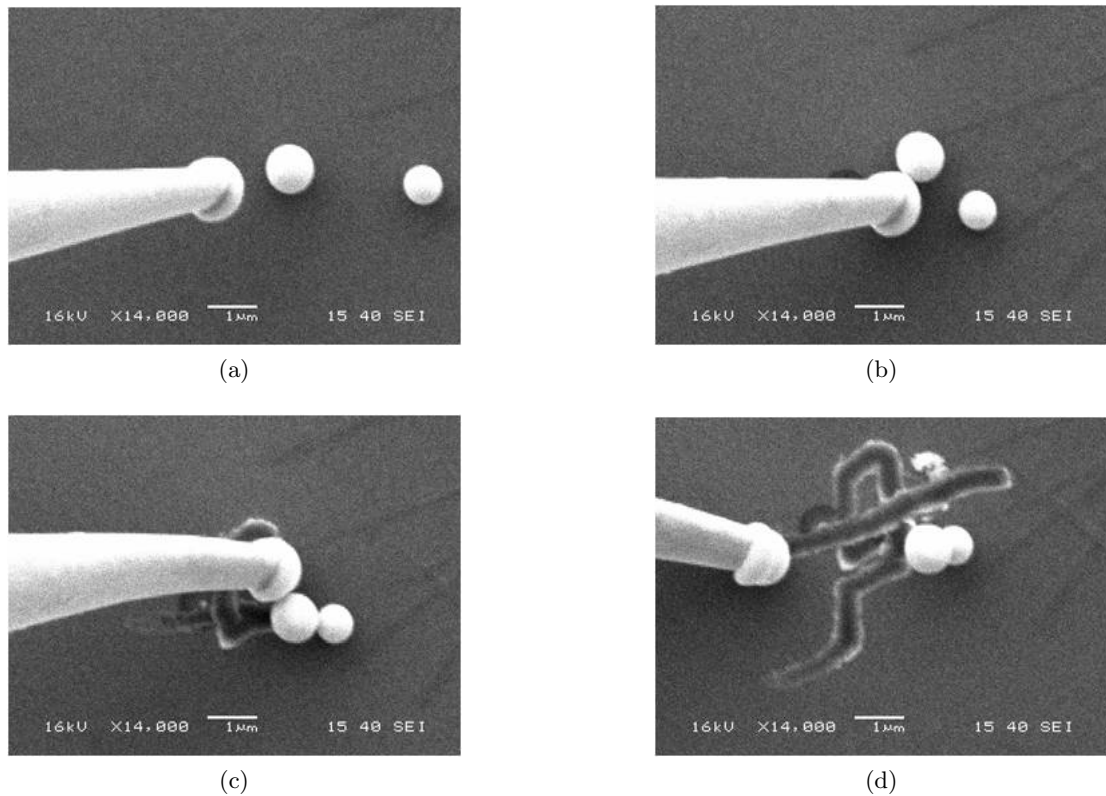


Figure 4.1.: A series of images of a tungsten tip pushing a colloidal gold particle over a surface (thin gold film on a  $\text{SiO}_2$  substrate) inside a SEM. The gold particle was brought into contact with a second micro-ball. The tungsten tip leaves scratches in the softer gold surface behind. (This experiment was performed on a similar probe station that was built at the Kavli Institute of Nanoscience at TU Delft, The Netherlands.)

In order to investigate the potential of moving small objects and assemble them to arbitrary patterns, a colloidal suspension of gold particles was drop-cast on two different

substrates, a thin gold film on  $\text{SiO}_2$  and a bare  $\text{SiO}_2$  substrate. The diameter of the particles was in the range between 200 nm and 1  $\mu\text{m}$ .<sup>2</sup> The samples were dried before transfer into the SEM chamber. The measurements presented in this subsection were performed at the Kavli Institute of Nanoscience (TU Delft, The Netherlands).

In Figure 4.1 a series of SEM images shows, how a gold particle with a diameter of around 1  $\mu\text{m}$  is moved over a gold surface by a commercially available tip. The tiny ball is pushed over a distance of a few micrometers and placed on top of a second gold particle (see Figure 4.1d). During the manipulations, the tungsten tip scratches over the soft gold surface and leaves scrape marks behind. The apex of the tip is rounded, because of an electric discharge (see chapter 7), which occurred before these images were taken.

In order to have sharper tips with a higher aspect ratio, a tungsten wire was etched electro-chemically in 1-Molar aqueous sodium hydroxide (NaOH). With such a tip, colloidal gold particles of a diameter of 200 nm dispersed on a  $\text{SiO}_2$  substrate were mechanically manipulated. On the  $\text{SiO}_2$  substrate, the colloidal particles were sticking to the substrate due to van der Waals interaction, so that a certain force was needed by the tip to overcome this attractive force. Because of that, the small particles rather jumped than rolled to the next position. From 4.2a–4.2c the gold particles were arranged by the tip to a triangular shape.

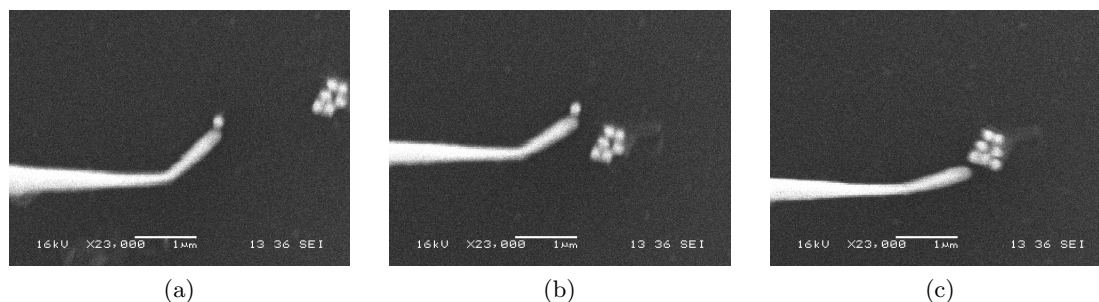


Figure 4.2.: A micromanipulator is manipulating colloidal gold particles with a diameter of 200 nm inside a SEM. The colloidal particles were sticking to the sample substrate ( $\text{SiO}_2$ ) due to van der Waals interaction, so that a certain force was needed by the tip to overcome this attractive force. Because of that, the small particles rather jumped to the next position. From (a)–(c) the gold particles were arranged by a tungsten tip to a triangular shape. (This experiment was also performed at the Kavli Institute of Nanoscience at TU Delft, The Netherlands.)

<sup>2</sup>The colloidal suspension of gold particles was bought from Ted Pella, Inc.

## 4.2. Manipulation and Attachment of Carbon Nanotubes to Tungsten Probe Tips

The smaller the tip diameter and the higher the aspect ratio of etched tungsten tips gets, the more susceptible they become for mechanical damage, mostly bending. A different approach to get high aspect ratio tips is to modify a standard tip by attaching a carbon nanotube (CNT). Carbon nanotubes are known to have superior material properties in terms of their tensile strength and Young's modulus [26]. They are used to modify atomic force microscopy (AFM) tips [31] as well as tungsten probe tips [9]. Here, multi-walled carbon nanotubes (MWCNTs) with a diameter of about 80 nm were attached to a tungsten tip for high aspect ratio probing.

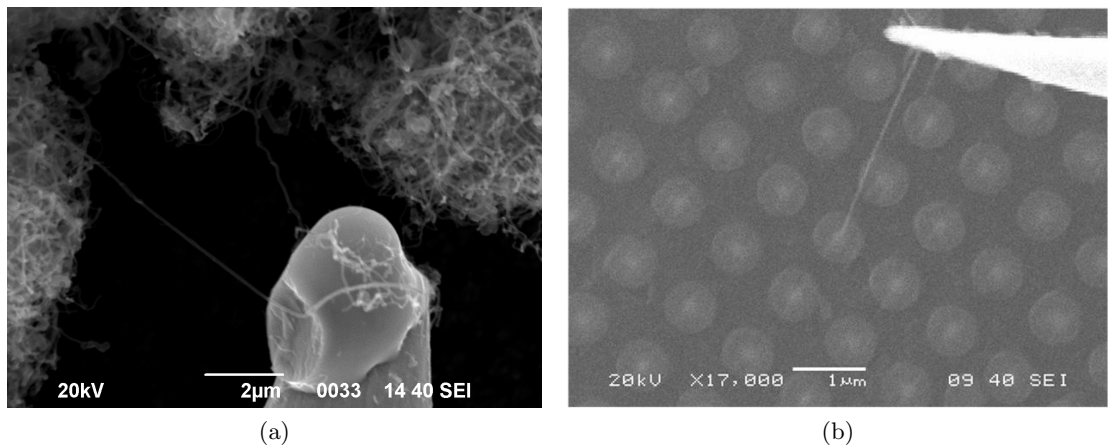


Figure 4.3.: Attachment of MWCNTs to tungsten tips. (a) A bundle of MWCNTs with a protruding tube, that is connected by van der Waals forces to a tungsten tip. (b) A MWCNT with a diameter of around 80 nm was attached to a tungsten tip. The high aspect ratio and the superior mechanical properties of CNTs turn them into very well suited probe tips. In this case a sample with standing, multilayered nanowires was electrically probed.

An agglomeration of commercial available MWCNTs was placed on adhesive tape inside the SEM chamber and a tube protruding from the bundle was selected. The probe tip was then brought into contact with the MWCNT. Such a process is shown in Figure 4.3a. The relative position of tip and tube can be estimated by focussing on each object and the correspondent difference of the working distance. Once they touch each other, the van der Waals forces will assist in establishing a rather stable connection. By skillful manipulation of the tip, the MWCNT was aligned along the tip shank. The larger the contact area, the stronger the connection will be. In Figure 4.3b a MWCNT with a diameter of around 80 nm is attached to a tungsten tip. The modified probe tip was used to contact individual layers of standing, multilayered nanowires.

This connection is often enough for pulling the MWCNT out of the bundle and

overcome the attractive forces between the tubes itself. For improving the mechanical stability of the tube-tip connection, electron beam induced deposition (EBID) can be used [9]. Gaseous molecules are dissociated by the electron beam and adsorbed onto a nearby surface. If the electron beam is set to high magnification and focussed on the tube-tip contact area, carbonaceous material is deposited and enforces the mechanical connection.

### 4.3. Two-terminal Measurements on Tungsten Nanowires

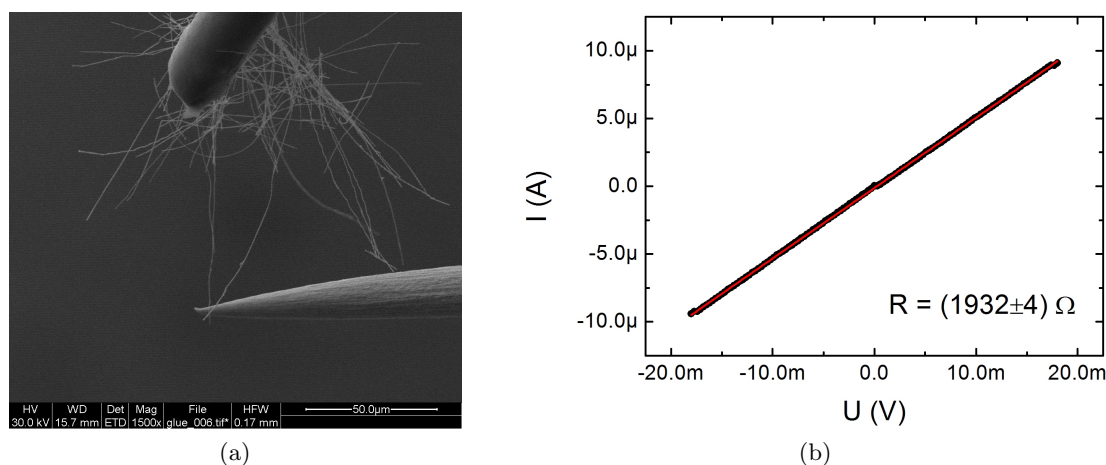


Figure 4.4.: Attachment of tungsten nanowires to tungsten tips. (a) Image of a nanowire suspended between two tungsten tips. In that way a two-terminal electric contact was established. (b) The ohmic current-voltage characteristic of a suspended tungsten nanowire (black circles) and the linear fit (red line). The two-terminal resistance is  $R = (1932 \pm 4) \Omega$ . The contact resistance of the two nanowire-tip connections could not be determined.

Single crystalline tungsten nanowires, that were prepared from directionally solidified NiAl-W alloys by a chemical release from the resulting binary phase material [7], were examined.<sup>3</sup> Similar to picking up MWCNTs by tungsten tips, tungsten nanowires with a nominal diameter of 200 nm were attached to tungsten tips. One tip was driven into a network of nanowires and pulled out again. Some nanowires stuck to the tip and could then be contacted by a second tungsten tip (see Figure 4.4a). In that way, a two-terminal electric contact could be established and a current-voltage characteristic was measured (see Figure 4.4b). The two-terminal resistance was calculated from the fitted slope to  $R = (1932 \pm 4) \Omega$ . From the known bulk resistivity of tungsten ( $\rho_W = 5.6 \cdot 10^{-8} \Omega\text{m}$ ), the resistance of a cylindrical nanowire of length  $l = 100 \mu\text{m}$  and diameter  $d = 200 \text{ nm}$

<sup>3</sup>The nanowires were provided by Andrew Jonathan Smith (Max-Planck-Institut für Eisenforschung, Düsseldorf).

can be calculated by the ohmic law to  $R = \rho_W l / \pi d^2 = 180 \Omega$ . To eliminate the contact resistance of the two tip-nanowire connections, a 4-point probe configuration was tried to establish. The attempts failed, due to the weak cohesive forces and the rather unflexible nanowire.

## 5. Making Small Contacts

To perform electrical measurements on small objects or devices one has to establish an electric contact between the microscopic device and the macroscopic measurement instrument first. This chapter considers making contact to nanostructures from a theoretical and an experimental point of view.

### 5.1. Theoretical Basics of Electrical Contacts

In this subsection, we want to discuss the different regimes when we approach and make electric contact to a conducting surface with a probe tip.

#### 5.1.1. Field Emission

If the tip is far from the substrate, it is possible to observe a current due to field emission. External electromagnetic fields can induce the emission of electrons from solids, liquids or atoms, by changing the potential barrier at the surface. The potential barrier is lowered and gets a finite width, so that the electrons can tunnel through the barrier with a certain probability, which depends on the potential barrier and the energy state of the electron. A simplified quantum mechanical calculation of the emission current density  $j$ , where the non-relativistic time-independent Schrödinger equation in one dimension is solved for a triangular potential, leads to the following Fowler-Nordheim equation [18]

$$j(E) = \frac{c_1 \cdot E^2}{\Phi} \cdot \exp\left(\frac{-c_2 \cdot \Phi^{\frac{3}{2}}}{E}\right), \quad (5.1)$$

where  $E$  is the electric field strength,  $\Phi$  is the potential barrier height,  $c_1$  and  $c_2$  are constants.

The process of field emission is also used to produce high current density electron sources, i.e. in field emission guns for electron microscopy (see chapter 2).

#### 5.1.2. Tunnel Contacts

If the distance between the probe tip and the sample surface is small enough that the electron wave function extends over the potential barrier of the gap into the sample surface, there will be a finite chance for the electron to tunnel through the barrier. Eligible distances are typically in the sub-nanometer regime. The gap can be vacuum or an insulating material like a non-conducting oxide. An applied voltage will lead to a net current flow, the tunnel current.

The solution of the Schrödinger equation for a rectangular potential barrier gives an exponential decay of the electronic wave function. The tunnel current as sum over the tunnel probabilities of all electronic energy levels shows therefore an exponential dependence of the width of the barrier and the distance between tip to sample surface, respectively. Tunnel contact resistances are typically in the range of megaohm to gigaohm.

### 5.1.3. Quantum Point Contacts

Reducing the distance further, the probe tip will eventually make contact to the sample surface. In the smallest limit, the contact is monatomic. For such point contacts, the electron mean free path is larger than the dimension of the contact area, meaning there are no scattering events for the electron across the constriction (ballistic transport). If the Fermi wavelength is comparable to the width of the one-dimensional constriction, the contact is called a quantum point contact. The transverse confinement of the electronic wave function results in a quantization of the electron transport. Every mode of the quantum point contact can only be occupied by one electron simultaneously (Pauli principle) and accounts to the total resistance by the resistance quantum given by the Klitzing constant  $R_K = h/e^2$  ( $\approx 25.81$  k $\Omega$ , without spin degeneracy), with Planck's constant  $h$  and the elementary charge  $e$ . This leads to the typical steps in the conductance<sup>1</sup>

$$G = n \cdot \frac{2e^2}{h} \quad (5.2)$$

at multiples  $n$  of the quantum conductance  $G_0 = 2e^2/h$ , when changing a parameter which controls the number of allowed transport modes [1]. In the experiment, this parameter can be the displacement of a scanning tunneling microscope tip, which is retracted from a metal surface [17]. Another established method is the use of a mechanically controllable break junction (MCBJ) [1]. There, a thin metal wire is mounted on top of a supporting structure. Upon bending the supporting structure, the thin metal wire stretches and will undergo several stages of deformation until it eventually breaks. Shortly before rupture, the constriction will consist of one or a few atoms and behave as a quantum point contact. Because the exact rearrangement of the atoms will differ from experiment to experiment, the results are not perfectly reproducible. Commonly, this is compensated by repeating the experiments many times and plotting the measured conductance in a histogram for statistical evaluation. Apart from the deviations from the integer conductance quantization in the experiments, the atomic contacts are also unstable in time due to spontaneous structural rearrangements. Especially at small contact areas, the high current densities will lead to electromigration. Electromigration is the transport of material caused by the gradual movement of the ions in a conductor due to the momentum transfer between conducting electrons and diffusing metal atoms.

---

<sup>1</sup>In this community the conductance is rather used than the resistance.

#### 5.1.4. Sharvin Point Contacts

If the thermal energy  $k_B T$  is greater than the energy level spacing of the different modes that propagate through the channel, the quantized conduction is washed out. If transport is still ballistic, i.e. the mean free path is larger than the dimension of the contact, the contact is called a Sharvin contact [13]. Its resistance is given by the Sharvin resistance [1]

$$R_S = \frac{h}{2e^2} \left( \frac{2}{k_F \cdot a} \right)^2, \quad (5.3)$$

where  $k_F$  is the Fermi wave vector and  $a$  the contact radius. Note that the Sharvin resistance depends only on the electron density (through  $k_F$ ), and is independent of the resistivity of the material. Quantum mechanics enters only through Fermi statistics in the derivation of this formula. In this domain, values of the contact resistance are still in the kilohm regime.

#### 5.1.5. The Classical Holm Resistance

Increasing the contact area leads to a transition from the point contact regime to the classical Holm contact regime (sometimes also called Maxwell regime), where the contact radius becomes much larger than the electron mean free path [13] and the current transport can be treated classically.

At such an electrical junction, the electrical current lines are distorted close to the contact interface, as they have to bundle to pass through the small contact spots. This constriction of the electrical current increases the electrical resistance (constriction resistance).

For a circular contact area with radius  $a$  of two semi-infinite solids with electrical resistivities  $\rho_1$  and  $\rho_2$ , the constriction resistance is [22]

$$R_C = \frac{\rho_1 + \rho_2}{4a}. \quad (5.4)$$

For non-circular contact areas, the constriction resistance will generally be smaller if compared to a circular contact spot with identical area. More realistic shapes of the asperities that form the contact spots give rise to a higher value of constriction resistance. If, for instance, one contact member is of conical shape making an angle  $\theta$  with a flat surface (in the limit of a much smaller contact spot radius compared to the cone length), the constriction resistance becomes [36]

$$R_\theta = \frac{\rho}{4a} \cdot \tan \left( \frac{\pi + 2\theta}{4} \right). \quad (5.5)$$

Applied to a circular contact spot between a conical tungsten tip and a flat gold surface, the contact resistance due to the constriction is then

$$R_C = \frac{\rho_W}{4a} \cdot \tan \left( \frac{\pi + 2\theta}{4} \right) + \frac{\rho_{Au}}{4a}. \quad (5.6)$$

For a radius  $a$  of 100 nm and an angle  $\theta$  of  $45^\circ$  the contact resistance is  $R_C = 0.39 \Omega$  ( $\rho_{Au} = 2.2 \cdot 10^{-8} \Omega\text{m}$ ,  $\rho_W = 5.6 \cdot 10^{-8} \Omega\text{m}$ ; values from [8]).

In practice, an electrical junction will have many contact spots. The contact resistance is then determined by the number and the dimensions of the contact spots as well as the grouping [36]. In the simplest case of circular contact spots with large distances between each other, the total constriction conductance  $1/R_C$  is simply the sum of the individual conductances.

The area of mechanical contact  $A_C$  between two contacts is related to the load  $F$  applied to the electric interface. Under the assumption that contact pressures on contacting asperities are equal to the hardness  $H$  of the softer of the two materials, the normal load is supported by plastic flow of the softer asperities [36]:

$$F = A_C \cdot H. \quad (5.7)$$

With  $A_C = \pi a^2$  and Eq. 5.7 the constriction resistance  $R_C = \rho/2a$  can also be expressed by

$$R_C = \frac{\rho}{2} \sqrt{\frac{\pi H}{F}}. \quad (5.8)$$

Surface films at the interface of an electrical junction modifies the contact resistance in various ways. Conducting films can increase or decrease the constriction resistance, depending on the electrical resistivity of the film material relative to that of the substrate. This process is often used on purpose (electroplating) to improve electrical contact resistance as well as protect the contact surface against oxidation, corrosion, tarnishing and mechanical wear. The growth of intermetallic layers at a bimetallic interface usually results in an increase of contact resistance and a decrease of mechanical strength of the contact. To mitigate the growth of an intermetallic layer, an appropriate diffusion barrier can be introduced at the interface. Oxidation or corrosion on contact surfaces lead often to electrically insulating or weakly conducting surface films. To establish an electrical contact, the film has to be fractured, so that metal-to-metal contact spots are formed. Thus, the electrical contact resistance depends strongly on the applied load.

Solid materials have generally a rough surface on the microscale. When two such rough surfaces are brought into contact, the true mechanical contact will only occur at discrete spots and be much smaller than the nominal geometrical contact area over a large range of contact loads. In intermetallic contacts, the surfaces are often covered with an oxide or insulating layers. In this case, the area of true electrical metal-to-metal contact will be even smaller than the area of true mechanical contact, because electrically insulating films have to be ruptured at the contacting asperities first.

### 5.1.6. Temperature Dependence of Contacts

When current passes through a contact, the temperature is highest at the narrowest part of the constriction. Holm considered heating in the case where the diameter of a circular contact is larger than the electron mean free path and both sides of the contact are made

from the same material. Further he assumed that the metal that forms the contact obeys the Wiedemann-Franz Law [25], which states that the electrical conductivity  $\sigma$  is related to the thermal conductivity  $\kappa$  as

$$\frac{\kappa}{\sigma} = L_0 \cdot T. \quad (5.9)$$

Here  $T$  is the temperature and  $L_0 = 2.44 \cdot 10^{-8} \text{ V}^2/\text{K}^2$  is the Lorentz number. Under these assumptions, the relation between the applied voltage  $U$  and the maximum temperature at the center of the contact  $T_{max}$  is [22]

$$T_{max}^2 = T_0^2 + \frac{U^2}{4L_0}. \quad (5.10)$$

Here  $T_0$  is the temperature of the leads far away from the contact. Fairly modest applied voltages can cause the metal to melt at the constriction. The melting voltages for some materials are: Al=0.3 V, Ni=0.16 V, Cu=0.43 V, Ag=0.37 V, Sn=0.13 V, Au=0.43 V, W=1.1 V, Pt=0.65 V [36].

If the transport behavior becomes ballistic (Sharvin contact), Eq. 5.10 breaks down and the observed temperatures are lower than expected [40]. The reason is the onset of the largely temperature independent Sharvin resistance. In a simple model, the resistance of a small constriction consists of a classical resistance component and the Sharvin resistance (series resistances). They form a voltage divider, so that only a part of the voltage drops at the Holm resistance and participates in heating in Eq. 5.10.

### 5.1.7. Summary of the Contact Resistance Regimes

In general the size of the contact area in comparison to the mean free path, respectively the Fermi wavelength of the electrons determines the order of magnitude of the contact resistance. The different resistance regimes, that were discussed, have distinct physical transport mechanisms. The smaller the contact area gets, the higher the contact resistance will be. The lowest values for the contact resistance  $R_C$  can be reached in the Holm regime ( $R_C < 1 \Omega$ ), followed by the Sharvin regime ( $0.1 \Omega < R_C < 10 \text{ k}\Omega$ ), the quantum point contacts ( $R_C = 25.81 \text{ k}\Omega$  per channel) and the tunneling contact regime ( $10 \text{ M}\Omega < R_C < 10 \text{ G}\Omega$ ).

## 5.2. Experimental Problems and Solutions for Electrical Probing of Micro- and Nanostructures

Performing electrical measurements on a sample, you normally want low-ohmic contacts between the probe tip and the sample. In section 5.1 we saw, that a good contact into a metal film has a certain minimum area. Having small contact areas when probing micro- and nanostructures, this goal is difficult to achieve and you often end up with high resistance contacts.

Additionally, contact resistances of small contact areas tend to be unstable in time and

present a major difficulty for the experimenter. Reasons for instability can be corrosion, mechanical vibrations, surface diffusion and - especially due to the high current densities in the small contact areas - electromigration [21], thermal expansion and electrical forming [2].

### 5.2.1. Examples of Unstable Contacts

In order to demonstrate the behavior of unstable electrical contacts, a thin gold film electrode was contacted by two aged tungsten tips and a low bias of 0.5 V was applied between the tips. The time dependence of the measured current is shown in Figure 5.1. The current decreases from 0.46 mA to 0.2 mA over the duration of around two hours, after which a sudden drop to zero current occurred. The optical inspection showed afterwards a hole in the thin gold film, where one tip was in contact before. Interestingly, the current was not decreasing monotonically.

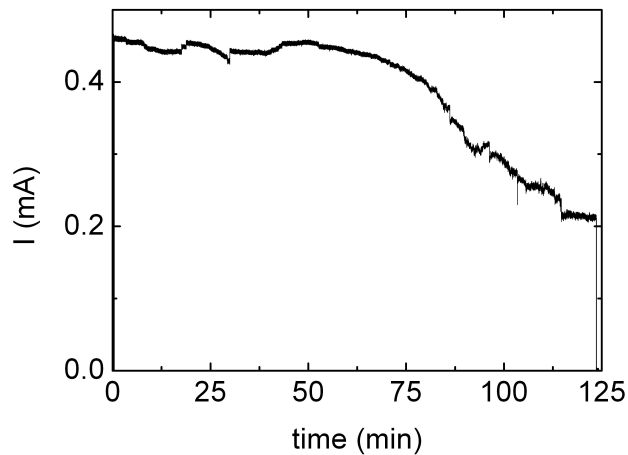


Figure 5.1.: Unstable contact between tungsten tips and a thin gold film in a two-terminal measurement setup. The plot shows the time dependence of the measured current at a bias of 0.5 V.

By applying a higher bias, the contact can be improved. Figure 5.2a shows the current (black line) and the applied voltage (red line) over time. The voltage was stepwise increased to 10 V. After some minutes the current became stable at the higher bias. The bias voltage was then decreased again and the current followed rather linearly till 6 V (see Figure 5.2b). At lower bias the current showed again fluctuations and the overall tendency of getting smaller due to increasing contact resistances. The reason for the contact improvement is possibly due to electromigration and melting processes at the contact interface at higher current densities.

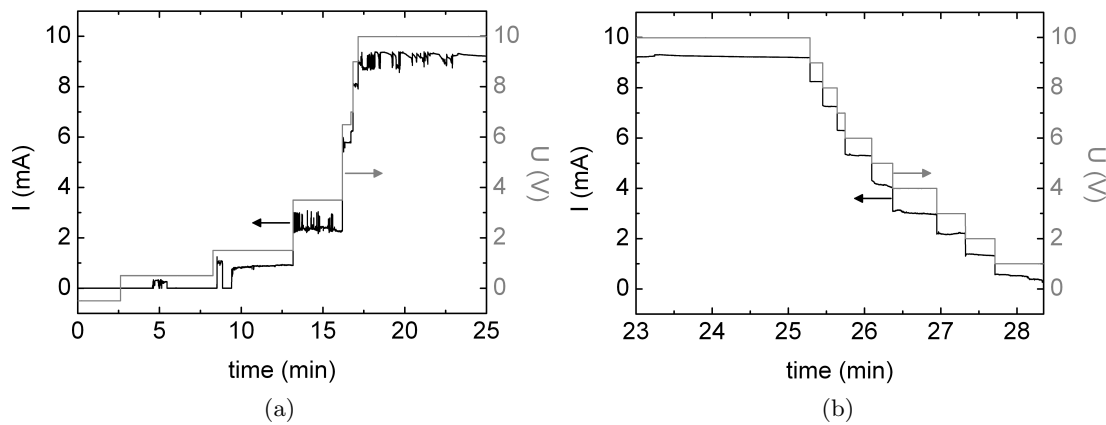


Figure 5.2.: (a) Unstable contact between tungsten tips and a thin gold film in a two-terminal measurement setup. The plot shows the time dependence of the measured current at a bias of 0.5 V. (b) Improving an unstable electrical contact by increasing the applied bias. After ramping the bias (gray line) up to 10 V for some time, the current (black line) gets much more stable.

### 5.2.2. Electrical Forming

For metal-semiconductor contacts, we used a similar procedure to lower the contact resistance. Two aluminum wires were placed close to each other on a bulk silicon surface with native oxide on the semiconductor (Figure 5.3a). The initial two terminal resistance between the two wires including the two aluminum-silicon contacts and the path through the silicon was nonlinear and on the order of gigaohm at low bias (supplied by the *SourceMeter 2636A*). Applying a voltage pulse of 200 V lead to a local heating at the contact spots and initiated the formation of an aluminum silicide alloy at the interface (see Figure 5.3b). The total resistance dropped to  $360 \Omega$  and was ohmic. Thus, the electrical forming process lead to an electrically stable low-ohmic contact. The silicon between the two aluminum wires was also structurally altered.

### 5.2.3. Tip Cleaning by Direct Current Heating

Depending on the choice of the tip material, there can be an isolating native oxide layer. On tungsten tips, which we often use, a few nanometer thin native oxide ( $\text{WO}_3$ ) is formed in air and acts as an insulating layer [12, 32]. Therefore a cleaning procedure inside the vacuum chamber is desirable.

One way to remove the oxide is by direct current heating. Two tips are crossed and a current of typically 0.2–0.3 A is forced through the tips. Due to the small contact area of the tips the current density becomes very high. (For a current of 0.1 A and a contact area of  $1 \mu\text{m}^2$  the current density is  $j = 10^{11} \frac{\text{A}}{\text{m}^2}$ .) The tips are heated till they are red glowing.

At temperatures above  $1470 \text{ }^\circ\text{C}$  the native oxide is removed [39]. One has to be careful

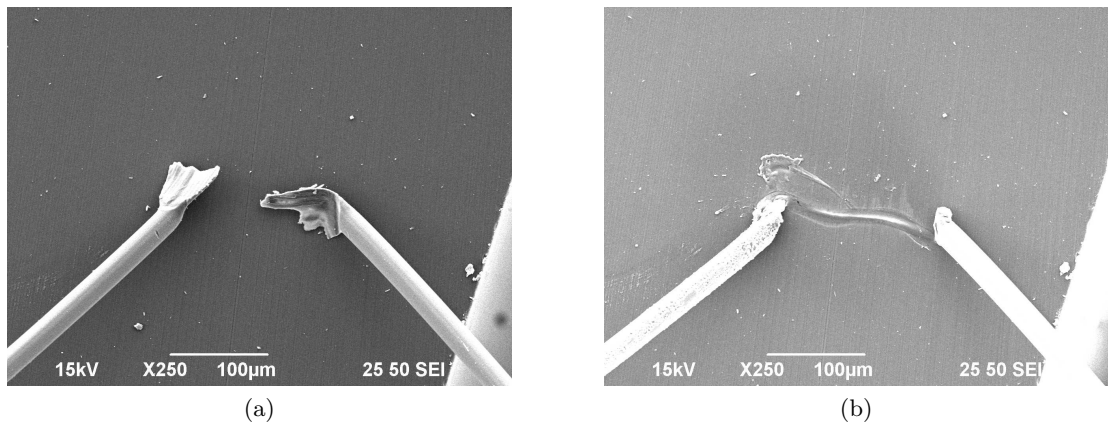


Figure 5.3.: (a) Two aluminum wires were placed on a silicon substrate. (b) A pulse of 200 V was applied and melted the tips to the surface. The electrical forming process lowered the two-terminal resistance to  $360 \Omega$ .

though to not overheat the material. This could melt the tips and make them unusable. Especially inside the scanning electron microscope (SEM) one has to be careful, because the temperature can not be estimated by observing the color of the thermal radiation. By cleaning a tungsten tip with this method the resistance between a thin chrome film and the tip was decreased by several orders of magnitude.

#### 5.2.4. Sharpening and Cleaning of Tips Inside the FIB

Another approach for in situ cleaning of a probe tip is by bombarding the tip with a focused ion beam (FIB). Due to the removal of tip material, the tip is also sharpened that way. In Figure 5.4b a secondary electron (SE) image of a sharpened tungsten tip is shown. The ion beam was directed from above parallel to the axis of the tip. The apex radius was dramatically reduced (compare to the size before the milling in Figure 5.4a).<sup>2</sup>

The sharpened tungsten tip was used to land inside micron sized square pits and measure the potential at the bottom of the pits (see Figure 5.5a). During probing the tip was accidentally plastically deformed, which happens very easily with this ultrathin tungsten tips (see Figure 5.5b).

#### 5.2.5. Mechanical Scratching

Another way to improve the electrical contact is removing oxide layers or other contaminations by mechanical forces. Scratching the tip several times over a contact pad can already lead to a much better contact. But the method is not material selective: Scratching through an oxide implies also damage to the tip and the sample surface. Therefore, this method is for thin layers or soft materials often not applicable. Also,

<sup>2</sup>The FIB milling experiments on the FIB were performed by Harald Plank, FELMI (TU Graz).

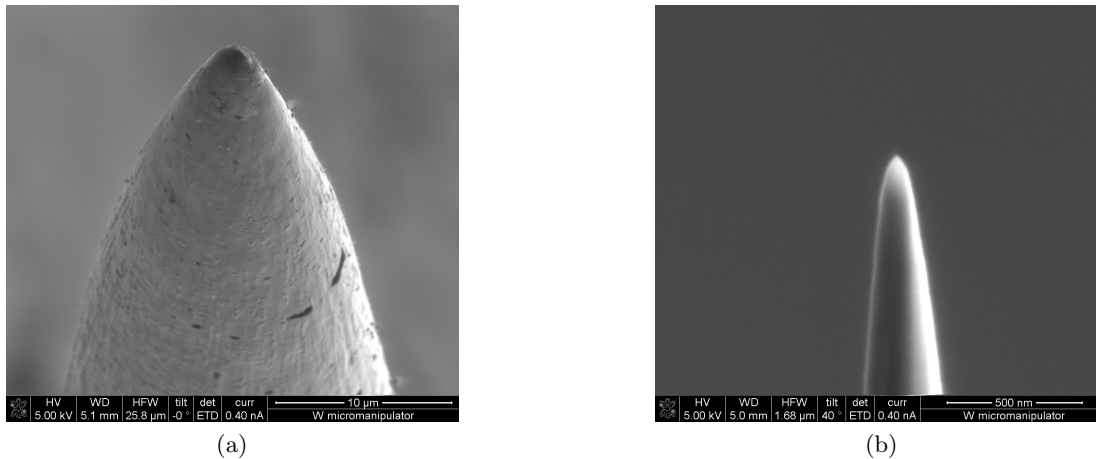


Figure 5.4.: (a) SE image of a commercially available tungsten tip (scale bar: 10 μm). (b) The tip apex after FIB milling of the tip (scale bar: 500 nm). The tip was thinned and sharpened and at the same time cleaned through oxide removal.

if the tip shape plays an important role - especially if one needs a very sharp tip and does not want to risk to bend the tip - one needs a different approach. The problem of oxidized tips can be reduced or prevented by choosing a suitable tip material. For instance, inert metals like gold can be used as tip material to prevent oxidation.

### 5.3. Conclusion

Probing in the micro- and nanometer regime leads to small contact areas. Dependent on the size and character of a contact, a wide range of interesting physical phenomena can be studied. In general one can say, the smaller a contact area is, the higher the contact resistance will be. For the characterization of small devices, the strong contribution of the contacts to the total electrical behavior can be inconvenient. Also, for decreasing contact areas, the contacts often become unstable.

Several methods for lowering the contact resistance were presented in this chapter. By forcing higher current densities through the contact, contact resistances were improved due to electromigration and electrical forming. Oxide layers, which prevented a low-ohmic contact, were removed by current heating and FIB milling. Scratching a probe tip over the contact surface can also lower the contact resistance, because of the removal of existing oxides or contaminants at the interface. A sound choice of the tip material can even prevent some of the mentioned problems. Depending on the situation, one or more of the discussed possibilities are applicable.

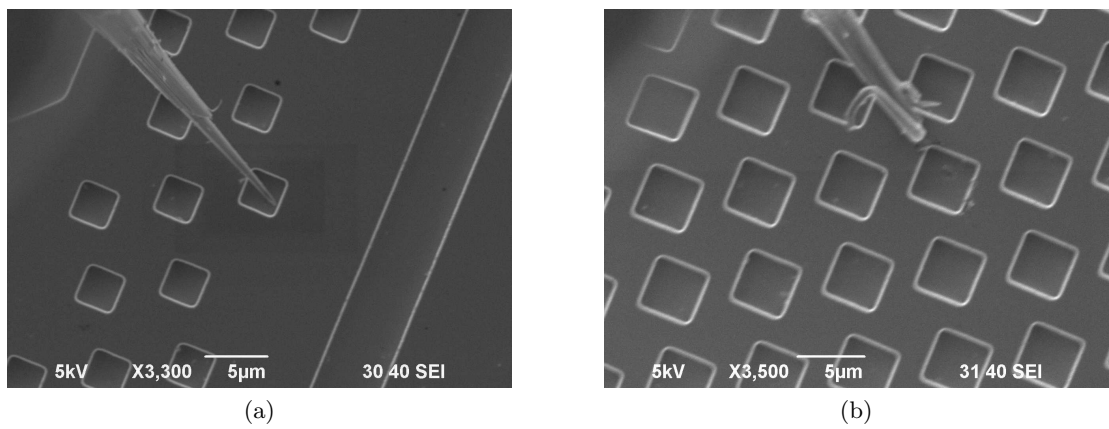


Figure 5.5.: (a) The sharpened tungsten tip was used for landing and probing in small micron sized pits. (b) The ultrathin tungsten wire was bent during probing through plastic deformation.

## 6. Multi-Probe Measurements

For the determination of the resistance of a device a simple two-terminal measurement is often used (typical for multimeters). If measured this way, the resultant resistance is the sum of the intrinsic resistance of the device itself, the resistances of the contacts, cables and the internal resistance of the multimeter. One way to eliminate these “parasitic” resistances and only measure the intrinsic resistance is to use a four-terminal measurement with two outer current probes and two inner voltage probes. In principal, this technique could be used to measure the electrostatic potential of a sample by changing the position of one voltage probe, if the contact resistances of the current probes are stable in time. In order to correct for unstable contacts, a five-point electrical measurement was employed and maps of the electrostatic potential as a function of position were directly measured.

Sometimes it is not desirable or possible to contact a sample with five probes. For these cases a three-terminal setup was developed, where we can also determine the electrostatic potential as a function of position. Basically, one measures, how the current splits across the sample if a voltage is applied between the tips.

In this chapter three-point and five-point scanning measurements are presented on a range of different devices.

### 6.1. Scanning Five-Point Electrical Measurements

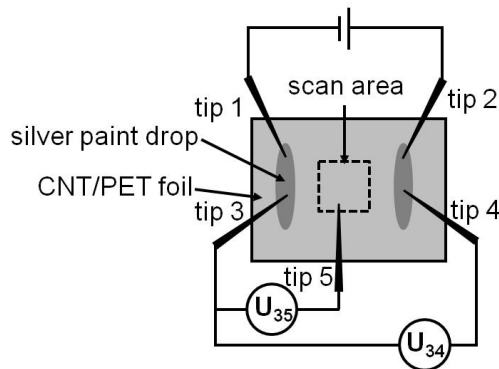


Figure 6.1.: Schematic drawing of a five-point measurement on a CNT covered PET foil. A current is sourced between tips 1 and 2. The ratio of the voltages  $U_{34}$  and  $U_{35}$  is measured as a function of position of tip 5 on the sample. Silver paint was used to improve the electric contact of tips 1–4 .

A five-point electrical measurement procedure was applied to a polyethylene terephthalate (PET) foil covered with carbon nanotubes (CNTs). Two parallel silver paint lines, with a gap of around  $130\ \mu\text{m}$  between them, were drop cast on the sample. Two tips were positioned on each of the lines. One tip on each line was connected to the LO-, respectively HI-, output of one channel of the *SourceMeter 2636A*, forcing a current through the CNT/PET foil. A second tip on each silver paint contact was used as a voltage probe. Tip 5 was used as the scanning tip, which measured the voltage as a function of position. Figure 6.1 shows a schematic drawing of the measurement setup.

The voltages were measured with the *ADwin*. Voltage follower had to be put between the voltage probes and the *ADwin* because of the high impedance of the device. In order to use the positional encoders of the *LT6820* substage and determine an absolute position, the substage was moved together with the sample and tips 1–4 to perform the lateral two-dimensional scan, instead of moving the scanning tip 5. The scanning tip (tip 5) was mounted on the top mounting ring in the scanning electron microscope (SEM) chamber, so that the substage could be moved independently of tip 5. After each step with the substage, tip 5 moved down until electric contact was established. The voltages  $U_{34}$  and  $U_{35}$  were measured. Afterwards tip 5 was lifted and the substage would travel to the next position. During the measurement the voltage  $U_{34}$  was monitored, in case one of the contacts would loose contact and the execution could be stopped. For the automated approach detection the modified voltage follower circuit was used for tip 5 with the Lock-In amplifier acting as the approach sensor (see section 3.4).

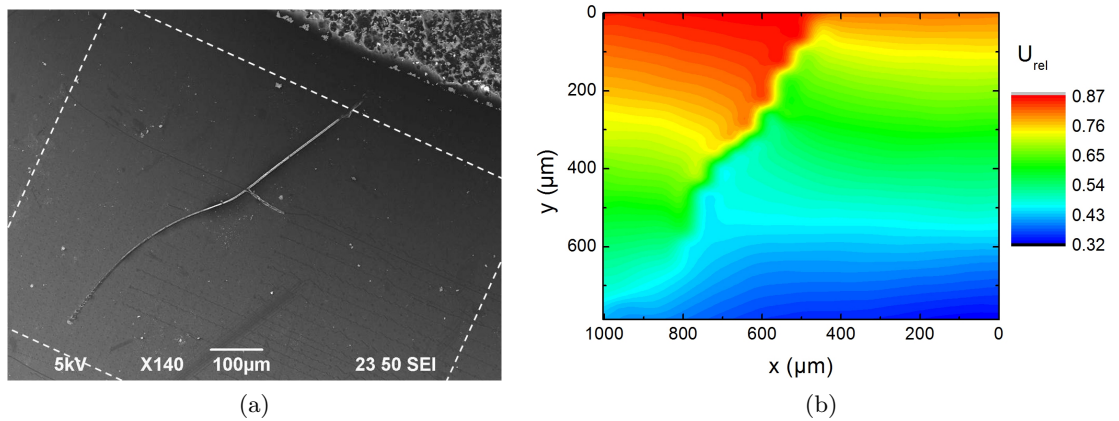


Figure 6.2.: Five-point measurement of the lateral potential distribution on a CNT covered PET foil. (a) The SE image of the CNT/PET foil taken after the measurement. On the upper right the edge of a silver paint contact is visible. The boundary of the scan area of the potential measurement is indicated by the white dotted line. Landing marks as well as long scratches of the scanning tip are visible. (b) Plot of the potential  $U_{rel} = U_{35}/U_{34}$  as a function of position. A crack in the foil, visible in (a), disturbs the potential distribution strongly.

The SE image of the CNT/PET foil is shown in Figure 6.2a. A part of one silver paint contact is visible in the upper right corner. The boundary of the scan area is indicated by the dotted white line. A crack in the foil runs through the scan area. The image was taken after the measurement. The puncture marks, that can be seen in the image, are imprints of the tip landings of this measurement and scans before. Additionally, there are lines scratched into the foil, when the scanning tip was too low during the lateral scan. Especially when the substage moves from the end of a scan to the start of the next line scan, a tilt between the plane of the foil and the plane of the substage leads to a substantial height difference at the position of tip 5. The measured potential  $U_{rel} = U_{35}/U_{34}$  is plotted in Figure 6.2b as a function of position. The crack in the foil influences the potential distribution strongly.

## 6.2. Scanning Three-Point Electrical Measurements

### 6.2.1. Resistance Determination Method

To measure the electrostatic potential as a function of position, one probe tip can be scanned while the others are held fixed. Making stable electrical contact with a scanning tip is often problematic. The contact area is small so the contact resistance tends to be large and unstable in time. It is therefore important to measure the contact resistance. This was done using a three point measurement where the currents flowing through all three tips were determined at every location.

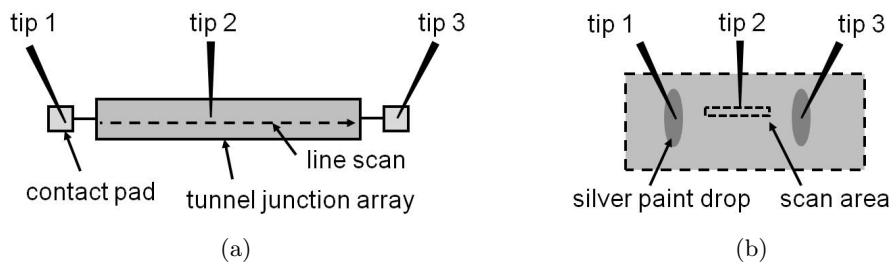


Figure 6.3.: Schematic diagram of scanning three-point electrical measurements on a 2D Josephson tunnel junction array. (a) The whole device is scanned parallel to the long axis of the tunnel junction array. Tips 1 and 3 are positioned on contact pads that are connected to the sides of the array. The array has a size of  $3 \text{ mm} \times 0.4 \text{ mm}$ . (b) Tip 2 is scanning a rectangular area (approximately  $170 \text{ }\mu\text{m} \times 1 \text{ }\mu\text{m}$ ) of the tunnel junction array. The scanning tip applies a voltage and the currents through tip 1 and 3 are measured. Silver paint improves the electric contacts between the sample and tip 1 and 3.

Figure 6.3a shows the schematic diagram of a three point measurement where tip 2 was scanned (single coarse steps with axis A) across the sample while the positions of

tips 1 and 3, positioned on contact pads at each side, were held fixed. A 2D Josephson tunnel junction array was used as a test structure (for details see [41]). The array had a size of  $3 \text{ mm} \times 0.4 \text{ mm}$ . It consists of individual Josephson tunnel junctions with a size of about  $3.5 \text{ } \mu\text{m} \times 2.5 \text{ } \mu\text{m}$ , that are connected to four neighboring tunnel junction islands. Figure 6.4a is an SE image showing a section of the Josephson tunnel junction array. The short sides of the array were connected to contact pads (gold).

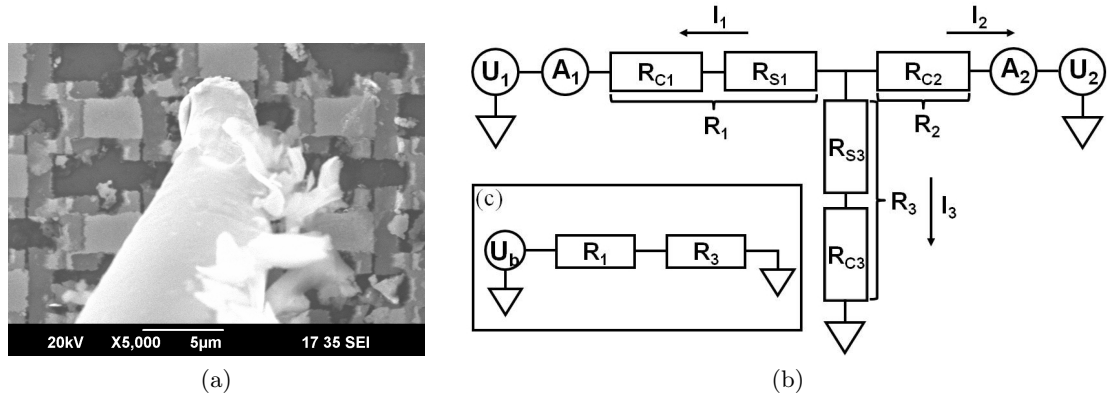


Figure 6.4.: Scanning three-point electrical measurement. (a) Secondary electron image of a section of the 2D Josephson tunnel junction array and the scanning tungsten tip (tip 2) is shown at high magnification. Tip 2 was scanned across the whole device and the resistances and the potential distribution were measured. Tip 1 and 3 were positioned on contact pads that are connected to the sides of the array. (b) The equivalent electrical circuit of the measurement setup in (a). The contact resistances  $R_{C1}$  and  $R_{C3}$  are constant, the sample resistances  $R_{S1}(x)$  and  $R_{S3}(x)$  are dependent on the position of tip 2. The contact resistance  $R_{C2}(x)$  of the scanning tip depends on the exact landing position and pressing force. (c) Equivalent circuit for the two-terminal measurement without tip 2.

The electrical measurements on this sample were performed in the light microscope probe station. During the measurement, tip 3 was grounded and small voltages  $U_1$  and  $U_2$  were applied to tip 1 and tip 2. The currents through tip 1 and 2 were measured and the current flowing through tip 3 was known from current conservation  $I_3 = -(I_1 + I_2)$ . The equivalent electrical circuit is shown in Figure 6.4b. The resistance  $R_1$  includes the contact resistance  $R_{C1}$  at tip 1 as well as the sample resistance  $R_{S1}$  between tip 1 and tip 2. The resistance  $R_3$  includes the contact resistance  $R_{C3}$  at tip 3 as well as the sample resistance  $R_{S3}$  between tip 2 and tip 3. However, the resistance  $R_2$  only includes the contact resistance at tip 2. The sample resistance does not contribute to  $R_2$ .

It is possible to determine all three resistances by performing two measurements. In the first measurement,  $U_1 = 0$  and  $U_2 = U_b$  so that the current, that flows from the source  $U_2$ , splits between the two resistors  $R_1$  and  $R_3$ . Consequently

$$\begin{aligned}
 R_1 I_1 &= R_3 I_3 \\
 \Leftrightarrow R_1 &= -\frac{I_1 + I_2}{I_1} R_3 = \alpha R_3.
 \end{aligned} \tag{6.1}$$

The circuit is then biased so that  $U_1 = U_b$  and  $U_2 = 0$ . The current that flows from source  $U_1$  splits between the two resistors  $R_2$  and  $R_3$ . This leads to the relation

$$\begin{aligned}
 R_2 I_2 &= R_3 I_3 \\
 \Leftrightarrow R_2 &= -\frac{I_1 + I_2}{I_2} R_3 = \beta R_3.
 \end{aligned} \tag{6.2}$$

These two measurements provide us with enough information to determine the three resistances and the potential  $U_2$  at the position of tip 2:

$$\begin{aligned}
 U_b &= -I_1 R_1 - I_1 \frac{R_2 R_3}{R_2 + R_3} \\
 \Leftrightarrow R_3 &= \frac{-1}{\alpha + \frac{\beta}{\beta+1}} \frac{U_b}{I_1}
 \end{aligned} \tag{6.3}$$

$$U_2 = U_b + I_1 R_1. \tag{6.4}$$

Figure 6.5a shows the result of a sequence of measurements where tip 1 and tip 3 were held at fixed positions while tip 2 was scanned between them. It is possible to make relatively firm and stable contact at the fixed tips but the scanning tip 2 makes light contact and the resistance varies greatly during the measurement (red circles in Figure 6.5a). Even though the contact resistance at the scanning tip 2 varies, it does not affect the measurement of the resistances  $R_1$  and  $R_3$ . Fitting the data points of the resistances  $R_1$  and  $R_3$  linearly in dependence of the position  $x$ , values for the contact resistances and the internal resistance of the sample could be evaluated. The contact resistances were  $R_{C1} = (157 \pm 4) \Omega$ ,  $R_{C3} = (180 \pm 4) \Omega$  and the total intrinsic resistance of the sample was  $R_S = (2068 \pm 4) \Omega$ . However, the result of the potential  $U_2$  shown in Figure 6.5b as black squares is strongly influenced by the fluctuation of  $R_2$ . If one is interested in the potential drop along the sample only contacted by tip 1 and tip 3 (see circuit diagram 6.4c), the potential progression is given by:

$$U(x) = U_b \frac{R_3(x)}{R_1(x) + R_3(x)}. \tag{6.5}$$

The result, calculated with the fit values of  $R_1(x)$  and  $R_3(x)$ , is plotted as a red line in Figure 6.5b. For large values of  $R_2$  ( $R_2 \gg R_3$ ) the parallel resistance  $\frac{R_2 R_3}{R_2 + R_3}$  approaches  $R_3$  and the values of  $U_2$  and  $U_{fit}$  coincide.

With the described three-terminal scanning tip measurement, the internal sample resistance and the contact resistances of all three tip-sample connections as a function

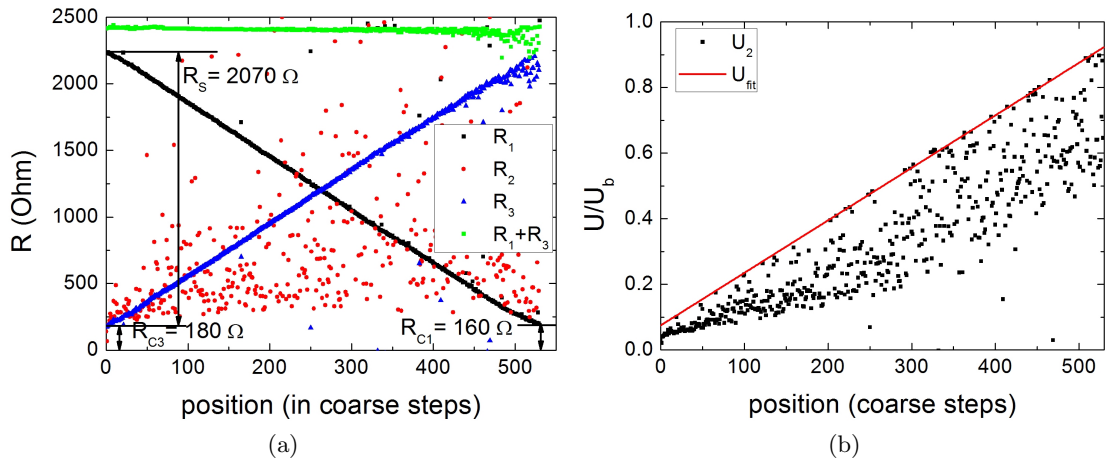


Figure 6.5.: Results of the scanning three-point electrical measurement. (a) The resistances  $R_1$ ,  $R_2$ ,  $R_3$  and  $R_1 + R_3$  as a function of position calculated from the measured currents  $I_1$  and  $I_2$  and the relations from Eq. 6.1–6.4. The resistance  $R_2$  of the scanning tip 2 varies greatly during the measurement (red circles). The contact resistances ( $R_{C1} = 160 \Omega$  and  $R_{C3} = 180 \Omega$ ) and the internal resistance of the sample ( $R_S = 2070 \Omega$ ) were evaluated by linear fit to the data points. (b) The potential at the position of the scanning tip  $U_2$  (black squares) as calculated with Eq. 6.4. The values fluctuate strongly due to the fluctuating contact resistance  $R_2$ . The red line is the potential progression calculated with  $U_{fit} = R_{3,fit}(x)U_b / (R_{1,fit}(0) + R_{3,fit}(0))$ . For large values of  $R_2$  ( $R_2 \gg R_3$ ) the parallel resistance  $R_2 R_3 / (R_2 + R_3)$  approaches  $R_3$  and the values of  $U_2$  and  $U_{fit}$  coincide.

of position could be measured. With these results, the potential distribution in the sample can be calculated without perturbation of the contacts.

## 6.2.2. Current Ratio Method

Since the resistance  $R_3$  is not needed to calculate the potential for the two-terminal configuration, the measurement can be simplified to just simultaneously measuring two currents once. If tips 1 and 3 are grounded while a voltage is applied to tip 2, the ratio  $r$  of the currents is  $r = I_1/I_3 = R_3/R_1$ . Equation 6.5 can be rewritten as:

$$U_{norm} = U(x)/U_b = \frac{1}{1+r}. \quad (6.6)$$

For mapping the potential with the latter method across a section of the device, tip 2 was scanned in a rectangular area (approximately  $170 \mu\text{m} \times 1 \mu\text{m}$ ) of the 2D Josephson junction array. The schematic geometry of the measurement is drawn in Figure 6.3b.

Tip 2 was scanned along 9 lines with 65 single coarse steps along axis A, that had a

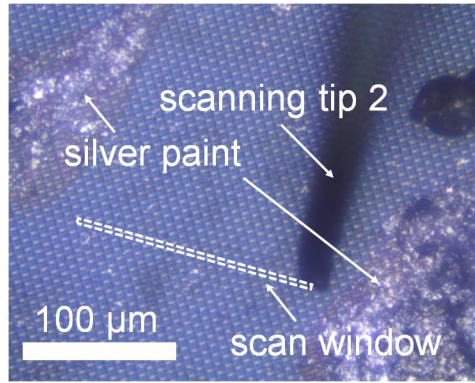


Figure 6.6.: A light microscope image of the configuration of a 2D scan of the electric potential of a 2D Josephson tunnel junction array. The voltage applying tip 2 was scanning a rectangular area (marked with dotted lines), while two stationary tips, positioned on silver paint drops visible in the image, were connected to current preamplifiers (*SR570*). A gold wire with a diameter of  $25\ \mu\text{m}$  was used as tip.

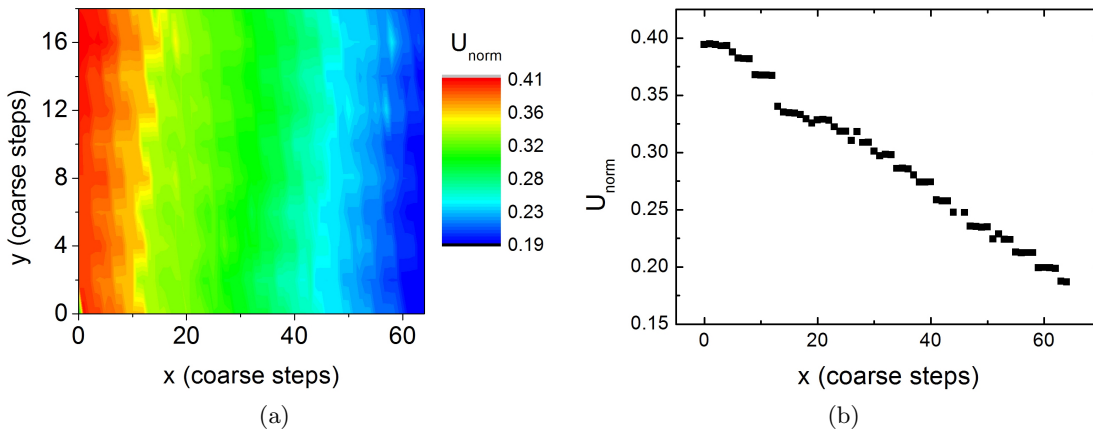


Figure 6.7.: (a) 2D plot of the potential measured by putting the source and drain probes on two nearby silver paint drops on the tunnel junction sample and measuring the potential as a function of position. The hysteresis of the coarse steps is visible in the potential map (spacing between two line scans was  $y = 2$  coarse steps). (b) shows a line scan for  $y = 4$  coarse steps. The plateaus correspond to individual tunnel junctions.

spacing of 2 coarse steps along the linear axis C of the manipulator. For a substantial potential difference along the scan the two stationary tips were positioned closer together. The contact to the sample was improved by two drops of silver paint (see Figure 6.6). Figure 6.7a is a plot of the measured potential calculated by Eq. 6.6, Figure 6.7b shows a line scan for  $y = 4$  coarse steps. The plateaus in the potential correspond to individual tunnel junctions. Because of the slanted scan window relative to the tunnel junction array the plateaus have different widths in the line scan. For the automation of the measurement, the landing of tip 2 was detected, if the measured current exceeded a threshold value. If the tip landed on an insulating part of the sample, it would descent further and slide onto the next tunnel junction, where the current is again big enough to overcome the limit. Because of this, the measurement process is only susceptible to the conducting parts of the sample. The lateral resolution is therefore of the order of  $1 \mu\text{m}$ , given the distances of the conducting islands and the size of the apex of tip 2. The hysteresis of the coarse steps scanning back and forth in a zig-zag pattern is reflected in the potential map. The spacing between two line scans ( $y = 2$  coarse steps) matches the shifts of the potential in x direction comparing adjacent line scans in the potential map in Figure 6.7a.

### 6.3. Three-Point Measurement of the Potential Drop Along a Single-Walled Carbon Nanotube

A collaborating group at the Korea Research Institute of Chemical Technology (KRICT) developed electrical transducers for biosensing applications. The adsorption or binding of charged biomolecules in these devices populates (or depletes) carriers in single-walled carbon nanotubes (SWCNTs). This appears as an increase (decrease) of the channel conductance. In the end, these sensors should detect the presence of tumor-associated markers so that they can be used as effective diagnostic tools for early cancers. To give selectivity to the nanotube based sensors, aptamers are used for molecular recognition. Aptamers are artificial oligonucleotides (DNA or RNA) that can bind to a wide variety of entities such as metal ions, small organic molecules, proteins, and cells with high selectivity and affinity, equal to or often superior to those of antibodies [27]. The aptamers can be isolated from combinatorial nucleic acid libraries by using in vitro selection methods. Synthesizing aptamers is relatively inexpensive, and they can be engineered easily for both immobilization and labeling purposes. These biosensors could be used repeatedly, because of the aptamers' capability of reversible denaturation.

In order to clarify the process of the conductance change upon adsorption or binding of biomolecules, the potential drop along a SWCNT on a test structure (provided by Jeong-O Lee, KRICT) was measured. The main question in this context was, if the conductance change stems predominantly from the adsorption of biomolecules at the nanotube/electrode interface or from the adsorption along the whole length of the nanotube.

Figure 6.8a is an SE image of the test structure. It shows two gold electrodes that are connected by a SWCNT. The bright spots are gold particles, that are attached to the

nanotube. The SWCNTs were grown by catalytic chemical vapor deposition on a  $\text{SiO}_2$

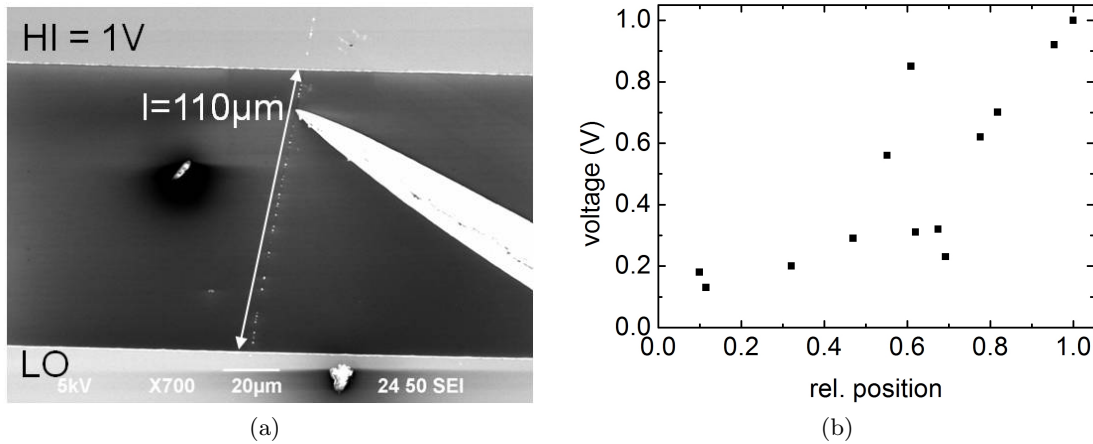


Figure 6.8.: Three-point measurement of the potential drop along a SWCNT. (a) Secondary electron image of a SWCNT. Attached gold particles provide a good visibility of the nanotubes despite their small diameter of a few nanometer. (b) Plot of the measured voltage, that was applied to the probe tip so that no current flowed, as a function of position along the SWCNT shown in (a).

substrate. Transverse to the growth direction, gold lines (electrodes) with a separation of  $100 \mu\text{m}$  were deposited by lift-off processing. Gold particles were attached along the nanotubes to increase the number of nanotube/gold interfaces, which have for the potential measurement no significance except an enhanced visibility of the SWCNTs in the SEM.

A different instrumental approach for measuring the potential along the tube as a function of position for a three-point probing configuration was used. Two tungsten tips were placed on adjacent gold lines. They were connected to the sourcemeter and a constant voltage of  $1 \text{ V}$  was applied, which lead to a current of  $0.8 \mu\text{A}$ . For measuring the potential along the tube, a tungsten tip was brought into contact with the SWCNT. The HI-output of the second channel of the sourcemeter (LO-output of channels A and B was shorted) was connected to this tip and applied a specific voltage, so that no current flowed through that tip. The applied voltage equals then the potential at that position. In that fashion, a series of measurements were performed along the SWCNT.

The measured voltages are plotted as a function of position (normalized to the total length of the nanotube) in Figure 6.8b. It can be concluded from these results, that the voltage drops fairly linearly along the SWCNT between the two electrodes and not mainly at the nanotube/electrode contact. The non-monotonic characteristic of the potential progression was caused firstly by the large imprecision of the measurement. Depending on the quality of the contacting, the reading error was in the range of  $0.01\text{--}0.1 \text{ V}$ . Secondly, an altering of the electric properties of the SWCNT during the

measurement due to mechanical stress can not be excluded. In order to establish an electric contact between tip and nanotube, the tip was pushed carefully over the substrate and across the SWCNT. Ultimately, the measurement was ended, when the tip cut the SWCNT accidentally in half, which demonstrates the mechanical load exerted on the nanotube.

In conclusion, the initial question, if the voltage drops mainly at the nanotube/electrode contacts, could be negated in this three-point measurement.

## 7. Structuring and Modification of Metal Lines and Thin Films

A difficulty in using sharp tips for making electric contact is that they sometimes cause damage to the sample due to electrostatic discharge or the high current densities that result from the very small contact areas. Here we describe some of these processes and describe how they can be used to purposely modify metal structures in a controlled way. Contact-breaking microspark erosion (CBME) was used to cut lithographically defined metal lines in an integrated circuit and electrical fusing of thin metal film was used to selectively remove metal from a photolithography mask.

### 7.1. Contact-Breaking Microspark Erosion

We tried positioning the needles just above a metal surface in vacuum and applied a high voltage so that a spark was created. The high voltage required results in a more energetic spark which creates too much damage and the process was much harder to control than the contact-breaking method. Using a relatively small current is important to ensure that the ablated area remains small. A simple scratching of the metal traces using the piezo-actuated micromanipulators proved ineffective. Scratching bends the ends of the needles without cutting through the metal films.

#### 7.1.1. Basics on Spark Generation upon Opening Electric Contacts

The fundamentals of arcs and interruptions in electric circuits cover a large area of applications. For the sake of brevity, we will focus on the formation of an electric spark during contact opening, which is the process used in the CBME experiments. The classical description (Holm regime) here follows [36], where a more complete discussion on the subject can be found.

From Eq. 5.8 the contact resistance is given by

$$R_C = \frac{\rho}{2} \sqrt{\frac{\pi H}{F}}, \quad (7.1)$$

where  $\rho$  is the resistivity,  $H$  the material hardness and  $F$  the load. Upon opening an electric contact ( $F \rightarrow 0$ ),  $R_C$  will increase and the electric current flowing through the contact will heat up the contact spot. Even at low applied voltages the temperatures at the contact spot reach the melting point of the metal. As the contacts continue to part, a molten metal bridge is formed in between. When the bridge is drawn further it becomes unstable due to surface tension effects, boiling of the highest temperature region and

convective flows of molten metal resulting from temperature gradients. Eventually, the bridge will break and release metal vapor into the gap. Already at low voltages the condition for ionization processes due to electron-atom and hot gas atom-atom collisions are fulfilled. If the electric field exceeds the breakdown condition, a spark is formed in the gap, due to an avalanche effect of the ionization processes. This electric discharge mechanism works also in vacuum because of the metal vapor of the contact material itself.

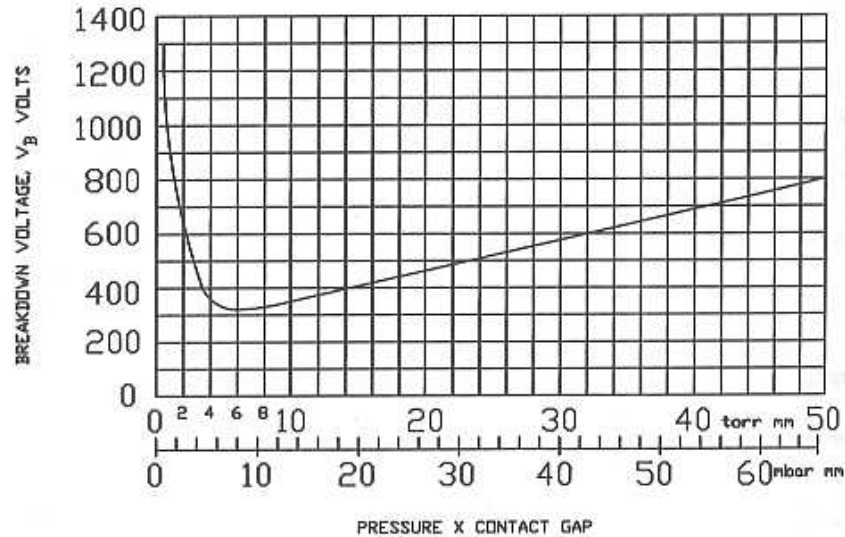


Figure 7.1.: Paschen curve showing breakdown voltages as a function of the product of pressure and gap distance for air filled gaps between plane and parallel electrodes [36, pg. 444].

The breakdown voltage  $V_B$  for a given gas is a function of the gas pressure  $p$  and the contact gap  $d$  (Paschen's law):

$$V_B = f(p \cdot d). \quad (7.2)$$

Figure 7.1 shows a Paschen curve for an air filled gap between two coplanar electrodes (taken from [36]). Note, that above the minimum breakdown voltage, two values of  $p \cdot d$  exist for a given  $V_B$ . Consider a fixed contact gap. In the high-pressure regime, the electrons rapidly lose energy through frequent collisions. In order to ensure the electric breakdown, the electric field  $E = V_B/d$  must be high enough that the electrons gain enough kinetic energy between collisions. The voltage  $V_B$  has to increase for increasing pressure. In the low-pressure regime, the electrons have large mean free paths and only few collisions, hence a small number of ionization events. To compensate for this when decreasing the pressure, the ionization probability of each collision and thus the electric

field strength needs to be increased.

### 7.1.2. Experimental Results

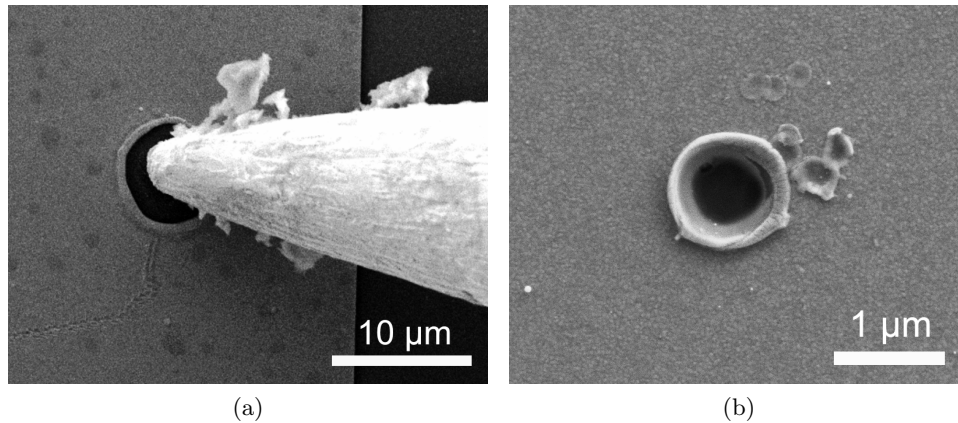


Figure 7.2.: (a) A five micron hole was produced in a 90 nm thick aluminum film by contact-breaking microspark erosion (CBME). A track can be seen where the tip was dragged across the metal prior to being lifted at the point where the hole is. Pieces of aluminum from holes made previously at other locations are seen on the tip. (b) A hole created in a 70 nm thick gold film by CBME. Note the smaller diameter of the hole compared to (a).

Small sparks between a tip and a conducting substrate can be generated by placing a 1 mH inductor and a 1 k $\Omega$  resistor in series with the needle and purposefully retracting the needle to cause a spark. Voltages of no more than 10 V were applied before the needle was retracted. Under these conditions, a maximum of  $5 \cdot 10^{-8}$  J of energy was stored in the inductor. When contact between the needle and the film was broken, the energy stored in the inductor created an electrical discharge that ablated the metal away near the point of contact. Figures 7.2a and 7.2b show holes made in aluminum and gold films using this method. The sparking process works in vacuum as well as in air and was used to modify metal structures inside a scanning electron microscope (SEM).

We call this cutting method CBME to distinguish it from a similar industrially applied process called electric discharge machining (EDM) [34]. In EDM, a spark is created between an electrode and a conducting workpiece. Typically, the distance between the electrode and the workpiece is about 300  $\mu\text{m}$  and the electrode never comes in electrical contact with the workpiece. The space between the electrode and the workpiece is filled with a dielectric fluid, either water or oil. The dielectric fluid cools the workpiece and carries away the ablated material. Although this is a well established technology for cutting metal, the voltages applied and the dielectric fluid make this process inappropriate for work in a SEM.

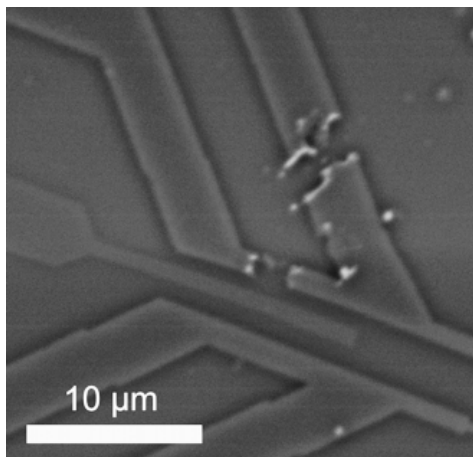


Figure 7.3.: A SEM image of two aluminum contact lines that were cut by CBME. The 1.5  $\mu\text{m}$  wide line was broken with one microspark, the wider line (3.5  $\mu\text{m}$ ) was cut with four microsparks.

Contact-breaking microspark erosion was used to cut two metal traces in an integrated circuit as shown in Figure 7.3. Cutting metal traces in an integrated circuit to isolate a subcircuit (like a transistor) is useful in failure analysis to determine exactly where an electrical fault is located. The thinner wire was a 1.5  $\mu\text{m}$  wide aluminum trace and was broken in a single spark. The wider trace was 3.5  $\mu\text{m}$  wide and required four sparks. Notice that the nearby metal lines are not affected by the ablation of metal only microns away. It is important that this process is compatible with the vacuum conditions in a SEM because other types of microscopes would not have the resolution to be able to distinguish these lines or to observe that the sparks completely cut the lines. Clearly microspark erosion is a cruder method than what can be achieved with a focused ion beam which is often used for failure analysis. However, the simpler method is sufficient in many cases and requires significantly less expensive equipment. The sparking was done using low voltages ( $< 10\text{ V}$ ) and low currents ( $< 10\text{ mA}$ ).

The spark occurs quickly and the surrounding material does not heat up significantly. The evolution of the temperature profile after a spark can be approximated by the solution to the heat equation for a two dimensional thermal conductor when a delta-function thermal pulse is applied,

$$T(\vec{r}, t) = \frac{1}{4\pi at} e^{-\frac{r^2}{4at}} \quad \text{with} \quad (7.3)$$

$$a = \frac{\sigma}{\rho\kappa_s}. \quad (7.4)$$

Here  $\rho$  is the mass density,  $\kappa_s$  is the specific heat capacity, and  $\sigma$  is the thermal conductivity. The temperature decreases exponentially with the distance  $r$  from the

point where the spark occurs. This means that a few decay lengths from the center of the spark the metal will be cool. The observed size of the holes generated in thin metal films is about a micron. Plugging this into the expression for the decay length gives an estimate for the length of time it takes to create the hole. This time  $\tau = \frac{r^2}{4\alpha}$  is approximately  $\tau \approx 1$  ns.<sup>1</sup>

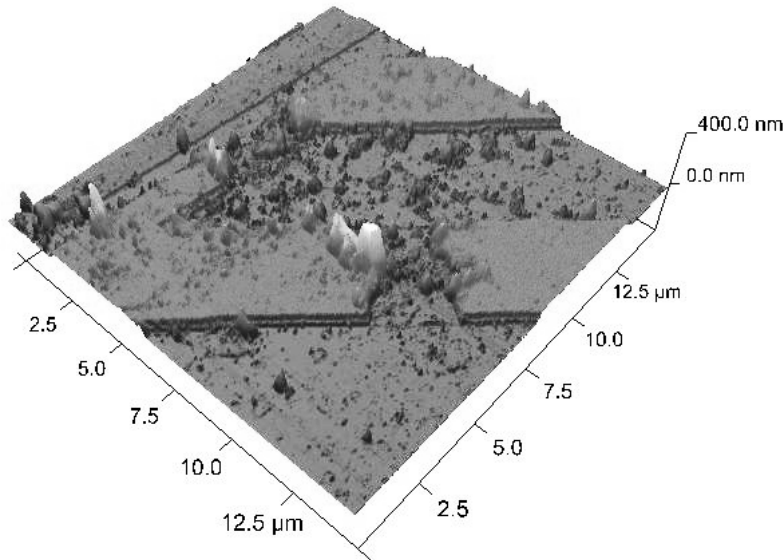


Figure 7.4.: An AFM image of the same region as in Figure 7.3. The Al lines are clearly cut with CBME, but ablated material lies around in the vicinity.

Metals are ablated while the underlying insulators are left unaffected. The ablation is therefore material selective. An atomic force microscopy (AFM) image of the circuit in Figure 7.4 shows that the SiO<sub>2</sub> substrate is smooth in the regions where metal has been removed by microspark erosion.

## 7.2. Electrical Fusing of Metal Wires and Thin Films

### 7.2.1. Electrical Fusing of a Photolithography Mask

We attempted to remove parts of a thin chrome film on a conventional photolithography mask using CBME but found it was not possible. Preliminary measurements were done under an optical microscope in air using a tungsten needle to make contact to the chrome film. When a few volts were applied to the needle, bubbles appeared around the point of contact indicating that an electrochemical process was taking place. Presumably a thin

<sup>1</sup>In the case of aluminum the decay time calculates for  $r = 1$   $\mu\text{m}$  to  $\tau = 2.6$  ns. The material parameters  $\kappa_s = 904 \frac{\text{J}}{\text{kg} \cdot \text{K}}$ ,  $\sigma = 235 \frac{\text{W}}{\text{m} \cdot \text{K}}$  and  $\rho = 2.7 \frac{\text{g}}{\text{cm}^3}$  are taken from <http://de.wikipedia.org/wiki/Aluminium> (19.5.2010).

film of water was absorbed on the surface of the film when it was exposed to air. The contact resistance was unstable due to the reaction. We repeated this experiment in vacuum ( $p \approx 10^{-6}$  mbar) and could not observe any bubbles although with this pressure some water would still be expected to be found at the surface and we can not exclude that some reaction was taking place. We attempted to perform CBME by putting the needle in contact with the chrome film and applying a voltage to establish a current. The film fused due to the high current density before the conditions for microspark erosion could be established. It was not necessary to retract the needle in this case. As the needle was slid along the film, a 5  $\mu\text{m}$  wide channel was cut in the chrome film (see Figure 7.5). The edges of this region are discolored. This is similar to the discoloration that was observed in these films when a high current density passes through them.

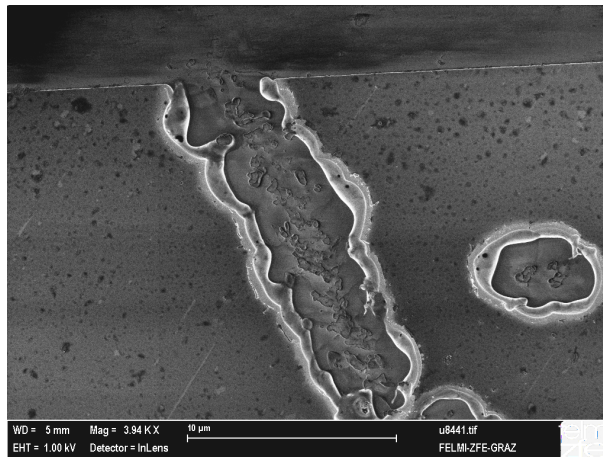


Figure 7.5.: SE image of a line cut in a conventional photolithography mask. The scale bar is 10  $\mu\text{m}$ .

### 7.2.2. Electrical Fusing of a Metal Wire

A fusing experiment was also performed on copper test structures, which was provided by Infineon (Regensburg) under a collaboration with FELMI (TU Graz). We were asked to conduct resistance measurements and determine the current, at which a copper line would fuse. The copper lines and contact pads were produced by lift-off processing and then buried under an isolating passivation layer. In order to conduct the resistance measurement, the isolating top layer had to be penetrated first. With extra stiff tungsten tips, the top layer could be pierced by scratching back and forth with the tip. In such a way, four tips were landed on individual contact pads. The contact resistance between the tips and the contact pads were measured to be of the order of a few ohms. The resistance of a nominally 500 nm wide and 1  $\mu\text{m}$  long copper line was determined by a four-point measurement to  $R_{Cu} = (519 \pm 1) \Omega$ . (see Figure 7.6a). To test the electrical stability of the copper line, the current was increased till the line fused. The

### 7.3. Conclusion

last measured current before fusing the wire was 18.4 mA at 11.5 V. At 20.4 mA the line was already fused and the voltage of the Sourcemeter was in compliance (100 V). The SE image in Figure 7.6b shows two contact pads and part of the fused copper line. Interestingly, the copper wire was not only damaged in the region of 500 nm line width, but also at the much larger contact pads. On the left tip, one can see well the swarf of the scratching procedure.

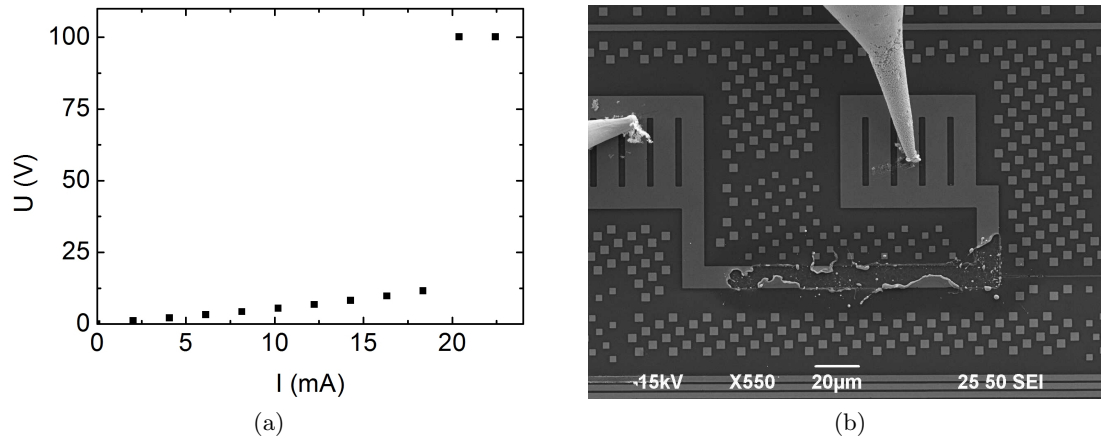


Figure 7.6.: (a) Current-voltage plot of a 500 nm wide and 1  $\mu\text{m}$  long copper line. The resistance was determined by the four-point measurement to  $R_{Cu} = (519 \pm 1) \Omega$ . In order to make electrical contact to the contact pads, an isolating passivation layer had to be punctured first. To test the electrical stability of the copper line, the current was increased till the line fused. The last data point before fusing the wire was 18.4 mA at 11.5 V. At 20.4 mA the line was already fused and the voltage of the Sourcemeter was in compliance (100 V). (b) The SE image shows two contact pads and part of the fused copper line. Interestingly, the copper wire was not only damaged in the region of 500 nm line width, but also at the much larger contact pads. On the left tip, one can see well the swarf of the scratching procedure.

### 7.3. Conclusion

We have shown that micromanipulators that are put into a SEM to perform electrical measurements can also be used to selectively remove metal films from integrated circuits and photolithography masks by CBME or electrical fusing. This can be useful in failure analysis or mask repair and is much cheaper than the conventional method of using a FIB.

The removal of metals by CBME works best with thin metal films where the metal is removed all the way to the substrate by a single spark. Thicker films conduct the heat away more efficiently and less material is removed per spark. Because more sparks

are necessary for thicker films and more material has to be removed, there is more redeposited metal around the cutting site. This results in less control of the final shape of the cut region.

Electrical fusing can also be used to cut metal lines and surfaces. If the current carrying tips are placed close together, the fuse region can be confined. With our probe station we could penetrate an isolating passivation layer and contact a buried copper structure. Four-point measurements were performed and the resistance could be evaluated. To test the electrical stability of the copper structure, we increased the current till the wire fused. Interestingly, the damage was not confined to a small area but rather extended over most part of the 500 nm wide line and a good part of the 10  $\mu\text{m}$  wide contact pad metallization. Additionally, we showed the possibility of cutting and structuring a photolithography mask by an electrical fusing process.

## 8. Voltage Contrast Imaging and Electron Beam-Induced Current

In the previous chapters, the scanning electron microscope (SEM) has been used mainly as an observational tool in the measurements. The interactions of the electron beam with the sample can also be exploited in electrical measurements. Measuring the spatially resolved electron beam induced current (EBIC) in semiconductors, useful information of semiconducting materials and semiconductor devices, i.e. p-n junctions, Schottky contacts and solar cells, can be obtained. Changing the work function of a surface by applying a voltage to a conducting part of a sample, the voltage contrast in the secondary electron (SE) image differentiates between surfaces of different potential.

### 8.1. Voltage Contrast Imaging

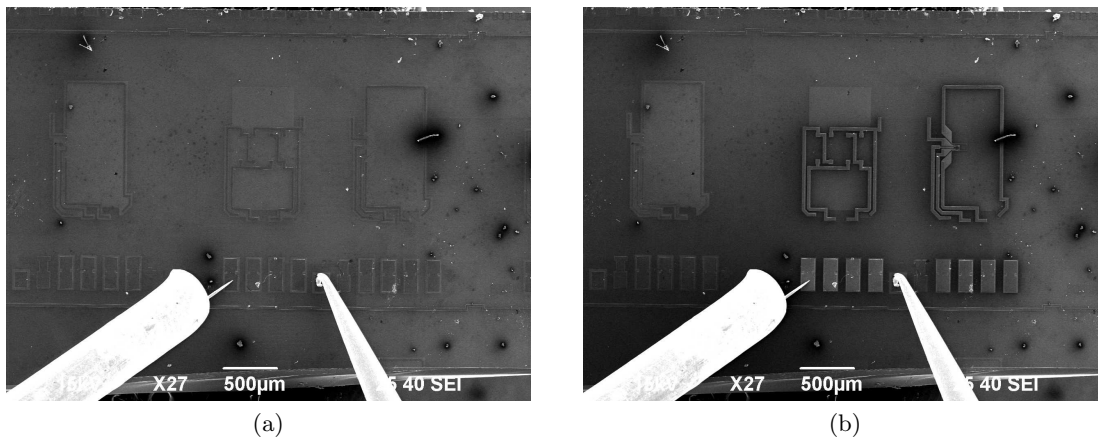


Figure 8.1.: SE image of an integrated circuit (a) without applied bias and (b) with an applied bias voltage of a few volt between two probe tips, which are landed on two contact pads.

Voltage contrast imaging in a SEM is a technique for studying potentials and potential distributions on a sample. Changes of the electric potential of a sample or a smaller part of it influences the potential distribution between the object and the collector of the SE detector and therefore the trajectories of the SEs. Applying a positive voltage to a region leads to less emitted SEs. Reversing the bias will increase the emitted electrons and leads to a brighter image. Thus a change of potential is reflected directly

in the SE signal. Regions of the same potential (conducting objects, i.e. wires) will have no potential contrast, whereas potential drops or regions of different potential can be visualized. This can be used for inspection purposes in integrated circuits. Broken wires and p-n junctions can be directly seen in the SE image.

Figure 8.1 shows two SE images of an integrated circuit without (Figure 8.1a) and with an applied voltage (Figure 8.1b) between tips, which are landed on two contact pads. The voltage contrast shows electrically connected regions of the IC structure.

### 8.1.1. Voltage Contrast Imaging of P-N Junctions

Here, we used the voltage contrast for visualizing a p-n junction across a cleaved surface of a doped silicon die. We placed two tungsten tips on each side of the p-n junction and applied a voltage of 10 V across the sample (see Figure 8.2). The positive biased side on the right appears darker in the SE image. The polarity is important, because the voltage drop across the p-n junction occurs only in reverse bias. Reversing the polarity results in the disappearance of the voltage contrast.

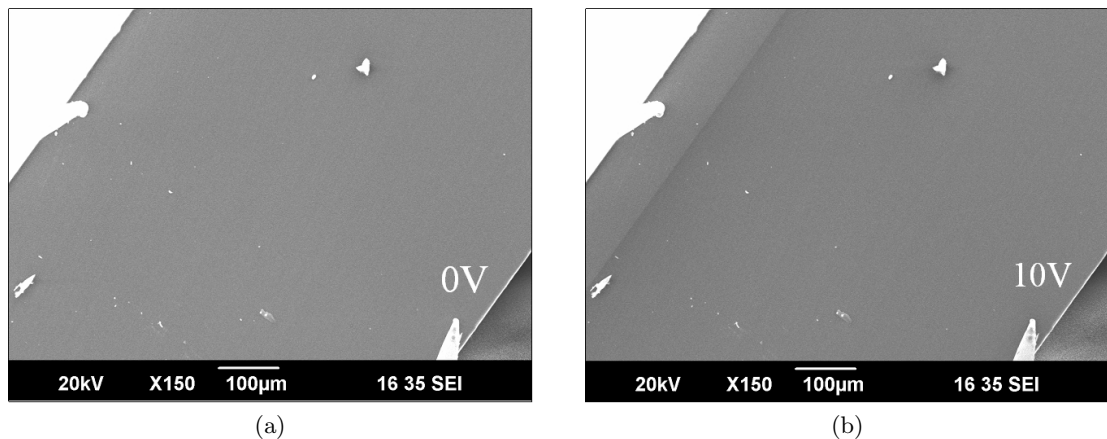


Figure 8.2.: (a) SE image of a cleaved surface of a doped silicon die with two tungsten tips landed near the edges. (b) Applying a voltage of 10 V between the tips reveals a p-n junction in the silicon at a distance of 100  $\mu\text{m}$  from the left edge.

### 8.1.2. Voltage Contrast Imaging of Single-Walled Carbon Nanotubes

Voltage Contrast was also used to enhance the visualization of single-walled carbon nanotubes (SWCNTs) [43]. The potential drop along a SWCNT was measured (see section 6.3). By applying a bias voltage of 15 V the visibility of the SWCNT could be considerably improved and easily recognized, despite their small diameter of around 2 nm. The positive bias enhances the emission of secondary electrons and the nanotube

appears bright in the SE image. Additionally, broken tubes are easily detected (see Figure 8.3).

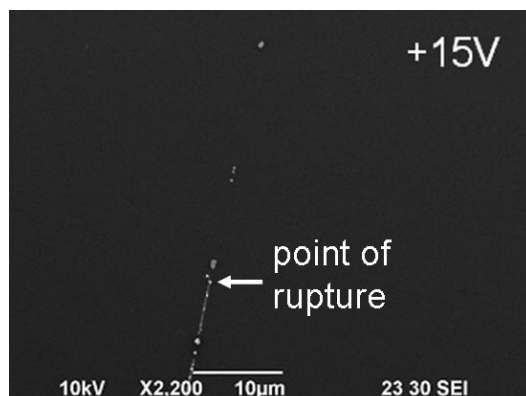


Figure 8.3.: SE image of a SWCNT (scale bar: 10  $\mu\text{m}$ ). The lower end is connected to a gold contact, which is biased at +15 V. Gold particles, that are attached to the nanotube, are visible across the image. The good visibility of the nanotube ends abruptly in the lower half of the image. The voltage contrast shows that the nanotube is broken and the point of rupture can be identified.

## 8.2. Electron Beam-Induced Current

Exposing the sample to the high energy beam of a SEM leads to numerous elastic and inelastic scattering events of the incoming electrons with the sample inside the so-called interaction volume (see chapter 2). In semiconductors, one primary electron generates numerous electron-hole pairs via ionization processes. In the presence of an internal electric field, such as a p-n junction or a Schottky barrier, or an externally applied electric field the charge carriers are separated and the resulting current can be measured. This technique provides the means to quantitatively determine physical properties like the diffusion length, the recombination time, the width of a junction or its depth below the surface [33, chap. 4.7]. In such a way optoelectronic devices like solar cells can be analyzed by excitation via the electron beam instead of a light source.

### 8.2.1. EBIC Measurements on P-N Junctions

Two tungsten tips were placed on each side of p-n junction, which was identified by voltage contrast imaging (see section 8.1.1) and the EBIC current flowing through both tips was measured by two SR570 current preamplifiers (current sink into a virtual ground). The electron beam of the SEM was scanned at an energy of 30 kV along a line, crossing the p-n junction perpendicularly. The duration of the line scan was 80 s.

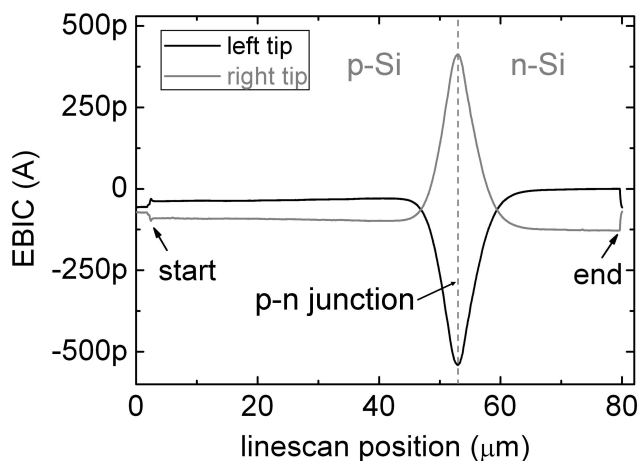


Figure 8.4.: Plot of the measured electron beam-induced current in dependence of the position of the electron beam during a line scan across a p-n junction. Two tips were placed on each side of the p-n junction and the currents flowing through both tips were measured by two SR570 current preamplifiers (current sink into a virtual ground). The charge carrier diffusion length can be estimated to 2.5  $\mu\text{m}$ .

With the magnification set to 1600, the line scan speed was 1  $\mu\text{m}/\text{s}$ . The measured currents are plotted in Figure 8.4. Close to the p-n junction, the current through the right tip (gray line) increases to a maximum value of 529 pA directly at the p-n junction (forward biased polarity). The full width at half maximum (FWHM) value of the Lorentzian shape is measured to 5.5  $\mu\text{m}$ . The current through the left tip is of the same magnitude but of different polarity. In terms of charge carriers, electrons flow from the p-n junction to the p-side (left), holes to the n-side (right).

The charge carrier diffusion length can be estimated to be on the order of half the FWHM value of the EBIC peak, which amounts to approximately 2.5  $\mu\text{m}$ . Considering the rather large diameter of the interaction volume of 5  $\mu\text{m}$  in silicon at a primary energy of 30 kV, which was determined by a Monte Carlo simulation (CASINO 2.42 [10]), the charge carrier diffusion length can even be smaller. This value is much shorter than measured elsewhere on the sample and can be attributed to the high concentration of crystal defects in the vicinity of the p-n junction, which were created by proton bombardment of the silicon surface during the p-doping process (see section 8.2.2).

### 8.2.2. EBIC Measurements on Schottky Contacts

Similarly to EBIC measurements across p-n junctions, Schottky contacts will also generate EBIC currents, due to the built-in electric field in the semiconductor close to a Schottky barrier. A Schottky barrier is a potential barrier formed at a metal-semiconductor junction which has rectifying characteristics.

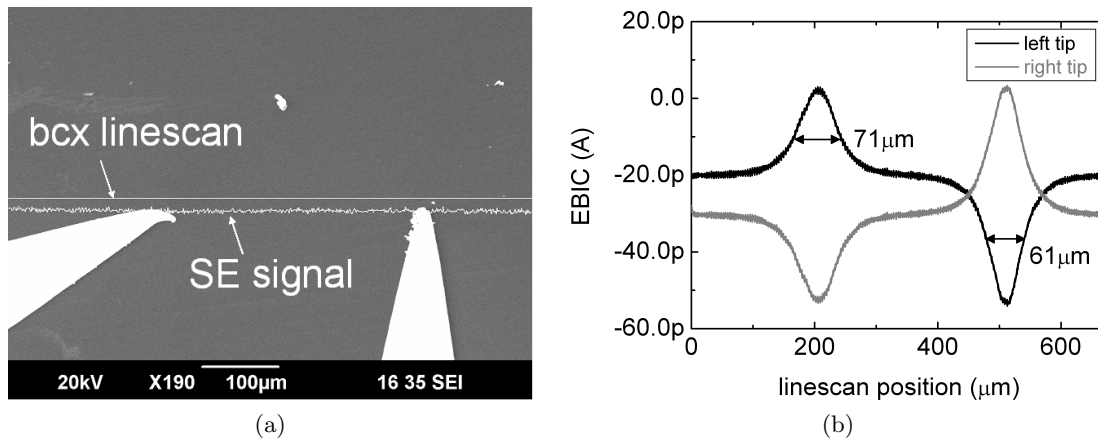


Figure 8.5.: (a) SE image of two grounded tungsten tips on an n-doped silicon substrate. During the EBIC measurement the electron beam was scanned along a line across this image passing the tips close by. The position of the line scan and the SE detector signal of the line scan are shown. (b) Graph of the EBIC signal of the two tips over the line scan position. The peaks in the measured current, which are situated at the nearest distance to the tip positions, are indications of Schottky barriers of the contacts. The FWHM values for the peaks of the left tip are 71  $\mu\text{m}$  and 61  $\mu\text{m}$  respectively.

Here, we landed two tungsten tips on a cleaved n-doped silicon surface and scanned the electron beam of the SEM along a line in close proximity ( $\leq 10 \mu\text{m}$ ) to the silicon-tip contacts as can be seen in Figure 8.5a. The currents through both tips were measured similarly as in section 8.2.1 and are plotted in dependence of the electron beam position in Figure 8.5b. The peaks in the measured current, which are situated at the nearest distance to the tip positions, are indications of Schottky barriers of the contacts. The difference in peak shape can be explained by the differing contact geometry and area. The FWHM values for the peaks of the left tip are 71  $\mu\text{m}$  and 61  $\mu\text{m}$  respectively and give an estimation of the charge carrier diffusion length, which can be approximated to 30–35  $\mu\text{m}$ . Note the more than tenfold higher charge carrier diffusion length compared to the results from the p-n junction of section 8.2.1, which is due to much less defects in this region.

### 8.2.3. EBIC Measurements on Silicon Solar Cells

The EBIC technique can also be used to measure the short-circuit current of solar cells by shining electrons instead of light on the photovoltaic device. The electron beam of a SEM was set to spot mode and the programmable sample stage was used to move a piece of a polycrystalline silicon solar cell (see Figure 8.6a) under the stationary beam. The p- and n-side metal contacts of the solar cell were each contacted by a tungsten tip and the current through the tips was measured by two SR570 current preamplifiers as above. A

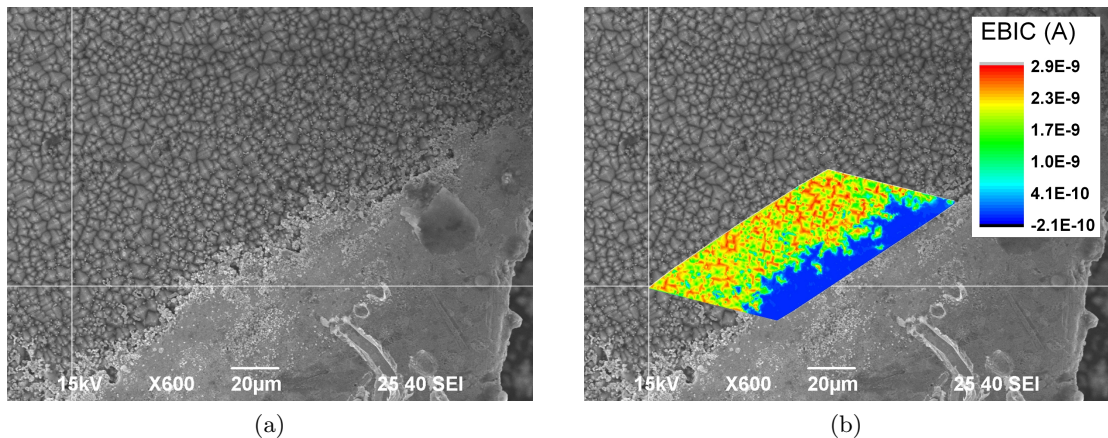


Figure 8.6.: (a) A piece of a polycrystalline silicon solar cell inside a SEM (SE image). (b) Overlay of a 2D microscale EBIC map with the SE image of the solar cell. The topographic pattern is repeated in the 2D EBIC map.

two dimensional microscale map ( $100 \times 100$  points) of the generated EBIC current was produced (see Figure 8.6b). The measured current on the active zone varied between 1 and 3 nA. Comparing the topographic SE image and the EBIC map, the micron sized structures are in striking agreement. The EBIC map shows no signal, when the electron beam hits the top metallization contact.

These preliminary results of EBIC measurements on solar cells were the starting point for extensive studies on solution-processed solar cells, which are presented in the next chapter.

### 8.3. Conclusion

Probing inside a SEM is not only beneficial for reaching high image resolutions, but opens up several possibilities of employing the SEM as an active part of the experiment. Two main examples, namely voltage contrast and EBIC, were discussed and several applications were presented.

Voltage contrast was used to inspect an integrated circuit, where electrically connected parts can be distinguished from the rest of the circuit. The potential drop across a p-n junction in reverse bias was observed. Voltage contrast imaging was also used to enhance the visibility of SWCNTs and to detect broken tubes and the point of rupture.

The silicon p-n junction was also used as a test case for the EBIC measurement technique. By scanning the electron beam across the p-n junction and recording the generated EBIC current, the charge carrier diffusion length could be extracted. Similarly, the charge carrier diffusion length in the n-doped region of the cleaved silicon sample was determined, by producing Schottky contacts at the interface of the semicon-

ductor surface with tungsten tips and scanning the electron beam across the contact region. It was found, that the diffusion length was more than ten times larger at the Schottky contacts than at the p-n junction. This is attributed to the high concentration of crystal defects, due to the proton bombardment during the p-doping process. By exposing a polycrystalline silicon solar cell to the electron beam, a 2D map of the EBIC current was generated.



## 9. 2D Mapping of the Electron Beam Induced Current in Solution Processed Solar Cells

Electron beam induced current (EBIC) measurements were used to produce 2D microscale maps for investigating the homogeneity of solar cells. These maps are acquired by setting the electron beam of a scanning electron microscope (SEM) to high magnification and using a programmable sample stage to move the solar cell under the quasi stationary beam. The electron beam generates electron-hole pairs in the solar cell much like light does in normal solar cell operation. Solution processed solar cells consisting of purely inorganic and purely organic materials were measured. Since the electron beam damages organic material, it was important to ensure that the measurements were made before the materials were altered.

The development of solution processed solar cells is being pursued in many laboratories since it is potentially an inexpensive route to provide clean energy. To optimize these solar cells, it is important to characterize their uniformity. A convenient method for characterizing the performance of solar cells is EBIC [5]. In this technique, the electron beam of a SEM falls on a solar cell and generates electron-hole pairs. Charge separation occurs and a current flows just as it does when light falls on the solar cell. EBIC images are essentially maps of the short circuit current collected by the junction after carriers have been excited by the electron beam. The method is most often used to probe cleaved solar cells in the cross-section geometry in order to reveal the junction position [16]. Here, the solar cells are scanned laterally by irradiating the active material through the back electrode.

The EBIC current is typically much larger than the beam current since the electrons in the beam have a high energy and each produce many electron-hole pairs. EBIC can image large areas and has a resolution limited by the size of the interaction volume of the electron beam. While EBIC has been used to characterize inorganic thin film solar cells [16], it is not commonly used to investigate organic solar cells.

### 9.1. Working Principle of Solar Cells

Inorganic solar cells, with silicon solar cells being the most prominent representatives, are very well known and understood (i.e. [3]). In the semiconducting material charge carriers are excited from the valence band into the conduction band by light absorption. At the p-n junction the internal electric field induced by the charge carrier diffusion generates the opposite directional drift current, which is the dominant force in these

devices for charge carrier separation. Are the p- and n-side connected to ohmic metal-semiconductor contacts, an external load can be powered by the solar cell device.

The optoelectronic processes in organic solar cells are different than in their inorganic counterparts. Here, the p-n junction is replaced by a donor/acceptor interface in the photoactive layer. The excitons (bound electron-hole pairs) are dissociated in current polymer solar cells by a gradient of the potential across the donor/acceptor interface. In organic materials the exciton diffusion length is only 5–20 nm [23]. Blending the acceptor and donor materials increases the interface area and eliminates the effect of a diffusion limited charge separation. The separated charges have then to be transported to the respective electrodes by percolated paths. Thus, the bulk heterojunction has to consist of interpenetrating networks of donor and acceptor phases. The driving force for the charge carrier extraction is the internal electric field caused by the different work function electrodes.

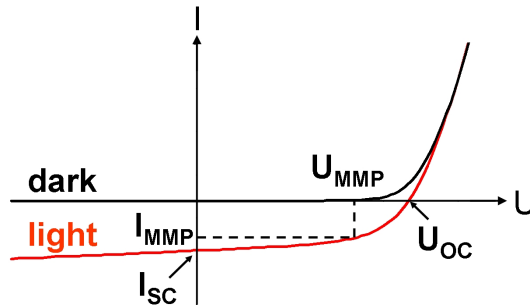


Figure 9.1.: A typical current-voltage characteristic of a solar cell with (red line) and without (black line) illumination. The product of  $I_{MPP}$  and  $V_{MPP}$  is the maximum power point. The ratio between the maximum power  $V_{MPP} \cdot I_{MPP}$  and the product of the open circuit voltage and the short circuit current  $V_{OC} \cdot I_{SC}$  is the filling factor (FF).

A typical current-voltage characteristic of a polymer solar cell under illumination is shown in Figure 9.1. The maximum power point (MPP) corresponds to the maximum of the product of photocurrent and voltage. The ratio between the maximum power  $V_{MPP} \cdot I_{MPP}$  and the product of the open circuit voltage and the short circuit current  $V_{OC} \cdot I_{SC}$  is called the fill factor (FF). The power conversion efficiency  $\eta$  is defined as the maximum power output divided by the incident light power:

$$\eta_{POWER} = \frac{P_{OUT}}{P_{IN}} = \frac{I_{MPP} \cdot V_{MPP}}{P_{IN}} = \frac{FF \cdot I_{SC} \cdot V_{OC}}{P_{IN}}. \quad (9.1)$$

Improving the efficiency of solar cells is of course one major goal for research and development of these devices. Commonly, the efficiency is determined by illuminating the solar cell with a standardized light source and measuring the current-voltage characteristics. This measurement is an average over the whole device and no substructure can be evaluated. A timeline of the development of solar cell energy conversion efficien-

## 9.1. Working Principle of Solar Cells

ciencies for various solar cell technologies in research is shown in Figure 9.2 as reported by Lawrence Kazmerski, National Renewable Energy Laboratory (USA).<sup>1</sup>

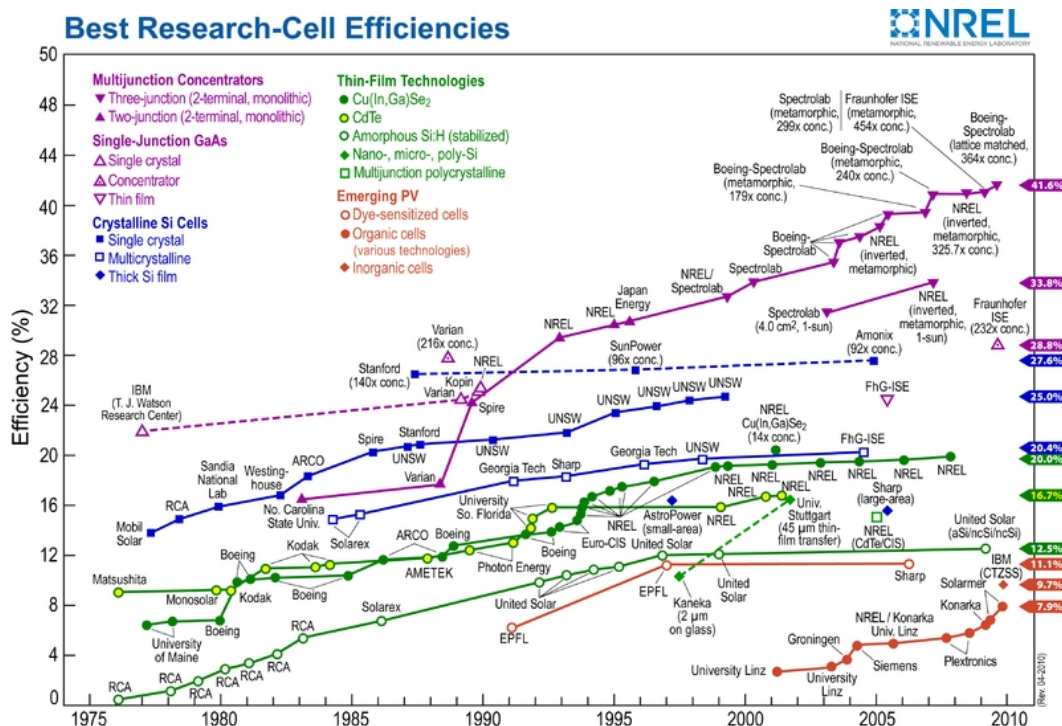


Figure 9.2.: Reported timeline of solar cell energy conversion efficiencies for various solar cell technologies (from National Renewable Energy Laboratory).

The micro- and nanoscale morphology of the photoactive layer plays an essential role in the optoelectronic properties (charge separation and transport), as was mentioned earlier. Several techniques such as high resolution spectroscopic mapping [42], near-field scanning photocurrent measurements [30] and photoconductive atomic force microscopy [20] have been already successfully applied to analyze correlations between the nanoscale morphology and the generated photocurrent in organic solar cell devices.

We employed EBIC measurements to probe the locally, by the electron beam generated current on the micrometer scale. Although the charge carrier generation process is different as by excitation with light, the processes of charge separation and transport are the same. Therefore, this method should be equivalent to light induced photocurrent measurements for examining the homogeneity of the solar cell devices. With a lateral resolution of one up to tens of micrometers, problems in the fabrication of the solar cells can be detected.

<sup>1</sup>source: <http://en.wikipedia.org/wiki/File:PVeff%28rev100414%29.png> (11.6.2010)

## 9.2. Fabrication

The fabrication of the two types of solution processed solar cells are described below. Further details on the used materials (source and specifications) can be found in appendix B.

### 9.2.1. P3HT:PCBM Solar Cells

Organic solar cells consisting of a blend of poly(3-hexylthiophene) (P3HT) and [6,6]-phenyl-C61-butyric acid methyl ester (PCBM) were fabricated on a glass substrate using a layer sequence of indium tin oxide (ITO) (100 nm), Poly(3,4-ethylenedioxythiophene) poly(styrenesulfonate) (PEDOT:PSS) (30 nm), P3HT:PCBM (100–150 nm), and aluminum (80–120 nm).<sup>2</sup> The structural formulas of P3HT and PCBM are shown in Figure 9.3.

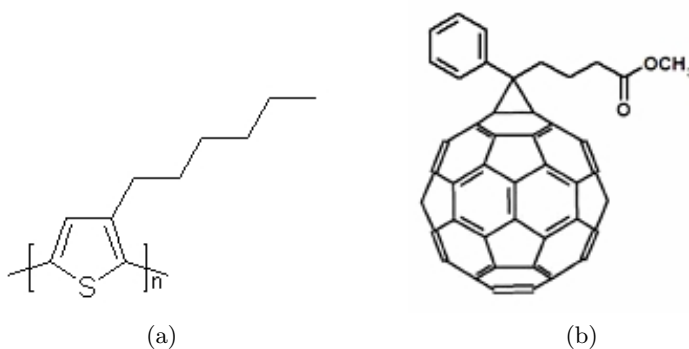


Figure 9.3.: Structural formulas of (a) poly(3-hexylthiophene) (P3HT) and (b) phenyl-C61-butyric acid methyl ester (PCBM).

Indium tin oxide coated glass substrates were cleaned in an ultrasonic water bath followed by an ultrasonic isopropanol bath. Indium tin oxide acts as a transparent electrode. For contact improvement and enhanced hole transportation, the indium tin oxide (ITO) was coated with a thin layer of PEDOT:PSS and annealed at 80 °C for 15 min. The photoactive layer was spin cast from a solution of a P3HT:PCBM blend (1:0.8 w/w) in chloroform with film thicknesses of 100–150 nm. The aluminum electrode was deposited on the polymer-fullerene blend by vacuum deposition at  $10^{-6}$  mbar. Film thicknesses ranged from 80–120 nm. The photoactive area was 0.09 cm<sup>2</sup>. For tuning the P3HT:PCBM blend morphology, the devices were annealed at temperatures ranging from 100–200 °C for 15 min after the deposition of the aluminum film.

<sup>2</sup>The P3HT:PCBM solar cells were fabricated by Thomas Rath (Institute for Chemistry and Technology of Organic Materials (ICTM) and Christian Doppler Laboratory for Nanocomposite Solar Cells, TU Graz).

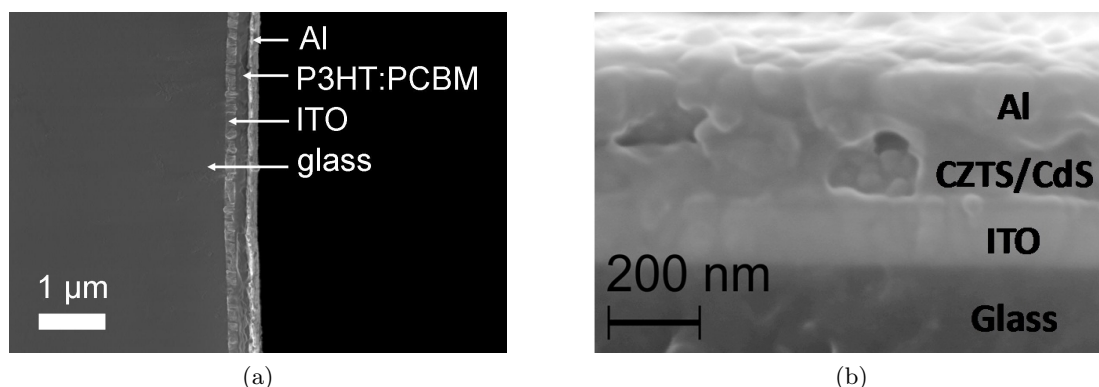


Figure 9.4.: SE images of cross-sections of an (a) P3HT:PCBM solar cell and (b) CdS/CZTS solar cell.

Figure 9.4a shows a secondary electron (SE) image of a cross-section of a P3HT:PCBM solar cell device.<sup>3</sup>

For the EBIC measurements, the solar cell aluminum and ITO electrodes were contacted by thin copper wires, that were glued to the electrodes by conductive epoxy. The ITO was partially removed by etching to prevent electric shorting between the ITO and the aluminum contact pad.

### 9.2.2. CdS/CZTS Solar Cells

The CdS/CZTS solar cells were also fabricated on glass substrates using a layer sequence of ITO (100 nm), CdS/CZTS (120–130 nm), and aluminum (200 nm).<sup>4</sup>

Indium tin oxide coated glass substrates were cleaned in an ultrasonic water bath followed by an ultrasonic isopropanol bath, each for 20 min. The  $\text{Cu}_2\text{ZnSnS}_4$  (CZTS) precursor solution consisted of  $\text{CuI}$  (0.32 mol/l),  $\text{Zn}(\text{acetate})_2$  (0.16 mol/l),  $\text{SnCl}_2$  (0.16 mol/l) and TAA (3.2 mol/l or 2.2 mol/l) dissolved in pyridine. The solution was then spin coated at a speed of 1500 rpm on the substrates for 18 s, which were then baked for 15 min at 350 °C (heating rate 21 °C/min) under vacuum to form the CZTS layer. After the heat treatment the samples were cooled down to room temperature under vacuum within 10 min. The CdS buffer layer was prepared from a pyridine solution containing  $\text{Cd}(\text{acetate})_2$  (0.33 mol/l) and thiourea (0.99 mol/l), which was spin coated directly onto the CZTS layer at 1000 rpm for 60 s. Then the device was annealed at 250 °C for 10 min under vacuum before a second CdS layer was deposited on top using the same conditions, except the heat treatment which was changed to 250 °C for 5 min. The aluminum top electrode was deposited at a pressure of  $10^{-6}$  mbar with a thickness

<sup>3</sup>The cross-section image of the P3HT:PCBM solar cell was made by Johannes Rattenberger (FELMI, TU Graz).

<sup>4</sup>The CdS/CZTS solar cells were fabricated by Achim Fischereder (Institute for Chemistry and Technology of Organic Materials (ICTM) and Christian Doppler Laboratory for Nanocomposite Solar Cells, TU Graz).

of 200 nm to complete device fabrication. Due to similar Z-values and similar morphologies for CZTS and CdS it was not possible to distinguish between these two layers in the SE image of a cross-section (see Figure 9.4b).<sup>5</sup> Therefore only the thickness of the combined layers of CZTS and CdS can be estimated to be 120–130 nm.

### 9.3. The EBIC Measurement Technique for Solution Processed Solar Cells

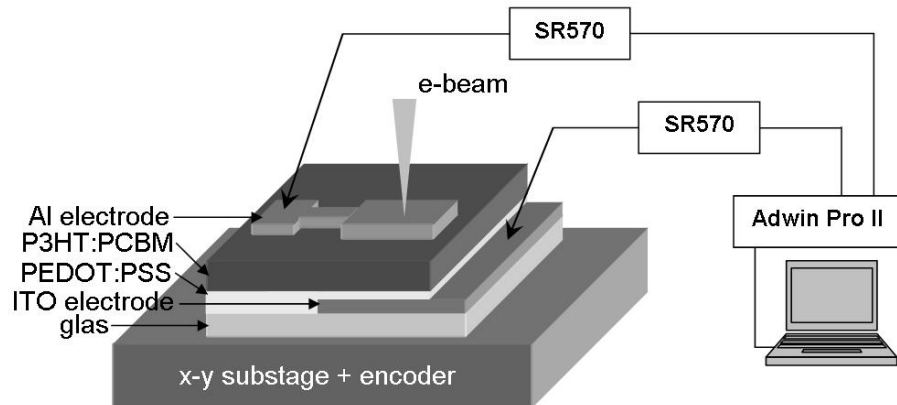


Figure 9.5.: Schematics of the experimental setup of the EBIC measurements and device architecture of the examined organic solar cells. Copper wires were glued with conductive epoxy to the aluminum and ITO electrode, respectively.

The electron beam of the SEM was either set in spot mode or exposed a larger scan window and solar cells were scanned under the beam using a programmable sample stage. While scanning, the currents flowing through the two contacts of the solar cell were measured using two separate current amplifiers (*SR570*). When the electron beam fell on an active area of the solar cell, the current amplifiers measured currents of opposite sign but equal magnitude. This is the EBIC current that results from the separation of electrons and holes generated by the electron beam. When the electron beam did not fall on an active area of a solar cell, the current amplifiers measured a small specimen current which was on the order of the beam current [11]. The specimen currents flowing through the two contacts of the solar cell typically have the same sign. In the following when we refer to an EBIC current it will always be a current much larger than the beam current where the current amplifiers measure currents of opposite sign but equal magnitude.

<sup>5</sup>The cross-section image of the CdS/CZTS solar cell was made by Wernfried Haas (Christian Doppler Laboratory for Nanocomposite Solar Cells and FELMI, TU Graz).

All current measurements for the 2D EBIC maps were taken with a sampling rate of 100 kHz for typically 100 ms duration. Because of the exponential decay of the EBIC signal due to beam damage, the current measurement duration and the scan window size were chosen such, that the measurement time was much shorter than the decay time constant. In that case the exponential decay of the current could be approximated by a linear fit and the initial value for the EBIC signal was calculated and stored together with the coordinates from the x-y substage encoders.<sup>6</sup> After finishing the current measurement, the substage traveled to the next position and the subsequent EBIC value was taken. A *LabVIEW* program controlled these procedures and communicated with the substage controller (via RS232) and with the *ADwin-Pro II* (via Ethernet). The *ADwin-Pro II* measured the analog output voltages of the current amplifiers (*SR570*) and performed the linear regression of the measured data (see Figure 9.5). All measurement programs were developed during this work.

## 9.4. EBIC Measurements on P3HT:PCBM Solar Cells

A well known representative of polymer-fullerene solar cells is a blend of P3HT and PCBM acting as the photoactive layer. Because of the intense studies performed on this material system with various techniques, we chose it for comparability of our findings with literature. Extensive investigations of the beam damage due to the EBIC measurement as well as analyzing the impact of different fabrication parameters and processes on the performance of the solar cells have been performed.

### 9.4.1. Beam Damage in P3HT:PCBM Solar Cells

A difficulty of using EBIC to measure organic solar cells is that the electron beam causes damage and it is necessary to ensure that a signal is measured before the beam induced damage alters the solar cell too much [35]. To reduce the damage, the solar cells were placed upside-down with the aluminum contact on top of the organic layer. For low acceleration voltages, the electron beam did not penetrate the aluminum layer. This could be directly observed by the fact, that there was no EBIC signal generated since no electron hole pairs were generated in the solar cell. A Monte Carlo simulation of the energy deposited by the electron beam for a low acceleration voltage of 2 kV was made with the program CASINO 2.42 [10] and is shown in Figure 9.6a.<sup>7</sup>

At this low acceleration voltage, the interaction volume remains in the aluminum contact. It is therefore possible to image the solar cells at low beam energy without causing any damage to the underlying layers.

As the acceleration voltage is increased, the electrons can penetrate the aluminum layer and an EBIC signal appears. At 5 kV the simulation in Figure 9.6b shows that the interaction volume reaches into the organic semiconductor layer with a lateral diameter

---

<sup>6</sup>The initial value of the EBIC current is  $I(t_0) = I_{offset} + I_0$ , see Eq. 9.2 in section 9.4.

<sup>7</sup>The simulations were calculated for 500 000 electrons and a beam radius of 10 nm. The sample stack consisted of aluminum (thickness: 100 nm, density: 2.7 g/cm<sup>3</sup>), P3HT:PCBM (150 nm, 1.1 g/cm<sup>3</sup>), PEDOT:PSS (30 nm, 0.87 g/cm<sup>3</sup>), ITO (100 nm, 7.12 g/cm<sup>3</sup>) and glass as substrate (1.74 g/cm<sup>3</sup>).

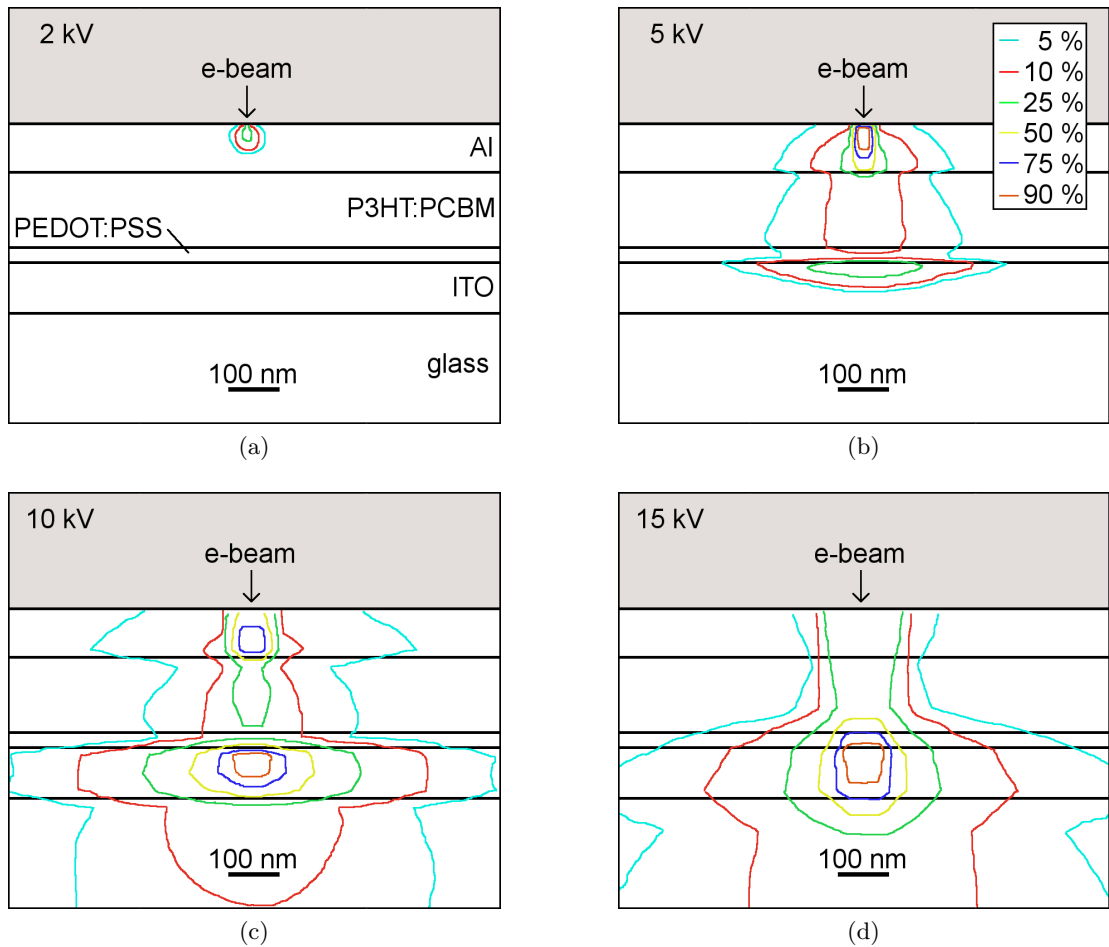


Figure 9.6.: Cross-section views of the absorbed energy in a P3HT:PCBM solar cell with acceleration voltages (a) 2 kV, (b) 5 kV, (c) 10 kV and (d) 15 kV were produced by Monte Carlo simulations (100 nm Al; 150 nm P3HT:PCBM; 30 nm PEDOT:PSS; 100 nm ITO; 500 000 electron trajectories simulated). The energy contour lines show the percentage of energy not contained within the line.

of about 400 nm, although most of the energy is deposited in the top metal layer. For even higher beam energies, the interaction volume grows both in diameter and depth (see Figure 9.6c and 9.6d). The percentage of the deposited energy in the active layer increases as well as the total amount of energy because of the increasing beam energy. For both minimal beam damage and high lateral resolution (which means a small interaction volume) high acceleration voltages should be avoided. Contrary, improving the signal to noise ratio of the EBIC requires increasing the beam energy. A compromise has to be found.

When the acceleration voltage is set large enough to penetrate the aluminum layer

and generate an EBIC signal, the magnitude of the measured signal decays due to damage caused by the electron beam. Figure 9.7a shows the timeseries of the EBIC decay for an acceleration voltage of 5 kV. The beam was scanned over an area of  $86 \mu\text{m}^2$  and the emission current was 9.95 pA. This decrease of the current in time can be fitted by an exponential decay of the form:

$$I_{EBIC}(t) = I_{offset} + I_0 \cdot \exp\left(\frac{t_0 - t}{\tau}\right). \quad (9.2)$$

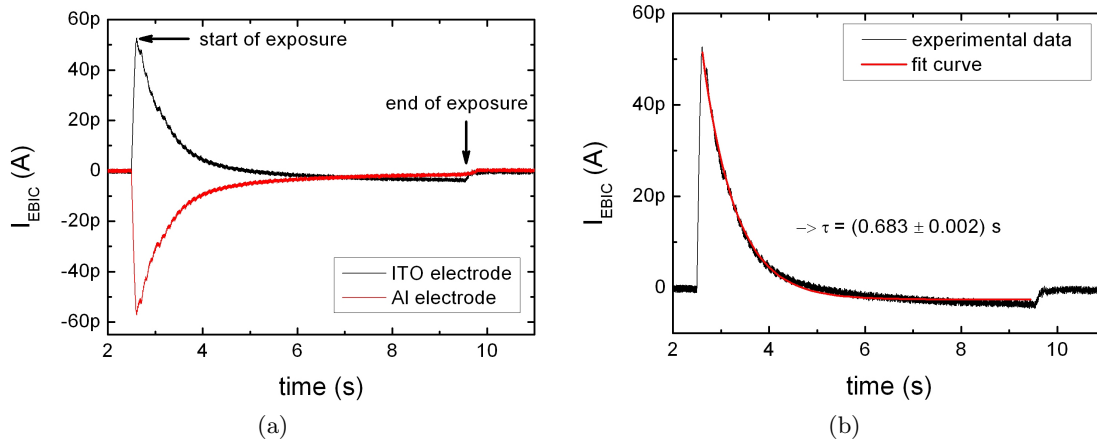


Figure 9.7.: (a) Timeseries of the EBIC currents of both electrodes when the electron beam was scanned over an area of  $86 \mu\text{m}^2$  of the organic solar cell. The currents are of opposite sign but equal magnitude. The probe current was measured to 9.95 pA. The damage caused by the beam causes a decrease in the EBIC current. (b) This decrease in current can be fitted by an exponential decay. The fitted decay time constant  $\tau = (0.683 \pm 0.002)$  is a quantitative measure for the radiation damage in the active organic material.

The measured current starts at  $t_0$  with the initial value  $I_{offset} + I_0$ , where the term  $I_{offset}$  contains the specimen current and an internal offset current of the current preamplifier. For simplicity, this term is kept constant. The decay time constant  $\tau$ , at which the current is decreased to  $1/e$  of the initial value, is used in the following to quantify the amount of the damage for a given acceleration voltage, scan area and emission current (Figure 9.7b). We have observed that the damage depends on the electron dose, measured in electrons/ $\text{cm}^2$ . For the three different acceleration voltages 5, 10 and 15 kV the fitted decay time constant increases with a linear trend for different scan area sizes (Figure 9.8a). The emission current was constant for each voltage, respectively. For better comparison the decay time constants were normalized for the emission current with respect to the measurement with  $U_{acc} = 15$  kV.

Increasing the electron dose by increasing the emission current (by changing the beam spot size) increases the damage also fairly linearly. This can be seen in Figure 9.8b where

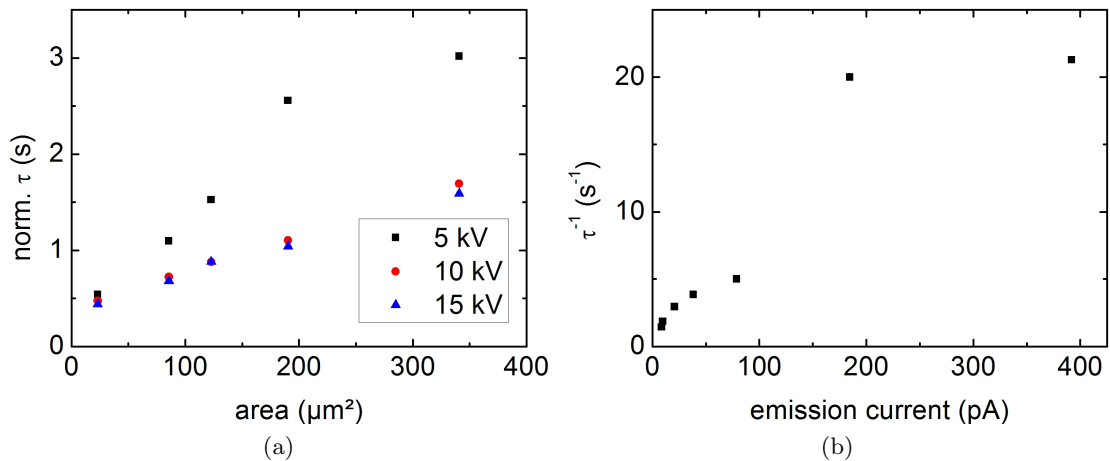


Figure 9.8.: (a) Radiation damage in dependence of the exposed area. The fitted decay time constants for different scan area sizes are plotted for three different acceleration voltages 5, 10 and 15 kV. For better comparison the decay time constants were normalized for the emission current with respect to  $U_{acc} = 15$  kV. (b) Radiation damage in dependence of the emission current. The inverse of the fitted decay time constants for different emission currents are plotted ( $U_{acc} = 5$  kV, area:  $86 \mu\text{m}^2$ ).

the inverse of the decay time is plotted in dependence of the emission current. The exposed area was set to  $86 \mu\text{m}^2$  and the acceleration voltage was 5 kV. Absolute values for the effective electron dose, which is responsible for the observed beam damage, are difficult to obtain, mainly because we only know the total number of electrons entering the sample which does not take into account the structure of our sample with its different material layers and their thicknesses.

For our typical EBIC imaging voltage of 5 kV, the total electron dose necessary to reduce the EBIC current by a factor of 2 was  $10 \mu\text{C}/\text{cm}^2$ . This dose is roughly 1000 times lower than what is used to expose a resist in electron beam lithography [15]. The simulation results (see Figure 9.6b) suggest an effective electron dose of only 10 % or less of the total electron dose. From the Bethe stopping power relation (Eq. 2.1 in chapter 2) a dependence of the acceleration voltage on the effective electron dose is also expected, as the mean primary energy loss per unit trajectory length  $dE/dx$  is a function of the primary electron energy  $E_0$  and residual energy  $E$ . The experimental data reflect this partly (see Figure 9.8a): Although the data points for the acceleration voltages 10 kV and 15 kV coincide more or less, the data for 5 kV indicate indeed a longer decay time compared to the higher electron energies, thus a lower effective electron dose.

The EBIC measurements require a certain time that should be much shorter than the time it takes to damage the sample substantially. For a fixed current, the time it takes to damage the sample can be reduced by increasing the area that is illuminated by the electron beam. In practice, this was the limiting factor that determined the spatial

resolution that could be achieved for the organic solar cells.

#### 9.4.2. 2D Mapping of Organic Solar Cells Using EBIC

In P3HT:PCBM solar cells, the beam damage in the active organic layer was limiting the spatial resolution of the EBIC measurements. The scan window of the electron beam was set to a specific magnification and scanned permanently over the sample from the start of the measurement to the end. In most cases, the electron beam was scanning over an area of  $86 \mu\text{m}^2$ .<sup>8</sup>

The measured EBIC signal of a P3HT:PCBM solar cell is displayed as a 2D color plot in Figure 9.9a. For clarity a line scan at position  $y = 1000 \mu\text{m}$  is shown in Figure 9.9b. Large variations of the EBIC signal across the device as well as an offset current (here  $I_{offset} \approx 50 \text{ pA}$ , see section 9.4.1), consisting mainly of the specimen current, can be seen. The color plot reflects the area of the aluminum electrode, shown in an SE image in Figure 9.9c. Excitons, which are created far away from the electrode, recombine instead of participating in the EBIC generation. Also inside the electrode area, regions of very poor current can be seen, ranging from fifty to several hundreds of micrometer in diameter. There is an approximately  $100 \mu\text{m}$  wide border of mediocre current at the edges and around the defects.

The defects could stem from holes at the various interfaces of the stacked layers, from big dust particles or phase separation of the organic blend. Different processing parameters were employed to investigate the cause of the defect generation. Besides the defects, where the EBIC signal is around zero, a variation of the signal with a typical length scale of 50 to  $100 \mu\text{m}$  is present. Wang et al. showed that the cluster sizes of PCBM in a P3HT matrix depend strongly on the annealing time for an annealing temperature of  $140 \text{ }^\circ\text{C}$  [42]. For an annealing time of 5 min the measured cluster sizes of the PCBM aggregates were in the nanometer range, whereas for 30 min the size increased into the micrometer range. The shorter annealing time showed additionally a strong quenching of the photoluminescence which indicates an intense photoinduced charge transfer process. These findings would imply a variation of the EBIC signal on the sub-micrometer scale and are not consistent with our measurement. This suggests a poor and unsatisfying morphology of the P3HT:PCBM blend or a different origin than the morphology.

#### 9.4.3. 2D Maps of EBIC at Different Beam Energies

A P3HT:PCBM solar cell (annealing temperature:  $150 \text{ }^\circ\text{C}$ ) was scanned with three different beam energies without overlap of the scans. In this way 2D EBIC maps of three quadrants of the device were generated (see Figure 9.10). The 5 and 10 kV maps in Figure 9.10b and 9.10d were scanned with a lateral resolution of  $15 \mu\text{m}$ , the 15 kV scan (Figure 9.10a) was scanned with a step size of  $30 \mu\text{m}$ . The scan window size of the electron beam was the same for all three scans ( $86 \mu\text{m}^2$ ).

---

<sup>8</sup>Scan mode "Scan 2" of the JSM-6490LV was used (frame rate: 0.15 s, pixel:  $640 \times 480$ ). At magnification 12000 the scan window is  $10.7 \mu\text{m} \times 8 \mu\text{m} = 85.6 \mu\text{m}^2$  in area size.

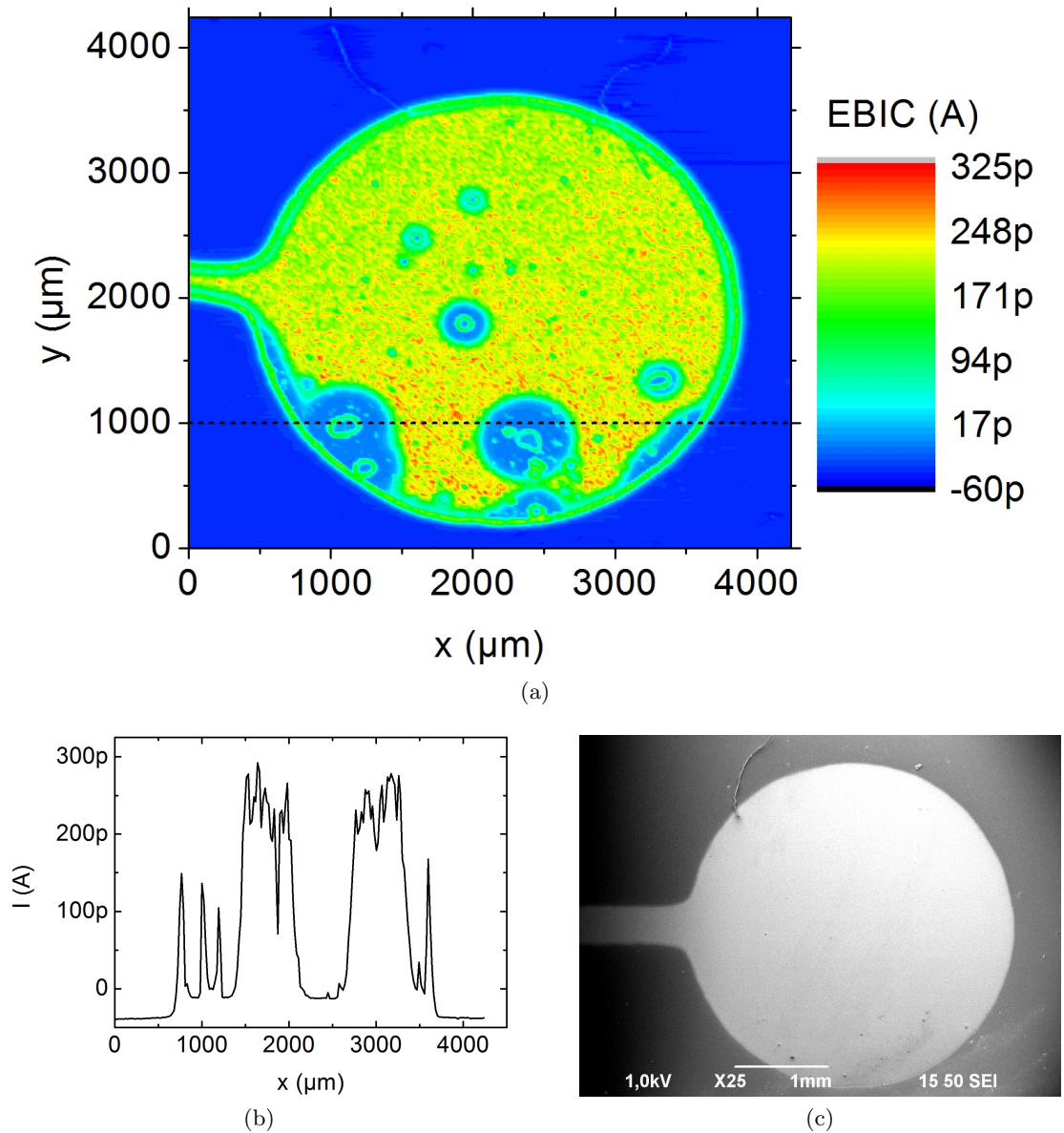


Figure 9.9.: (a) 2D color plot of the EBIC signal of a P3HT:PCBM solar cell at a beam energy of 5 kV. The device was annealed at 150 °C. The electron beam exposure area was 380  $\mu\text{m}^2$  and the step size 21  $\mu\text{m}$ . The dashed black line indicates the position of the line scan shown in (b). (c) SE image of the examined area.

The similarity of the occurring features in the 2D maps made at different beam energies are apparent. Again, large variations of the EBIC magnitude are observed. A 700  $\mu\text{m}$  border along the edge of the device with a higher current generation is present. Throughout the device, round defects with sizes up to 500  $\mu\text{m}$  with no EBIC signal are existent. In the SE image in Figure 9.9c only one structural round defect can be seen, indicated by the arrow. At the same position the EBIC map shows also a defect (see the arrows in Figure 9.10b and 9.10d).

From the comparison of 2D EBIC maps measured with different beam energies one can conclude, that the selection of the beam energy can be based mainly on beam damage considerations. That means, that for these devices a beam energy of 5 kV is a good choice. The beam damage is less than at higher energies (see Figure 9.8a), but the penetration depth of primary electrons is high enough to generate a good EBIC signal.

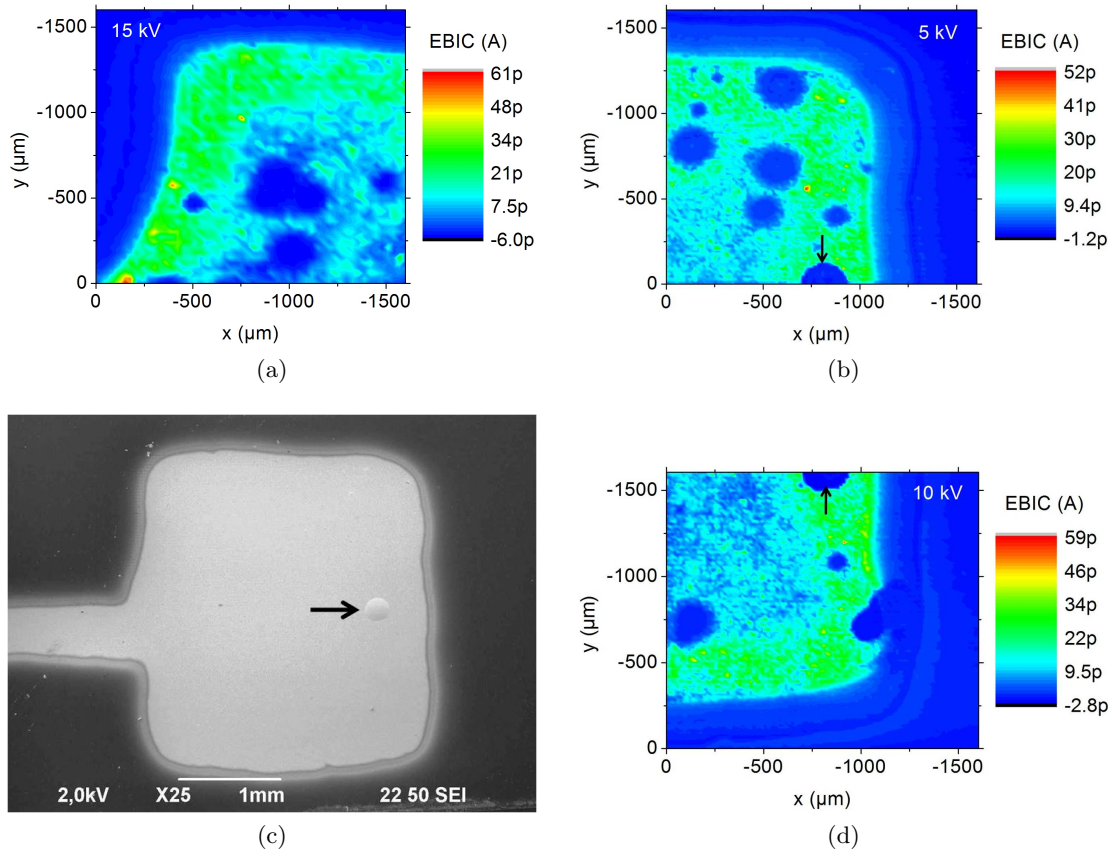


Figure 9.10.: 2D EBIC maps at different beam energies of the same P3HT:PCBM solar cell: (a) 15 kV at the upper left quadrant, (b) 5 kV at the upper right and (d) 10 kV at the lower right quadrant. The influence of the beam energy on the generated EBIC signal is negligible. (c) SE image of the investigated solar cell device. The bright area is the aluminum electrode. The arrows indicate the position, where a defect is discernible in the SE image as well as in the EBIC maps.

#### 9.4.4. Analysis of Different Annealing Temperatures

Using the EBIC technique a systematic study of the influence of different annealing temperatures in the fabrication of P3HT:PCBM solar cells on the performance of these devices has been performed. The annealing process was important for producing an optimal blend morphology. It was a postproduction treatment and took place after the deposition of the aluminum electrodes. Figure 9.11 shows the 2D EBIC maps and the corresponding SE images of three solar cells annealed at 100 °C, 150 °C and 200 °C, respectively.

Increasing the annealing temperature affects the topography visible in the SE images. At the low annealing temperature of 100 °C (Figure 9.11a), the aluminum electrode shows no defects except what might be some small scratches in the upper right quadrant. At 150 °C (Figure 9.11c), seven round defects appear with a diameter between 150  $\mu\text{m}$  and 200  $\mu\text{m}$ . At the highest temperature of 200 °C (Figure 9.11e) the number of similar defects increases approximately by a factor of two. These defects can be recognized in the corresponding 2D EBIC maps in Figure 9.11d and Figure 9.11f. At the same positions the EBIC signal is as low as adjacent to the electrode. Figure 9.11f shows even more similar deficient areas than the corresponding SE image.

Apart from the occurring round defects at higher temperatures, the overall EBIC yield has distinct differences for different temperatures. The 100 °C device in Figure 9.11b shows high EBIC currents in the center of the electrode with minor fluctuations of a characteristic length, which is larger than the resolution of the EBIC map (step size: 52  $\mu\text{m}$ ). Between the border and the center of the device exists a 200–300  $\mu\text{m}$  wide band of very poor EBIC generation. The EBIC signal increases again close to the border and forms a 200  $\mu\text{m}$  wide ring of moderate currents. A characterization with a standardized light source was performed before the EBIC measurements and yielded the following results:  $V_{OC} = 0.56 \text{ V}$ ,  $J_{SC} = 5.75 \text{ mA/cm}^2$ ,  $FF = 56.4 \%$  and  $\eta = 1.82 \%$ . The corresponding current-voltage curves are shown in Figure 9.12.

The 150 °C device in Figure 9.11d shows an improvement of EBIC generation compared to 9.11b. The maximum current is higher (130 pA compared to 100 pA) and there is no band of low or none EBIC signal. Similarly, the center area of the device produces higher currents than the outer regions. A thin ring of higher currents is present in the border region. Strikingly, the shape is following the edge of the electrode, especially at the corners and at the connection of the aluminum line on the left. The observation of higher EBIC signal on a larger effective area is consistent with the results of the light characterization method ( $V_{OC} = 0.62 \text{ V}$ ,  $J_{SC} = 5.66 \text{ mA/cm}^2$ ,  $FF = 55.4 \%$  and  $\eta = 1.95 \%$ , see Figure 9.12), although not as clearly as expected. The lower EBIC signal in the upper right corner is an imprint of an earlier EBIC measurement. The signal is decreased due to the irreversible beam damage, which occurred during the earlier scan.

In the device with an annealing temperature of 200 °C (Figure 9.11f), an overall deterioration of EBIC yield is observed. The magnitude of the generated current is strongly reduced. Current values of higher magnitude (yellow and red colors) appear only in two small areas. Besides the large number of round defects, most of the inner

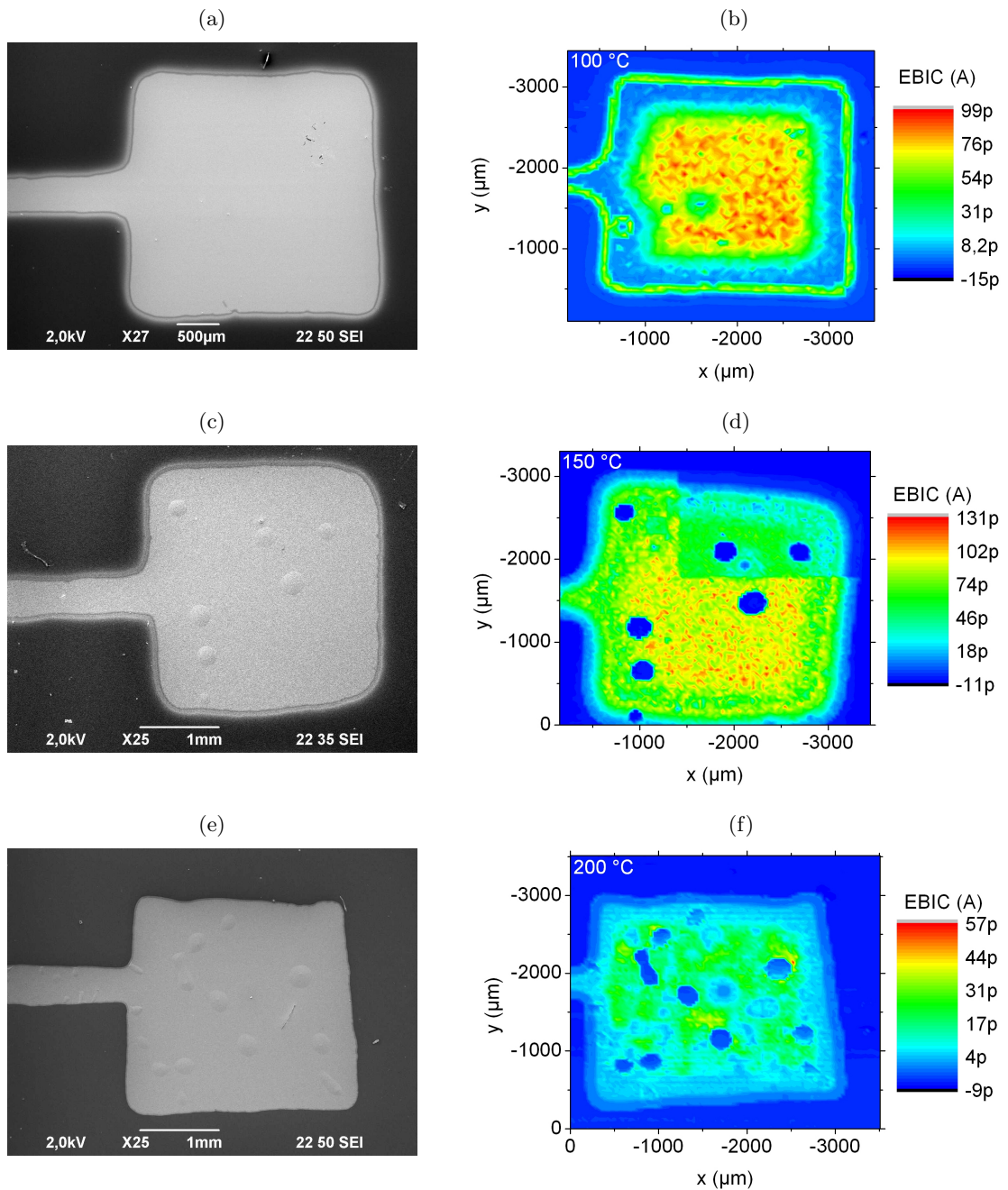


Figure 9.11.: SE images of spin coated P3HT:PCBM solar cells with postproduction annealing temperatures of (a) 100 °C, (c) 150 °C and (e) 200 °C. The corresponding 2D EBIC maps are shown in (b), (d) and (f). The electron beam energy was 5 kV, the scan window size was  $86 \mu\text{m}^2$ . The step size was  $52 \mu\text{m}$  in (b) and  $35 \mu\text{m}$  in (d) and (f). The upper right corner of the device in (d) was scanned before and yields therefore a lower current due to beam damage.

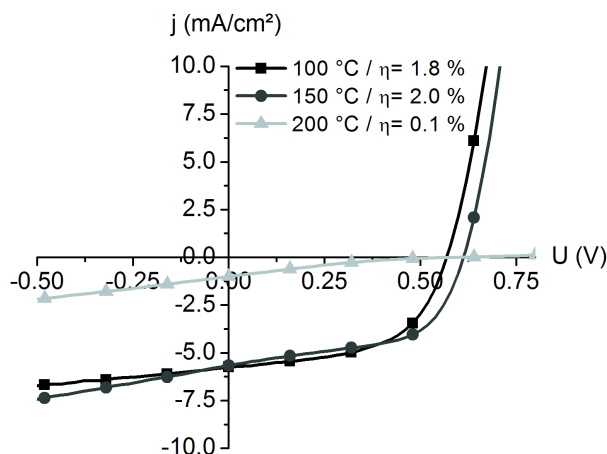


Figure 9.12.: Current-voltage curves of the examined P3HT:PCBM solar cells shown in Figure 9.11.

part of the electrode shows a mediocre EBIC signal (green) which decreases towards the border. The poor performance was also apparent in the light characterization. The determined values were  $V_{OC} = 0.6$  V,  $J_{SC} = 1.01$  mA/cm<sup>2</sup>,  $FF = 17.2$  % and  $\eta = 0.1$  % (see Figure 9.12).

In conclusion, the examination of the impact of different annealing temperatures on the device performance of P3HT:PCBM solar cells by means of EBIC measurements yield interesting insights in addition to the device characterization by the standard method with a light source. Both measurement techniques showed for the device that was annealed at 150 °C the best results. There, the magnitude of the EBIC current reached the highest values on a large part of the active area. Increasing the annealing temperature generated areas of circular shape, where no EBIC was produced. These defects decrease the effective photoactive area. The defects originate probably from gas bubbles formed during the annealing step. In this case, the generation of these defects could be prevented by evaporating the aluminum layer after the annealing step. The origin of the inhomogeneities in the generated EBIC current with fluctuation lengths of several tens of micrometer could not be clarified.

#### 9.4.5. Solar Cells Fabricated by Squeegee-Coating Processing

Instead of spin coating the organic layers on the substrate, a batch of P3HT:PCBM solar cells were fabricated by squeegee-coating of the photoactive material and annealed at a temperature of 100 °C. The beam energy was set to 5 kV, the scan window size was 86  $\mu\text{m}^2$  and the lateral step size was 35  $\mu\text{m}$ . The SE images and the measured 2D EBIC maps of three devices are shown in Figure 9.13.

The 2D maps show over a large area of the device a homogenous EBIC signal with small variations on a length scale comparable to the scan resolution. In Figure 9.13b

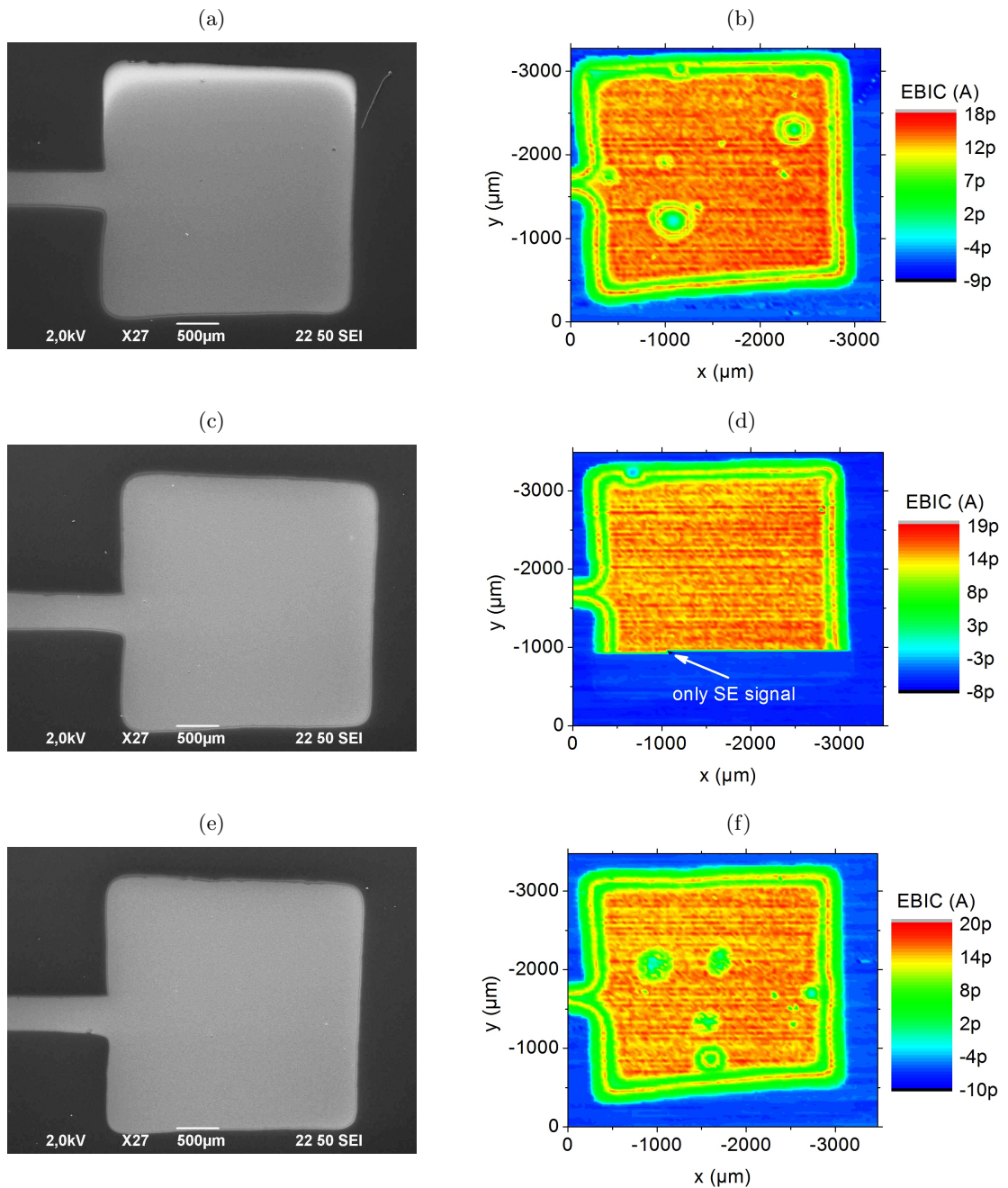


Figure 9.13.: (a), (c) and (e): SE images of P3HT:PCBM solar cells fabricated by squeegee-coating processing and an annealing temperature of 100 °C. The corresponding 2D EBIC maps are shown in (b), (d) and (f). The electron beam energy was 5 kV, the scan window size was 86  $\mu\text{m}^2$  and the step size 35  $\mu\text{m}$ . The lower part of the scan in (d) up to the position indicated by the arrow, only one electrode was contacted and therefore just the specimen current is recorded. The difference in magnitude of the EBIC signal and the specimen current is striking.

and 9.13f round defects of sizes from 50 to 500  $\mu\text{m}$  are present in the center region, in Figure 9.13d only two small ones. In contrast to the defects in Figure 9.9a and 9.11, the EBIC current is only reduced at the defects, but does not vanish. Additionally, along the edges of the devices an approximately 500  $\mu\text{m}$  wide area of reduced current is measured. In the center of these areas as well as in some larger round defects a characteristic ring of increased EBIC current with a width of around 50  $\mu\text{m}$  is visible. During the measurement in the lower part of the scan in Figure 9.13d up to the position indicated by the arrow, only one electrode was contacted and therefore just the specimen current was recorded.

Overall, the squeegee-coating method seems to produce solar cell devices with at least similar quality compared to spin coated devices. The EBIC maps show a high performance over a large area of the device, although the appearance of defects is not inhibited. The reason for the overall low magnitude of the measured EBIC current compared to the measurements in Figure 9.11 is not quiet clear.

## 9.5. EBIC in CdS/CZTS Solar Cells

Solar cells made from inorganic active materials were also examined by the EBIC technique. The photoactive layer consisted of 120–130 nm of CdS/Cu<sub>2</sub>ZnSnS<sub>4</sub> (CdS/CZTS). EBIC measurements were performed to analyze the homogeneity of the current generation and compare the results with the P3HT:PBCM solar cells.

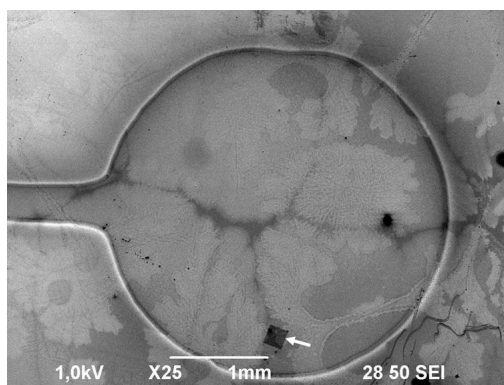


Figure 9.14.: SE image of a CdS/CZTS solar cell. A large fraction of the surface is covered with precipitates from unknown origin. The region of an EBIC scan can be seen as a dark square at the bottom of the image (indicated by the white arrow).

An SE image of such a device is shown in Figure 9.14. A large fraction of the imaged surface shows some precipitation, which looks brighter in the SE image than the clean areas. The sample was not freshly prepared but stored for some weeks in a glove box under nominally inert conditions, so it can not be excluded that the precipitations on the sample surface developed during storage.

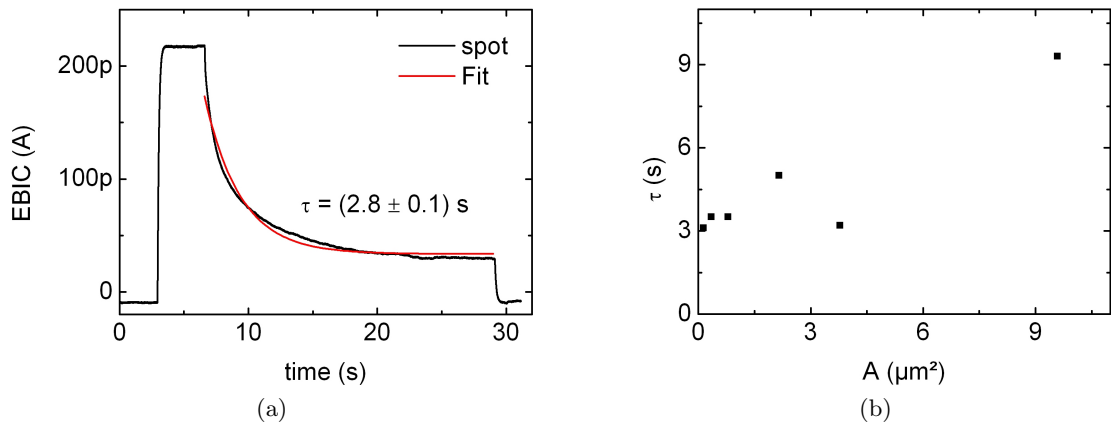


Figure 9.15.: (a) Electron beam induced current decay of a beam exposure of 5 kV in spot mode of a CdS/CZTS solar cell and the fitted exponential decay with decay time constant of  $\tau = (2.8 \pm 0.1) \text{ s}$ . (b) Decay time constants in dependence of different scan area sizes at a beam energy of 10 kV.

For studying the beam damage and calculating the decay time constant  $\tau$  on these solar cell devices, a series of stationary EBIC measurements with varying scan window sizes were performed. In Figure 9.15a a time series of a beam exposure of 5 kV is shown, where the electron beam was set to spot mode. The experimental data was fit to an exponential decay (Eq. 9.2) and yields a decay time constant of  $\tau = (2.8 \pm 0.1) \text{ s}$ . This measurement was also performed for different beam exposure areas at a beam energy of 10 kV and the resulting decay time constants are plotted in Figure 9.15b over the exposed area. The approximately linear increase of the decay time constant with exposed area indicates a linear dependence of the beam damage and electron dose. Compared to P3HT:PCBM cells (see Figure 9.8a) the electron dose is roughly a factor of hundred times bigger for similar decay time constants. Because of the long decay time at high electron doses in the CdS/CZTS cells, it is possible to map the EBIC signal with the electron beam set to spot mode, which yields the highest possible resolution.

An EBIC measurement with the beam set to spot mode and a beam energy of 5 kV is shown in Figure 9.16b. The step size of the substage was 1  $\mu\text{m}$ , which is on the order of magnitude of the interaction volume size. The scanned area can be seen in the SE image in Figure 9.14 as the dark square indicated by the white arrow. Regions of high EBIC signal correspond to regions without precipitations in the SE image.

A second scan with a step size of 4  $\mu\text{m}$  was placed around the smaller scan. In the 2D EBIC map in Figure 9.16b the smaller scan can be seen as an imprint because of the reduced EBIC signal in the preexposed areas due to the beam damage. However, the measured features are in qualitative agreement. Note that in the regions of high EBIC yield, the signal is rather homogeneous, compared to the examined organic solar cells.

A second device was examined with the focus on imaging the whole device rather than having a high resolution map of small dimensions. The solar cell in Figure 9.17a

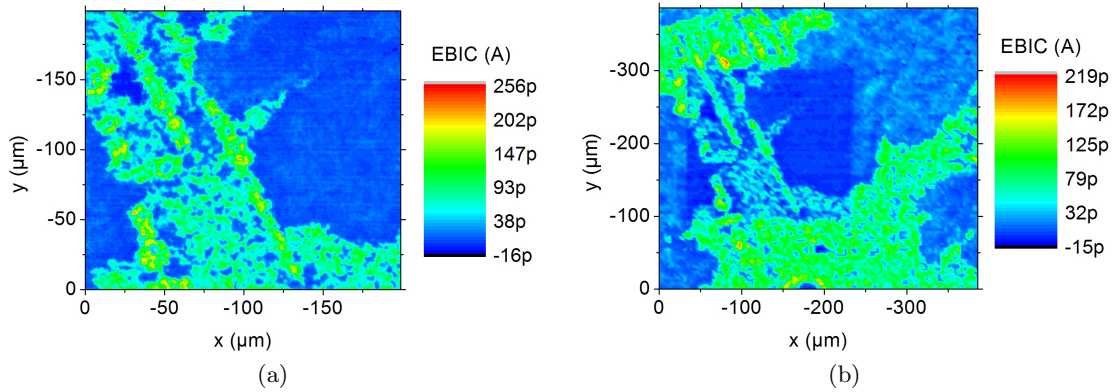


Figure 9.16.: (a) High resolution 2D EBIC map of a CdS/CZTS solar cell with beam energy 5 kV. The beam was set to spot mode and the step size was 1  $\mu\text{m}$ . (b) A second EBIC map was recorded, placed around the scan in (a) with a step size of 4  $\mu\text{m}$ .

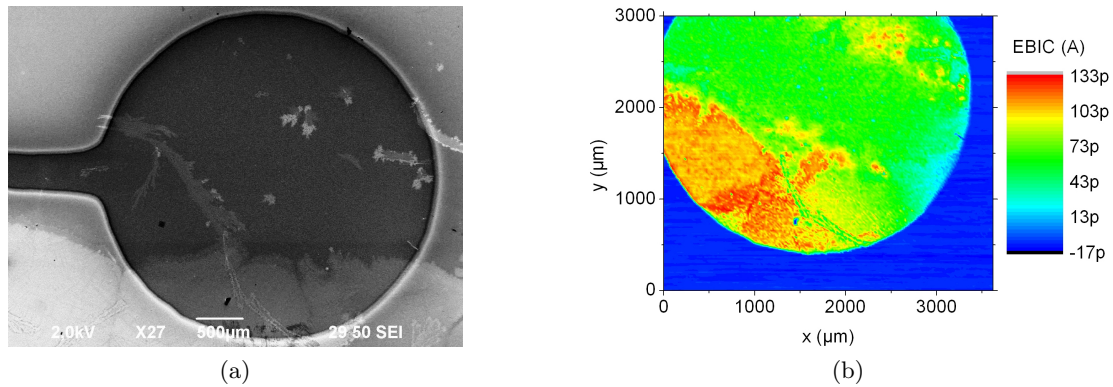


Figure 9.17.: (a) SE image of a second CdS/CZTS solar cell. Again, the surface is partly covered with precipitations. (b) 2D EBIC map of the inorganic solar cell at 10 kV beam energy and a stepsize of 18.2  $\mu\text{m}$ . The whole device produces an EBIC signal, but a clear twofold separation takes place with one area (around 20% of the electrode area) having twice the EBIC magnitude then the rest. The boundary between the two regions coincides with the topography in (a). (The 2D map is rotated by 15  $^\circ$  counterclockwise compared to the SE image.)

was scanned in spot mode at 10 kV beam energy and a lateral resolution of 18.2  $\mu\text{m}$ . The whole device produces an EBIC signal, but a clear twofold separation takes place with one area (around 20 % of the electrode area) having twice the EBIC magnitude than the rest (see Figure 9.17b). The boundary between the two regions coincides with features of the topography in the EBIC image.

## 9.6. Conclusion

It has been demonstrated that it is possible to perform EBIC measurements on solution processed solar cells by illuminating the active region with an electron beam that penetrates the metal back contact. The solar cells that were measured were prototypes which were being used to optimize the fabrication process. Useful information about the homogeneity of the solar cells can be obtained on scales ranging from microns to millimeters and the form of the defects can be obtained from the measurements.

In the results for P3HT:PCBM solar cells, three main problems could be identified concerning the homogeneity of these devices. In all examined devices, the measured EBIC current was reduced in the border region compared to the center of the solar cells. The postproduction annealing process generated additional defects of round shape with a strongly reduced EBIC yield. Increasing the annealing temperature increased also the number of these defects. Presumably, gas bubbles were formed during the annealing and degraded the morphology of the layer stack. Apart from these obvious defect features in the 2D EBIC maps, fluctuations of the measured current were observed on a length scale of typically a few to tens of micrometers.

For the inorganic CdS/CZTS solar cells, 2D EBIC maps were successfully generated. The beam damage was small enough, to set the electron beam to spot mode. In this way, high resolution measurements could be performed with a step size of only 1  $\mu\text{m}$ . The large scan, that covered the whole device, showed strong inhomogeneities, which correlated to structural features in the corresponding SE image. Because of the history of the devices, it can not be excluded, that these inhomogeneities originate from aging processes of the CdS/CZTS devices.

## 10. Summary

Electrical probing and mechanical manipulation of small objects and devices on a micro- and nanometer scale is of great importance. Especially in research, a flexible and quick method for performing such measurements is desired.

For this purpose, a scanning electron microscope (SEM) probe station was assembled during this work. Up to six micromanipulators can be installed inside the modified JEOL SEM (*JSM-6490LV*) for manipulation and electrical measurements. Peripheral measurement instruments and the movement of the manipulators and the substage can be controlled by a PC. Several control and data acquisition programs were written to automate and link the diverse machines for complex measurement routines.

Additionally to the SEM probe station, a light microscope probe station was built, which is situated inside a vacuum chamber. This setup can be used for probing macroscopic devices, for test purposes or situations, where the sample should not be exposed to an electron beam.

The SEM probe station was used for mechanical manipulation of small objects. Gold particles with a diameter of 200 nm were moved over a substrate and were arranged to arbitrary shapes. The attractive van der Waals interaction between tip and a multi-walled carbon nanotube (MWCNT) was employed to pick up the nanotube, pull it out from a bundle and transport it to another position. In this way, conducting high aspect ratio probe tips were produced. Similarly, single crystal metal nanowires were suspended between two tips and current-voltage characteristics of the nanowires were obtained.

Sharp probe tips and the small contact areas, that are present during the probing of micro- and nanostructures, lead to a range of interesting physical phenomena. These include field emission, quantum mechanical tunneling processes, quantum point contacts, Sharvin contacts and classical Holm contacts. For the electrical characterization of small devices, the contribution of large contact resistances to the measured total resistance can be inconvenient. In addition, contacts with a small area are often unstable.

There are several ways to reduce contact resistances. By forcing high currents through the contact, contact resistances were improved due to electromigration and electrical forming. Oxide layers, which prevented a low-ohmic contact, were removed by current heating and focused ion beam (FIB) milling. Scratching a probe tip over the contact surface can also lower the contact resistance, because of the removal of existing oxides or contaminants at the interface. The right choice of the tip material can also prevent contact problems beforehand.

Another way to circumvent the problem of large contact resistance is by using adequate measurement techniques. Three-point scanning measurements were presented, where the contact resistance can be separated from the sample resistance and both

quantities were determined. A five-probe scanning measurement was used to determine the 2D potential distribution of a high-resistive film of carbon nanotubes (CNTs) that were dispersed on a PET foil.

The same sharp metal tips, that we use for electrical probing, can also be used to structure and modify metal surfaces. We developed the contact-breaking microspark erosion (CBME) process to cut metal lines in integrated circuits and structure thin metal films. Electrical fusing was employed to modify a photolithography mask and to interrupt a conducting path in a metal wire. These methods can be of use in failure analysis or mask repair and would be much cheaper than the often used method of using a FIB.

Not only can the SEM be used as an observational tool in the measurements, it can play an active role. Voltage contrast imaging was used to inspect an integrated circuit, where electrically connected parts can be distinguished from the rest of the circuit. The potential drop across a p-n junction in reverse bias was observed and the position of the p-n junction can be seen in the secondary electron image. Voltage contrast imaging was also used to enhance the visibility of single-walled carbon nanotube (SWCNT) and to detect broken tubes and the point of rupture.

By creating electron-hole pairs in semiconductors with the electron beam, the locally generated electron beam induced current (EBIC) was measured in silicon based devices. The charge carrier diffusion lengths in the proximity of p-n junctions and Schottky contacts were determined and the local short-circuit current was measured in solar cells.

The EBIC measurement technique was used for extensive studies on solution processed organic (P3HT:PCBM) and inorganic (CdS/CZTS) solar cells. The generated 2D EBIC maps were used to characterize the homogeneity of the solar cells on scales ranging from microns to millimeters. Large variations in the EBIC signal were observed indicating that the performance of the solar cells was not uniform. This means that measurements, where the solar cells are exposed to a uniform light source and the total current is measured, have to be interpreted with care. The EBIC measurements also show that observed defects correlate to fabrication process parameters.

The immanent flexibility of a SEM probe station was utilized to investigate a broad range of samples with diverse measurement techniques. Several research areas of solid state physics can be addressed and explored with this setup. During the several stages of evolution of our equipment, a significant knowledge on probing on a small scale inside a SEM was established.

# Bibliography

- [1] N. Agraït, A. L. Yeyati, and J. M. van Ruitenbeek. Quantum properties of atomic-sized conductors. *Physics Reports*, 377(2–3):81–279, 2003.
- [2] J. Bardeen and W. G. Pfann. Effects of electrical forming on the rectifying barriers of *n*- and *p*-germanium transistors. *Phys. Rev.*, 77(3):401–402, Feb 1950.
- [3] R. B. Bergmann. Crystalline Si thin-film solar cells: a review. *Applied Physics A*, 69:187–194, 1999.
- [4] H. Bethge and J. Heydenreich, editors. *Elektronenmikroskopie in der Festkörperphysik*. Springer-Verlag Berlin Heidelberg New York, 1982.
- [5] O. Breitenstein, J. Bauer, M. Kittler, T. Arguirov, and W. Seifert. EBIC and luminescence studies of defects in solar cells. *Scanning*, 30(4):331–338, July–August 2008.
- [6] Qing Chen, Sheng Wang, and Lian-Mao Peng. Establishing ohmic contacts for in situ current-voltage characteristic measurements on a carbon nanotube inside the scanning electron microscope. *Nanotechnology*, 17:1087–1098, 2006.
- [7] Volker Cimalla, Claus-Christian Röhlig, Jörg Pezoldt, Merten Niebelschütz, Oliver Ambacher, Klemens Brückner, Matthias Hein, Jochen Weber, Srdjan Milenkovic, Andrew Jonathan Smith, and Achim Walter Hassel. Nanomechanics of single crystalline tungsten nanowires. *Journal of Nanomaterials*, vol. 2008:9 pages, 2008.
- [8] John D Cutnell and Kenneth W Johnson. *Physics*. Wiley, 4th edition edition, 1998.
- [9] Lixin Dong, Kaiyu Shou, D.R. Frutiger, A. Subramanian, Li Zhang, B.J. Nelson, Xinyong Tao, and Xiaobin Zhang. Engineering multiwalled carbon nanotubes inside a transmission electron microscope using nanorobotic manipulation. *Nanotechnology*, *IEEE Transactions on*, 7(4):508–517, July 2008.
- [10] Dominique Drouin, Alexandre Réal Couture, Xavier Tastet, Vincent Aimez, and Raynald Gauvin. CASINO v2.42 - A fast and easy-to-use modeling tool for scanning electron microscopy and microanalysis users. *Scanning*, 29(3):92–101, 2007.
- [11] R. F. Egerton. *Physical Principles of Electron Microscopy*. Springer, 2005.
- [12] I. Ekvall, E. Wahlstrom, D. Claesson, H. Olin, and E. Olsson. Preparation and characterization of electrochemically etched W tips for STM. *Measurement Science & Technology*, 10(1):11–18, January 1999.

- 
- [13] D. Erts, H. Olin, L. Ryen, E. Olsson, and A. Thölen. Maxwell and sharvin conductance in gold point contacts investigated using TEM-STM. *Physical Review B*, 61(19):12725–12727, 2000.
- [14] T. E. Everhart and R. F. M. Thornley. Wide-band detector for micro-microampere low-energy electron currents. *Journal of Scientific Instruments*, 37(7):246–248, 1960.
- [15] J. Fujita, Y. Ohnishi, Y. Ochiai, and S. Matsui. Ultrahigh resolution of calixarene negative resist in electron beam lithography. *Applied Physics Letters*, 68:1297, 1996.
- [16] S. A. Galloway, P. R. Edwards, and K. Durose. Characterisation of thin film CdS/CdTe solar cells using electron and optical beam induced current. *Solar Energy Materials & Solar Cells*, 57:61–74, 1999.
- [17] J. K. Gimzewski and R. Möller. Transition from the tunneling regime to point contact studied using scanning tunneling microscopy. *Phys. Rev. B*, 36(2):1284–1287, July 1987.
- [18] M.A. Grado-Caffaro and M. Grado-Caffaro. Electrical conductance from the fowler-nordheim tunneling. *Optik*, 116:299–300, 2005.
- [19] Werner Grogger. Rasterelektronenmikroskopie (519.003), TU Graz. lecture notes, February 2008.
- [20] C. Groves, O. G. Reid, and D. S. Ginger. Heterogeneity in polymer solar cells: Local morphology and performance in organic photovoltaics studied with scanning probe microscopy. *Accounts of Chemical Research*, 43(5):612–620, 2010.
- [21] Hubert B. Heersche, Günther Lientschnig, Kevin O’Neill, Herre S. J. van der Zant, and Henny W. Zandbergen. In situ imaging of electromigration-induced nanogap formation by transmission electron microscopy. *Applied Physics Letters*, 91(7):072107, 2007.
- [22] Ragnar Holm. *Electric Contacts*. Springer, reprint of the fourth completely rewritten edition 1967, 3rd print edition, 2000.
- [23] H. Hoppe and N. S. Sariciftci. *Photoresponsive Polymers II*, volume 214 of *Advances in Polymer Science*. Springer (Berlin / Heidelberg), 2008.
- [24] Hironori Katagiri, Kotoe Saitoh, Tsukasa Washio, Hiroyuki Shinohara, Tomomi Kurumadani, and Shinsuke Miyajima. Development of thin film solar cell based on cu<sub>2</sub>znsns<sub>4</sub> thin films. *Solar Energy Materials and Solar Cells*, 65(1–4):141–148, 2001.
- [25] Charles Kittel. *Introduction to Solid State Physics*. Wiley, 8 edition, 2005.

- [26] A. Krishnan, E. Dujardin, T. W. Ebbesen, P. N. Yianilos, and M. M. J. Treacy. Young's modulus of single-walled nanotubes. *Phys. Rev. B*, 58(20):14013–14019, November 1998.
- [27] Jeong-O Lee, Hye-Mi So, Eun-Kyoung Jeon, Hyunju Chang, Keehoon Won, and Yong Kim. Aptamers as molecular recognition elements for electrical nanobiosensors. *Analytical and Bioanalytical Chemistry*, 390:1023–1032, February 2008.
- [28] M. Mas-Torrent, S. Masirek, P. Hadley, N. Crivillers, N.S. Oxtoby, P. Reuter, J. Veciana, C. Rovira, and A. Tracz. Organic field-effect transistors (OFETs) of highly oriented films of dithiophene-tetrathiafulvalene prepared by zone casting. *Organic Electronics*, 9(1):143–148, 2008.
- [29] C.N. Mc Auley, A. Rummel, F.W. Keating, and S. Kleindiek. 3D failure analysis in depth profiles of sequentially made fib cuts. *Microelectronics Reliability*, 47:1595–1598, 2007.
- [30] C. R. McNeill, H. Frohne, J. L. Holdsworth, and P. C. Dastoor. Near-field scanning photocurrent measurements of polyfluorene blend devices: Directly correlating morphology with current generation. *Nano Letters*, 4(12):2503–2507, 2004.
- [31] Cattien V Nguyen, Qi Ye, and M Meyyappan. Carbon nanotube tips for scanning probe microscopy: Fabrication and high aspect ratio nanometrology. *Measurement Science and Technology*, 16(11):2138–2146, 2005.
- [32] L. Ottaviano, L. Lozzi, and S. Santucci. Scanning auger microscopy study of W tips for scanning tunneling microscopy. *Review of Scientific Instruments*, 74(7):3368–3378, JUL 2003.
- [33] Ludwig Reimer and Gerhard Pfefferkorn. *Rasterelektronenmikroskopie*. Springer-Verlag Berlin Heidelberg New York, 2 edition, 1977.
- [34] D. Reynaerts, W. Meeusen, and H. Van Brussel. Machining of three-dimensional microstructures in silicon by electro-discharge machining. *Sensors and Actuators A*, 67:159–165, 1998.
- [35] Meltem Sezen, Harald Plank, Philipp M. Nellen, Stephan Meier, Boril Chernev, Werner Grogger, Evelin Fisslthaler, Emil J. W. List, Ullrich Scherf, and Peter Poelt. Ion beam degradation analysis of poly(3-hexylthiophene) (P3HT): can cryo-FIB minimize irradiation damage? *Physical Chemistry Chemical Physics*, 11(25):5130–5133, 2009.
- [36] Paul G. Slade, editor. *Electrical Contacts*. Dekker, 1999.
- [37] Richard Smalley. Of chemistry, love and nanobots. *Scientific American*, pages 68–69, September 2001.

- [38] Paul Stokes and Saiful I. Khondaker. Controlled fabrication of single electron transistors from single-walled carbon nanotubes. *Applied Physics Letters*, 92(26):262107, 2008.
- [39] J.A. Thiele and M. Pereira da Cunha. High temperature LGS SAW devices with Pt/WO<sub>3</sub> and Pd sensing films. In *IEEE Symposium on Ultrasonics*, volume 2, pages 1750–1753, 5-8 2003.
- [40] R.S. Timsit. Electrical conduction through small contact spots. *Components and Packaging Technologies, IEEE Transactions on*, 29(4):727–734, dec. 2006.
- [41] H. S. J. van der Zant, B. J. van Wees, C. J. Muller, H. A. Rijken, and J. E. Mooij. Phase transitions of 2D josephson tunnel junction arrays. *Japanese Journal of Applied Physics*, 26S3(Supplement 26-3-2):1763–1764, 1987.
- [42] X. Wang, D. Zhang, K. Braun, H.-J. Egelhaaf, C. J. Brabec, and A. J. Meixner. High-resolution spectroscopic mapping of the chemical contrast from nanometer domains in P3HT:PCBM organic blend films for solar-cell applications. *Advanced Functional Materials*, 20(3):492–499, 2010.
- [43] R. Y. Zhang, Y. Wei, L. A. Nagahara, I. Amlani, and R. K. Tsui. The contrast mechanism in low voltage scanning electron microscopy of single-walled carbon nanotubes. *Nanotechnology*, 17(1):272, 2006.

# Acknowledgments

The research presented in this Ph.D. thesis would not have been possible without the contribution of a lot of people with whom I have been working or collaborating during the last years of my scientific research. It is my pleasure to take this opportunity to thank all the people who were directly or indirectly involved and supported me in my work.

First of all, I want to thank my supervisor Peter Hadley for giving me the opportunity, to work with him in Delft and in Graz. His positive attitude and his constant support was a most valuable guide during the last years. I hope, the original Dutch “fiets” I inherited from Peter will ride for years to come.

I am greatly indebted to Prof. Dr. Christian Teichert for being the second examiner of my defence.

Thanks to all the people of the MED group. I had a great time in Delft and enjoyed my stay in the Netherlands very much. Special thanks to Jay (Jae-Ryoung) Kim for the good teamwork and the memorable trip to Den Haag with Jeroen, to Jeroen B. Oostinga and Hangxing Xie for the pleasurable atmosphere in our office, to Christian A. Martin for several “lekker biertjes” and the possibility to speak German once in a while. Thanks to Benoit Witkamp, Edgar A. Osorio, Anna S. Molinari, Murat Durkut, the professors Herre S.J. van der Zant and Alberto F. Morpurgo, the always helpful and cheerful secretaries Maria Roodenburg-van Dijk and Monique Vernhout and all the others. I am also grateful for the cooperation on the interesting subject of solid phase epitaxy with Yann Civalé and Lis Nanver and the support and guidance of the scientists at the cleanroom facilities of DIMES.

During the four years in Graz a lot of very good friendships were formed, many of them in the institute. I have to thank Peter Pacher for our melodic adventures in the Nachtexpress, Gerold Rangger for showing me the mountains, Oliver Hofmann for the Guitar Hero sessions, Anna Track for the delicious Spritz in Venezia, Ferdinand Rissner and David Egger for the movie evenings and the introduction to Linux, Thomas Haber for leading me to the soccer training and the tandem jump, Horst Scheiber for long evenings on the Physiker-Stammtisch and honoring me by assigning me as his successor and Lorenz Romaner for adopting the tradition of and carrying out the Feuerzangenbowle event.

I would like to thank my coworkers from the institute for scientific and non-scientific discussions, movie evenings, extensive coffee and lunch breaks, funny institute excursions, a great atmosphere and much more. Credits go to Mathis Gruber, Veronika Proschek, Harald Etschmaier, Lukas Wittwer, Marco Marchl, Simon Ausserlechner, Thomas Obermüller, Andrej Golubkov, Stefan Kirnstötter, Lukas Ladinig, Sabrina Eder, Evelin Fisslthaler, Stefan Sax, Alex Blümel, Arno Meingast, Michael Pienn, Harald

Plank, Wolfgang Wiedemair, the professors Egbert Zojer, Roland Resel, Robert Schennach, Emil List, Manfred Leisch, Günter Leising, Adolf Winkler, Hartmut Kahlert and all the people I forgot to mention.

Special thanks go to Elisabeth Stern, Esther Schennach and Claudia Fritz for administrative support as well as to Harald Kerschbaumer and Birgit Kunert for technical support. Martin Kornschöber, Robert Krauß and Wolfgang Wurzwallner made strong contributions for the probe station setup by building many unique parts in the workshop. Invaluable technical support was also provided by staff members of Kleindiek and Labco.

I greatly thank Thomas Rath and coworkers at ICTOS and the Christian Doppler Laboratory for Nanocomposite Solar Cells for the excellent cooperation on the EBIC measurements of solution processed solar cells. Special thanks go to Thomas Rath for the fabrication of the organic solar cells and the fruitful discussions, to Achim Fischereder for providing the inorganic solar cells, Wernfried Haas for the high resolution SEM image of the inorganic solar cell cross section and Gregor Trimmel for discussions.

Further I want to thank Alex Blümel for performing AFM measurements and providing the image of the CBME cut aluminum lines.

I am also greatly indebted to Peter Pölt, Ferdinand Hofer, Angelika Reichmann and coworkers from FELMI for the collaboration and the possibility to install our probe station equipment in their SEMs. Special thanks go to Harald Plank for excellent cooperation (KPFM characterization of SWCNTs, sharpening tungsten tips in the FIB, Infineon test sample) and Johannes Rattenberger for producing the cross section image of the organic solar cell.

At this point, I want to thank my family for the constant support and believing in me. Especially I want to thank my brother Danny to whom I can always rely on and discuss scientific or any other problems. Pit and Birgit Loës provided invaluable assistance by helping me move across Europe (already several times now and soon again) and storing parts of my household in Kattbek. The Kayak trip through Holland with Pit, Danny and Tina was an awesome journey.

Finally, I want to thank Conni for her love, her support and her patience during the last years.

# Appendix



# A. Selected Program Codes

In this Appendix, *ADbasic* program codes are presented exemplarily, which were written and developed during this work. The selected codes are elementary for the standard measurement and communication tasks.

## A.1. Basic ADC Program

The “ADC 1.0” code is the elementary program for converting the analog voltage input channels of the *ADwin* into digital form. Because of the time consuming converting process, redundancy should be avoided. On that account, all other programs should refer to this subroutine for measuring input voltages. The sampling rate is one conversion per 10 microseconds. If the *ADwin* system is intensely used in terms of processor time, the process priority could be decreased to prevent a system crash.

```
'<ADbasic Header, Headerversion 001.001>
' Process_Number           = 9
' Initial_Processdelay    = 3000
' Eventsource             = Timer
' Control_long_Delays_for_Stop = No
' Priority                 = High
' Version                 = 1
' ADbasic_Version         = 5.0.5
' Optimize                = Yes
' Optimize_Level          = 1
' Info_Last_Save          = FFPH207 ffph207\PietR
'<Header End>
REM ***** ADC 1.0 *****
REM *****

REM "ADC 1.0" reads out all inputs at maximum speed
REM all other programs should refer to this program for adc tasks

REM OUTPUT:

' FPAR_1 ... FPAR_8: analog input voltages [V]
' FPAR_9 : timestamp [s]

' DATA_20[8]: analog input voltages [24 Bit]
```

```

' DATA_21[1-8]: input voltages [V]
' DATA_21[9]: timestamp [s]

REM *****
REM *****

#INCLUDE ADWINPRO_ALL.INC

DIM DATA_20[8] AS LONG
DIM DATA_21[9] AS FLOAT
DIM i AS LONG

INIT:
  REM AD Wandlung starten
  P2_START_CONVF(1,11111111b)

  globaldelay = 3000          ' 3000 : 10 microseconds

  FPAR_9 = 0.0

  FOR i=1 TO 8
    DATA_20[i]=8388608      ' = Null (24 Bit)
  NEXT i

  FOR i=1 TO 9
    DATA_21[i]=0          ' init data array
  NEXT i

EVENT:

  FPAR_9 = FPAR_9 + 0.00001  ' timestamp [s]

  IF (FPAR_9 = 65535) THEN FPAR_9 = 0  ' FPAR_9 doesn't increase
    ' after 65535 at increment 0.00001 for whatever reason

  REM Wandlung abwarten
  P2_WAIT_EOCF(1,11111111b)

  REM Wandlungsergebnisse auslesen
  P2_READ_ADCF8_24B(1,DATA_20,1)

```

```

REM voltage[V] = voltage[16Bit] * 20 / 65536 - 10
FPAR_1 = DATA_20[1] * 20 / 16777216 - 10
FPAR_2 = DATA_20[2] * 20 / 16777216 - 10
FPAR_3 = DATA_20[3] * 20 / 16777216 - 10
FPAR_4 = DATA_20[4] * 20 / 16777216 - 10
FPAR_5 = DATA_20[5] * 20 / 16777216 - 10
FPAR_6 = DATA_20[6] * 20 / 16777216 - 10
FPAR_7 = DATA_20[7] * 20 / 16777216 - 10
FPAR_8 = DATA_20[8] * 20 / 16777216 - 10

```

```
P2_START_CONVF(1,11111111b)
```

```

DATA_21[1]=FPAR_1
DATA_21[2]=FPAR_2
DATA_21[3]=FPAR_3
DATA_21[4]=FPAR_4
DATA_21[5]=FPAR_5
DATA_21[6]=FPAR_6
DATA_21[7]=FPAR_7
DATA_21[8]=FPAR_8
DATA_21[9]=FPAR_9

```

## A.2. Averaging ADC Measurement

The program “ADC mean 1.1” is reading all input channels and averages over a given number of values. It calculates the mean value and the standard deviation. If multipliers like the sensitivity of a current preamplifier are passed to the program, they will be multiplied to the results.

```

'<ADbasic Header, Headerversion 001.001>
' Process_Number           = 8
' Initial_Processdelay    = 3000
' Eventsource             = Timer
' Control_long_Delays_for_Stop = No
' Priority                 = High
' Version                 = 1
' ADbasic_Version         = 5.0.5
' Optimize                = Yes
' Optimize_Level          = 1
' Info_Last_Save          = FFPH207 ffph207\PietR
'<Header End>
REM ***** ADC mean 1.1 *****
REM *****
REM          calculates average values of all inputs

```

```
REM          !! needs ADC 1_0 for Input values  !!

REM v1.1: deleted globaldelay multiplier (no need,
REM because program can REM make infinite number of cycles)

REM INPUT:

' PAR_13 : # of measurements

' DATA_45: Input Multiplier (i.e. SENS (A/V))

REM OUTPUT:

' DATA_46: mean values (incl. multiplier)
' DATA_47: standard deviation (incl. multiplier)

REM *****

#include adwinpro_all.inc

DIM i, counter AS INTEGER

DIM sumx1, sumxx1, sumx2, sumxx2 AS FLOAT
DIM sumx3, sumxx3, sumx4, sumxx4 AS FLOAT
DIM sumx5, sumxx5, sumx6, sumxx6 AS FLOAT
DIM sumx7, sumxx7, sumx8, sumxx8 AS FLOAT
DIM mean1, mean2, sdev1, sdev2 AS FLOAT
DIM mean3, mean4, sdev3, sdev4 AS FLOAT
DIM mean5, mean6, sdev5, sdev6 AS FLOAT
DIM mean7, mean8, sdev7, sdev8 AS FLOAT

DIM DATA_45[8] AS FLOAT
DIM DATA_46[8] AS FLOAT
DIM DATA_47[8] AS FLOAT

#define numofmeas PAR_13
#define delay PAR_15

#define SENS1 DATA_45[1]
#define SENS2 DATA_45[2]
#define SENS3 DATA_45[3]
#define SENS4 DATA_45[4]
```

## A.2. Averaging ADC Measurement

---

```
#DEFINE SENS5 DATA_45[5]
#DEFINE SENS6 DATA_45[6]
#DEFINE SENS7 DATA_45[7]
#DEFINE SENS8 DATA_45[8]

INIT:

    globaldelay = 3000          'process delay = 10 microsec (100 kHz)

    IF (numofmeas = 0) THEN numofmeas = 100

    FOR i = 1 TO 8
        IF (DATA_45[i] = 0) THEN DATA_45[i] = 1
        ' IF (SENS1 = 0) THEN SENS1 = 1
        DATA_46[i] = 0          ' mean values
        DATA_47[i] = 0          ' sdev values
    NEXT i

    sumx1 = 0
    sumx2 = 0
    sumx3 = 0
    sumx4 = 0
    sumx5 = 0
    sumx6 = 0
    sumx7 = 0
    sumx8 = 0

    sumxx1 = 0
    sumxx2 = 0
    sumxx3 = 0
    sumxx4 = 0
    sumxx5 = 0
    sumxx6 = 0
    sumxx7 = 0
    sumxx8 = 0

    mean1 = 0
    mean2 = 0
    mean3 = 0
    mean4 = 0
    mean5 = 0
    mean6 = 0
    mean7 = 0
    mean8 = 0
```

```
sdev1 = 0
sdev2 = 0
sdev3 = 0
sdev4 = 0
sdev5 = 0
sdev6 = 0
sdev7 = 0
sdev8 = 0

counter = 0

REM *****

EVENT:

INC(counter)

REM ***** read voltage from "ADC" *****

sumx1 = sumx1 + FPAR_1           'sumx1 = summe der messwerte Input 1
sumxx1 = sumxx1 + (FPAR_1)^2    'sumxx1 = summe der quadrate der
                                'messwerte Input 1

sumx2 = sumx2 + FPAR_2
sumxx2 = sumxx2 + (FPAR_2)^2
sumx3 = sumx3 + FPAR_3
sumxx3 = sumxx3 + (FPAR_3)^2
sumx4 = sumx4 + FPAR_4
sumxx4 = sumxx4 + (FPAR_4)^2
sumx5 = sumx5 + FPAR_5
sumxx5 = sumxx5 + (FPAR_5)^2
sumx6 = sumx6 + FPAR_6
sumxx6 = sumxx6 + (FPAR_6)^2
sumx7 = sumx7 + FPAR_7
sumxx7 = sumxx7 + (FPAR_7)^2
sumx8 = sumx8 + FPAR_8
sumxx8 = sumxx8 + (FPAR_8)^2

REM ***** stop after (PAR_13) measurements *****

IF (counter = numofmeas) THEN END
```

FINISH:

```
REM ***** calculate mean and standard deviation *****
REM      ***** store values in data arrays *****

DATA_46[1] = sumx1 / (numofmeas)           ' mittelwert input channel 1
DATA_47[1] = SQRT(((sumxx1 * (numofmeas)) - (sumx1)^2) /
((numofmeas) * (numofmeas - 1)))
'standardabweichung input channel 1

DATA_46[2] = sumx2 / (numofmeas-1)
DATA_47[2] = SQRT(((sumxx2 * (numofmeas)) - (sumx2)^2) /
((numofmeas) * (numofmeas - 1)))
DATA_46[3] = sumx3 / (numofmeas-1)
DATA_47[3] = SQRT(((sumxx3 * (numofmeas)) - (sumx3)^2) /
((numofmeas) * (numofmeas - 1)))
DATA_46[4] = sumx4 / (numofmeas-1)
DATA_47[4] = SQRT(((sumxx4 * (numofmeas)) - (sumx4)^2) /
((numofmeas) * (numofmeas - 1)))
DATA_46[5] = sumx5 / (numofmeas-1)
DATA_47[5] = SQRT(((sumxx5 * (numofmeas)) - (sumx5)^2) /
((numofmeas) * (numofmeas - 1)))
DATA_46[6] = sumx6 / (numofmeas-1)
DATA_47[6] = SQRT(((sumxx6 * (numofmeas)) - (sumx6)^2) /
((numofmeas) * (numofmeas - 1)))
DATA_46[7] = sumx7 / (numofmeas-1)
DATA_47[7] = SQRT(((sumxx7 * (numofmeas)) - (sumx7)^2) /
((numofmeas) * (numofmeas - 1)))
DATA_46[8] = sumx8 / (numofmeas-1)
DATA_47[8] = SQRT(((sumxx8 * (numofmeas)) - (sumx8)^2) /
((numofmeas) * (numofmeas - 1)))

FOR i = 1 TO 8
  DATA_46[i] = DATA_46[i]*DATA_45[i]
  DATA_47[i] = DATA_47[i]*DATA_45[i]
NEXT i
```

### A.3. Basic DAC Program

The “DAC2” code is the elementary program for applying a voltage on an analog output channel of the *ADwin*.

'<ADbasic Header, Headerversion 001.001>

```

' Process_Number           = 10
' Initial_Processdelay    = 30000
' Eventsource             = Timer
' Control_long_Delays_for_Stop = No
' Priority                 = Low
' Priority_Low_Level      = 5
' Version                 = 1
' ADbasic_Version        = 5.0.5
' Optimize                = Yes
' Optimize_Level         = 1
' Info_Last_Save         = FFPH063 FFPH063\Reuter
'<Header End>
#include adwinpro_all.inc

```

EVENT:

```

' PAR_8 = 0: takes voltage FPAR_10 in V

IF (PAR_8 = 0) THEN
  PAR_10 = (FPAR_10 + 10) * 65536 / 20
  P2_DAC(2,PAR_9,PAR_10)
ENDIF

' PAR_8 = 1: takes 16Bit value PAR_10

IF (PAR_8 = 1) THEN
  P2_DAC(2,PAR_9,PAR_10)
  FPAR_10 = PAR_10*20/65536 - 10
ENDIF

END

```

#### A.4. Basic Motion Generator for Nanocontroller and LT6820

The “coarse step with NC” routine controls the motion of a micromanipulator or the x-y substage via the “Analog-In” input. In order to stay in the allowed voltage range of  $\pm 10$  V the “FineStep” value of the *Nanocontroller* is incorporated.

```

'<ADbasic Header, Headerversion 001.001>
' Process_Number           = 4
' Initial_Processdelay    = 30000
' Eventsource             = Timer
' Control_long_Delays_for_Stop = No

```

```

' Priority                      = Low
' Priority_Low_Level            = 5
' Version                      = 1
' ADbasic_Version              = 5.0.5
' Optimize                     = No
' Info_Last_Save               = FFPH063 FFPH063\Reuter
'<Header End>
REM *****
REM *** motion generator with coarse steps (+NC) ***
REM *****

REM  PAR_31      : output channel
REM  PAR_33      : If = 1 then positive motion is generated
REM              If = -1 then negative negative motion is generated

REM  FPAR_31     : NC FINE
REM  FPAR_32     : decreases amplitude

#include adwinpro_all.inc          ' Include-file for Pro-system

DIM maxpos, minpos, NCscale AS LONG
DIM finepos AS LONG              ' [-32768, 32767]

#define direction PAR_33

INIT:

    globaldelay=3000              'cycle-time of 10 microsec

    IF (FPAR_31 >= 0) THEN        ' correct height with Fine NC values
        maxpos = 32767 - 16*FPAR_31 - FPAR_32 ' clkw
        minpos = -32768 + FPAR_32
    ELSE
        maxpos = 32767 - FPAR_32
        minpos = -32768 - 16*FPAR_31 + FPAR_32
    ENDIF

    NCscale = 16*FPAR_31 + 32768
    finepos = 32768 - NCscale

EVENT:

```

```

IF (direction = -1) THEN
  IF (finepos <= minpos) THEN
    P2_DAC(2,PAR_31, NCscale)
  END
  ELSE
    dec(finepos)
    P2_DAC(2,PAR_31,finepos + NCscale)
  ENDIF
ELSE
  IF (finepos >= maxpos) THEN
    P2_DAC(2,PAR_31, NCscale)
  END
  ELSE
    inc(finepos)
    P2_DAC(2,PAR_31,finepos + NCscale)
  ENDIF
ENDIF
ENDIF

```

## A.5. Communication with Nanocontroller and LT6820 via RS232

The *ADwin* system can communicate with a *Nanocontroller* and the x-y substage via a RS232 interface. The program “RS232 1-4 Send And Receive NC” presents the platform for the data exchange. A *LabVIEW* program offers the possibility for choosing existing commands from a drop down menu or writing the command in a command line.

```

' Priority = Low
' Priority_Low_Level = 1
' Version = 1
' ADbasic_Version = 5.0.5
' Optimize = Yes
' Optimize_Level = 1
' Info_Last_Save = FFPH063 FFPH063\Reuter
'<Header End>
REM *****
REM *****
REM ***** RS232(1-4) Send and Receive NC + LT *****

REM system variables:

' PAR_70 ... PAR_73

```

```
REM INPUT:

' PAR_74: RS232 channel number (1-4)

' DATA_23[50]: transmission data

REM OUTPUT:

' DATA_24[50]: received data

REM *****
REM *****

#INCLUDE ADwinPRO_ALL.inc

DIM DATA_23[50] AS LONG           'transmission data
DIM DATA_24[50] AS LONG           'received data
DIM i, length AS LONG

INIT:

  globaldelay=300000

  FOR i = 1 TO 50
    DATA_24[i] = -1
  NEXT i

  IF (PAR_74 = 1) THEN RS_INIT(1,1,19200,0,8,0,2)
  IF (PAR_74 = 2) THEN RS_INIT(1,2,19200,0,8,0,2)
  IF (PAR_74 = 3) THEN RS_INIT(3,1,19200,0,8,0,2)
  IF (PAR_74 = 4) THEN RS_INIT(3,2,19200,0,8,0,2)

  PAR_70 = 2
  PAR_73 = 1

EVENT:
```

```
length = DATA_23[1]

SELECTCASE PAR_74

  CASE 1
    PAR_72 = READ_FIFO(1,1)
  CASE 2
    PAR_72 = READ_FIFO(1,2)
  CASE 3
    PAR_72 = READ_FIFO(3,1)
  CASE 4
    PAR_72 = READ_FIFO(3,2)
ENDSELECT

IF (PAR_72 <> -1) THEN
  DATA_24[PAR_73] = PAR_72
  INC PAR_73
ENDIF

IF (PAR_70 <= length+1) THEN

  SELECTCASE PAR_74

    CASE 1
      PAR_71 = WRITE_FIFO(1,1,DATA_23[PAR_70])
    CASE 2
      PAR_71 = WRITE_FIFO(1,2,DATA_23[PAR_70])
    CASE 3
      PAR_71 = WRITE_FIFO(3,1,DATA_23[PAR_70])
    CASE 4
      PAR_71 = WRITE_FIFO(3,2,DATA_23[PAR_70])
  ENDSELECT

  IF (PAR_71 = 0) THEN    INC PAR_70
ENDIF

IF ((PAR_73 > 1) AND (PAR_72 = -1)) THEN
  IF (PAR_70 > length+1) THEN END
ENDIF
```

## A.6. Communication with Current Preamplifier SR570

The communication with the current preamplifier *SR570* via RS232 is vital, if a bias voltage of a certain value is desired. The instrument's control panel offers no control over that property. A dedicated *LabVIEW* program offers the possibility for choosing existing commands from a drop down menu or writing the command in a command line.

```
'<ADbasic Header, Headerversion 001.001>
' Process_Number           = 1
' Initial_Processdelay     = 10000
' Eventsource              = Timer
' Control_long_Delays_for_Stop = No
' Priority                  = Low
' Priority_Low_Level       = 1
' Version                  = 1
' ADbasic_Version         = 5.0.5
' Optimize                 = Yes
' Optimize_Level          = 1
' Info_Last_Save          = FFPH063  FFPH063\Reuter
'<Header End>
#INCLUDE ADwinPRO_ALL.inc

DIM DATA_23[100] AS LONG           'Sendedaten
DIM i, length AS INTEGER

INIT:

    globaldelay=300000

    RS_INIT(1,1,9600,0,8,1,0)
    PAR_70 = 2

EVENT:
    length = DATA_23[1]
    PAR_14 = length

    IF (PAR_70 <= length+1) THEN
        PAR_71 = WRITE_FIFO(1,1,DATA_23[PAR_70])
        IF (PAR_71 = 0) THEN      INC PAR_70
    ENDIF

    IF (PAR_70 > length+1) THEN  END
```



## B. Source and Specifications of the Used Materials for Fabricating Solution Processed Solar Cells

### B.1. Indium Tin Oxide (ITO)

product: CG-61IN (ITO on polished float glass)  
supplier: Delta Technologies  
sheet resistance:  $R_S=15-25 \Omega$   
nominal transmittance:  $>78 \%$   
nominal coating thickness: 80–120 nm  
substrate thickness: 1.1 mm  
typical composition of float glass: 72.6 %  $\text{SiO}_2$ , 0.8 %  $\text{B}_2\text{O}_3$ , 1.7 %  $\text{Al}_2\text{O}_3$ , 4.6 %  $\text{CaO}$ , 3.6 %  $\text{MgO}$  and 15.2 %  $\text{Na}_2\text{O}$   
passivation of float glass: 20–30 nm  $\text{SiO}_2$  nominal index of refraction:  $n = 1.775$   
typical surface roughness:  $< 0.15 \mu\text{m}/20 \text{ mm}$  (peak-to-peak)  
source: <http://www.delta-technologies.com>

### B.2. PEDOT:PSS

product: CLEVIOS<sup>TM</sup> P VP AI 4083  
supplier: H.C. Starck  
chemical name: Poly(3,4-ethylenedioxythiophene) poly(styrenesulfonate) aqueous dispersion  
resistivity: 500–5000  $\Omega\text{cm}$   
solid content: 1.3 to 1.7 %  
Na content: max. 400 ppm  
sulfate content: max. 40 ppm  
PEDOT:PSS ratio: 1:6 (by weight)  
PEDOT work function: approximately 5.2 eV  
boiling point: approximately 100 °C  
source: <http://www.clevios.com>

### **B.3. P3HT**

product: Sepiolid, Poly(3-hexylthiophene-2,5-diyl ), P3HT (item # P200)  
supplier: Rieke Metals, Inc.  
molecular formula: C<sub>10</sub>H<sub>14</sub>S  
regioregularity: < 98 %  
field effect mobility: up to 0.3 cm<sup>2</sup>/Vs  
average molecular weight: < 50000 g/mol  
very low residual metal content  
source: <http://riekemetals.thomasnet.com>

### **B.4. PCBM**

product: [60] PCBM  
supplier: Solenne  
molecular formula: C<sub>72</sub>H<sub>14</sub>O<sub>2</sub>  
chemical name: [6,6]-Phenyl C<sub>61</sub> butyric acid methyl ester  
CAS number: 160848-22-6  
molecular weight: 910.9 g/mol  
fullerene purity: ≥ 99.5 % by HPLC with respect to fullerene content  
source: <http://www.solennebv.com/>

### **B.5. Chloroform**

product: Chloroform CHROMASOLV® Plus, for HPLC  
supplier: Sigma Aldrich  
molecular formula: CHCl<sub>3</sub>  
chemical name: trichloromethane  
CAS number: 67-66-3  
molecular weight: 119.38 g/mol  
boiling point: 60.5–61.5 °C  
purity: ≥ 99.9 %  
contains 0.5–1.0 % ethanol as stabilizer  
source: <http://www.sigmaaldrich.com>